Hybrid Fibre-Wireless Technology for Next Generation Small Cell Deployment

by

Yu Tian

Submitted in partial fulfillment of

the requirements of the degree of

Doctor of Philosophy

Department of Electrical and Electronic Engineering

University of Melbourne

VIC 3010, Melbourne, Australia

April 2018

Abstract

Driven by the ever-increasing data traffic and the need to provide connectivity to nearly everything, a new revolution for wireless access technologies is essential in next generation mobile communications. Analog fronthaul networks employing radio-over-fibre technique offers real potential to overcome the bandwidth and data rate constraints of common public radio interface (CPRI) based digital fronthaul networks. Combined with the license-free millimetre-wave frequency bands, especially 60 GHz frequency band that has 7 GHz bandwidth, analog RoF fronthaul links have the capability to provide broadband access and overcome the spectral congestion in microwave region. Network densification is believed to be a promising candidate to meet the requirements in next generation communication networks, which can be facilitated by utilising small cell deployment for better frequency reuse. In order to improve system spectral efficiency and mitigate inter-cell interference, advanced techniques such as coordinated multipoint (CoMP) and non-orthogonal multiple access (NOMA) have also been actively investigated.

In this thesis, systematic investigations of 60 GHz RoF fronthaul systems are demonstrated experimentally and theoretically. Two fronthaul systems based on modified DSB-SC and modified OSSB modulation technique are proposed and demonstrated. 4-QAM and 16-QAM signals are transmitted over fronthaul links for the two fronthaul solutions, and data rate up to 8 Gbps is obtained. Link performance of the two fronthaul solutions are compared in terms of EVM performance and RF power fading effect caused by fibre chromatic dispersion. Experimental results verify that the modified OSSB fronthaul option is superior for better receiver sensitivity and ability to overcome chromatic dispersion. As a pathway for achieving cost-effective fronthaul, a system integrating two integrated microwave photonic filters is also demonstrated.

Analytical models of the proposed fronthaul systems are presented and discussed, providing a framework for systematic investigation and optimisation of fronthaul systems. Mathematical expressions of received RF signal power as a function of optical carrier-to-sideband ratio (OCSR) are derived. Simulation results illustrated that OSSB fronthaul offers better receiver sensitivity due to its intrinsic smaller OCSR. The derived analytical models are confirmed to

be matched with experimental results closely. The impact of chromatic dispersion is also analysed and discussed.

Advanced techniques including CoMP and NOMA are employed in 60-GHz RoF fronthaul systems. Fronthaul system based on CoMP has the benefits of simplified carrier frequency offsets, reduced signalling overhead. Experimental demonstration verifies that much smaller delay is possible and 4 Gbps, 4-QAM signal is transmitted along 10-km fronthaul links with 1.3-dB receiver sensitivity improvement compared with fronthaul links without CoMP transmission. Furthermore, a multilevel code (MLC) based NOMA RoF fronthaul system is experimentally demonstrated where no successive interference cancellation is required at the receiver. Compared with conventional superposition code (SPC) based NOMA fronthaul, the proposed scheme simplifies receiver complexity and can avoid error propagation. Finally, a multi-user NOMA scheme is experimentally demonstrated with coordinated base stations (BSs) in the 60-GHz RoF fronthaul system for the first time. The proposed architecture could obtain mitigated inter-cell interference and improved system spectral efficiency.

A tractable model for NOMA based fronthaul system with coordinated BSs is developed and confirms the feasibility of the proposed scheme. NOMA technique in fronthaul small cells is further investigated in the context of stochastic demography distribution, including the impact of different user distribution schemes and different NOMA pair clustering schemes. Closed-form expressions of effective SINR and cell throughput are derived considering random number of users and various NOMA clustering schemes. In particular, optimum power allocation ratio to maximize cell throughput is derived in two situations: dynamic power allocation ratio and fixed power allocation ratio among different NOMA pair. Simulation results show that NOMA fronthaul system could achieve about 35% average spectral efficiency gain than traditional orthogonal multiple access (OMA) fronthaul system.

Acknowledgements

I would like to thank all whose cooperation, understanding and guidance helped me overcome the hurdles during my Ph.D. candidature. This thesis could not have been finished without the helps and supports from so many incredible individuals.

First and foremost, I would like to express my utmost gratitude to my supervisors for their generous support, patient guidance, and high-quality supervision. I am grateful to my principal supervisor Prof. Christina Lim for being so supportive and inspiring throughout my candidature. Her enthusiasm for research, immense knowledge, and insightful comments helped me keep motivated and develop deep understanding on my research topic. I must express the deepest gratitude to my co-supervisor Prof. Ampalavanapillai Nirmalathas. His profound thinking and technical insights have inspired me and helped me whenever I was in a dilemma and needed research directions. I would also like to acknowledge my co-supervisor Dr. Alan Lee for the helpful discussions and suggestions on experiments. His encouragements and patient guidance especially at the beginning of my Ph.D. candidature helped me overcome the tough times. In addition, I would like to express my sincere gratitude to my Ph.D. advisory committee member, Prof. William Shieh, for his assistant and precious advice. I am very grateful to the University of Melbourne and Department of Electrical & Electronic Engineering for providing me a world class research environment and offering me the scholarship. Without the financial support, I would not be able to pursue my PhD.

My special thank goes to my colleagues and friends who have offered valuable discussions and encouragements during my PhD candidature: Tian Liang, Di Che, Jian Fang, Feng Yuan, Benoit Gouhier, Cheng Cheng, Fuqiang Gu, Ke Wang, and Qiaowen Lin. I especially appreciate Tian Liang for her assistance, discussions, and supportive friendship when I experience difficulties. I must thank Cheng Cheng for her friendship and support. She is always there to enlighten me and cheer me up when I came across life difficulties.

My heartiest gratitude is for my parents, Yan Li and Yongyou Tian for their endless love, support and inspirations. Thanks to my sister Tian Tian for her continuous encouragements. Finally, I would like to thank my boyfriend, Zhengmao Yao, for his love, endless support, patience and continuous care throughout this journey.

Declaration

This thesis comprises my own work and, except where acknowledged, includes no material previously published by any other person. I declare that none of the work presented in this thesis has been submitted for any other degree or diploma at any university and that this thesis is less than 100,000 words in length, including figures, tables, bibliographies, appendices and footnotes.

Signature_____

Date_____

Preface

This thesis comprises only my original work (100%), which I conducted under the supervision of Prof. Christina Lim, Prof. Ampalavanapillai Nirmalathas, and Dr. Alan Lee. All the work in this thesis was conducted by the author of this thesis including experiments, theoretical analysis, analytical models, MATLAB simulations and manuscript writing, which contributed to above 90% of the work. My supervisors provided insightful technical comments and helpful discussions which contributed to about 10% of the work.

The thesis has not been submitted for other qualifications. All the work towards the thesis was carried out after the enrolment in the degree. No third party editorial assistance was provided in preparation of the thesis. The work was support by the Australian Research Council (ARC) Discovery Project Grant (DP150101977).

Publication [1] (listed in Chapter 1 Section 1.5) contains only the original work of the student, including experiments, analytical models, simulations and manuscripts writing, which contributed to about 90% of the publication. Shijie Song, Keith Powell, and Prof. Xiaoke Yi from the University of Sydney provided the integrated filters that were used in the experiments, which contributed to about 5% of the publication. Prof. Christina Lim, Prof. Ampalavanapillai Nirmalathas, and Dr. Alan Lee provided helpful discussions and suggestions, which contributed to about 5% of the publication.

Publications [2] to [6] contain only the original work of the student, including experiments, analytical models, simulations and manuscripts writing, which contributed to above 90% of the publication. Prof. Christina Lim, Prof. Ampalavanapillai Nirmalathas, and Dr. Alan Lee provided helpful discussions and suggestions, which contributed to about 10% of the publications.

The experimental results in publication [7] were provided by the student, which contributed to about 50% of the publication. Prof. Christina Lim provided the literature review, manuscript writing, which contributed to 40% of the publication. Prof. Ampalavanapillai Nirmalathas and Dr. Alan Lee provided helpful discussions and suggestions, which contributed to about 10% of the publications.

Publication [8] contains the experimental results of the student, which contributed to about 10% of the work. Prof. Christina Lim provided the literature review, manuscript writing, which contributed to 60% of the publication. Prof. Ampalavanapillai Nirmalathas, Dr. Alan Lee, Dr. Chathurika Ranaweera, and Prof. Elaine Wong provided helpful discussions and comments, which contributed to about 30% of the publication.

Table of Contents

Chapter 1 Introduction

1.1 Requirements and Key Enablers for Next Generation Communication Systems

From the first generation (1G) to the fourth generation (4G), mobile communication networks paved the way to a persistent evolution of brand new wireless access technologies, providing end users with faster and ever-improving user experience. However, the next generation mobile communications system, such as the most anticipated fifth generation (5G) mobile network has been often described as a new revolution for wireless access technologies. It is envisioned to provide connectivity to nearly everything and to handle the ever-increasing huge amounts of data traffic with broadband and flexible access [1, 2]. New services and applications such as Internet of Things (IoT), high definition video services and real time control of driverless cars have posed challenges in the achievable data rate, end-to-end latency, reliability, system throughput, and cost-effectiveness on the network.

To meet with these requirements, key enablers including network architecture advancements and the disruptive technologies to improve system throughput have been attracting attention and intensively investigated during recent years [3]. More specifically, three aspects can be considered to cope with the burst in data traffic and high demand on system throughput: incorporating spectrum expansion, realising network densification, and improving spectrum efficiency.

Due to the favourable signal propagation characteristics with frequency below 3 GHz, current cellular networks are mainly operated within this frequency band. Considering the increasing number of new services and burst in data rate, the frequency band below 3 GHz is experiencing spectrum congestion and could barely offer high-speed communications in next generation

networks. To overcome this spectrum congestion, spectrum expansion is necessary to shift the operating frequency bands to above 3 GHz and up to the millimetre-wave (mm-wave) band (30-300 GHz). As the channel propagation characteristics at mm-wave are different from those below 3 GHz, new air-interface and network architecture will be required. For instance, at mm-wave bands, only short distances transmission is possible due to the atmospheric attenuation losses. Mm-wave does not penetrate solid materials very well, either [4]. However, these effects are not necessarily disadvantageous. By using mm-wave spectrum, more compact system can be achieved. Mm-wave frequency allows for more antenna elements to be used at a smaller physical footprint at base station, which could enable the development of massive multiple-input and multiple-output (MIMO) base stations. Combined with Radio-over-fiber (RoF) technique, the mm-wave signals with broadband data can be delivered over long distance fibre links with negligible losses. In addition, rain attenuation can be overcome if small cells, beamforming and massive MIMO, which are inevitable technologies, are introduced. Enhancement of the security of communication is also achievable at mm-wave frequencies due to its unique propagation characteristics.

Network densification is believed to be a promising candidate to meet the requirements in next generation communication systems. It can be achieved through shrinking the cell size, i.e. utilising small cell architectures, to enable better frequency reuse and to minimise the inter-cell interference. The concept of small cells is initially proposed and utilised in wireless communications to mitigate dead spots in large cells and provide hotspots where high speed communication is needed [5]. Later, small cells are investigated in heterogeneous network (HetNet) where small cells are embedded into a microcell network [6]. It is believed that small cells will be designed differently from 4G to satisfy the 5G requirements. Firstly, the propagation characteristics will be different in small cells employing mm-wave frequency band. Secondly, the mobility requirements will be different depending on the application scenarios. For instance, in indoor or hotspot scenario, where most of the data traffic happen, only pedestrian speeds are required. Thus, the system design parameters will be different from macro cell system, where high speed mobility is considered. The deployment of small cells with low transmission power and lower cost is expected to improve cell density and provide high spatial and frequency reuse.

Examples of improving spectrum efficiency include massive MIMO, interference mitigation techniques such as coordinated multipoint (CoMP), non-orthogonal multiple access (NOMA), and small cells mentioned above. Massive MIMO is one of the most important techniques to improve the cell coverage, data rate and system throughput [7]. The performance improvement comes from the increased number of antennas at the transmitter and receiver, which enables significant beamforming gains and multi-user services [8]. The distance between antenna elements will influence the performance and design of massive MIMO. Due to the utilisation of mm-wave frequency signals, the distance can be kept small compared with that in current cellular networks. Overall, massive MIMO plays an important role in future cellular systems and offers improved energy efficiency, spectral efficiency, robustness and secure communication. However, there are still challenges to fully utilise the potential merits, such as synchronisation of large numbers of antenna elements and computational complexity.

Interference mitigation techniques are also actively investigated to improve the spectral efficiency in cellular networks. CoMP joint transmission and reception, a key feature in LTE-Advanced system, is aimed at mitigating the intercell interference and exploits the potential interference for data transmission. The gains achieved by CoMP have been demonstrated in various scenarios [9, 10], but further research is still needed in terms of non-ideal latency between coordinated nodes and accommodating different types of backhaul or fronthaul. In current wireless communication systems, orthogonal multiple access (OMA) scheme is used where different users are allocated orthogonal resources in time, frequency, or space domain. On the contrary, NOMA scheme allows users to transmit signals using the same time and frequency resources, and applying successive interference cancellation technique at the receiver [11]. The overall spectrum efficiency is enhanced by using NOMA and more users can be connected at the same time. Despite the performance gain offered by NOMA scheme, the interference introduced in users with higher channel gain should be further explored and mitigated, as well as the increased computational complexity and latency at the receiver when large numbers of users are grouped into the same NOMA cluster.

1.2 Need and Challenges of Fronthaul

Cloud radio access network (C-RAN) [12], which offers high processing efficiency, less power consumption and high spectral efficiency, is a promising candidate for next generation cellular communication RAN architecture. In C-RAN, the traditional base station (BS)

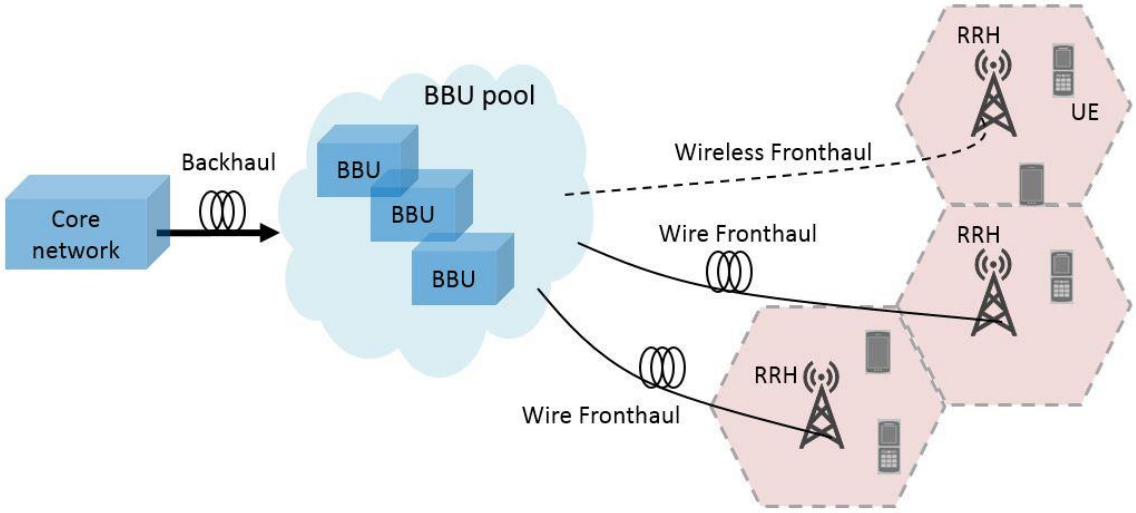

Fig. 1.1 Illustration of C-RAN architecture and wire/wireless fronthaul structures

function is split into two parts: centralised baseband units (BBUs) in a virtualised resource pool and remote radio heads (RRHs) for radio frequency processing. Higher system throughput and less power consumption are possible by moving the RRHs closer to user equipment, likewise cooperative processing techniques and resource sharing facilitated by the centralised baseband processing function at BBU pool. However, the C-RAN performance is constrained by fronthaul [13, 14], the link interconnecting between BBUs and RRHs as shown in Fig 1.1. The reasons of fronthaul being one of the greatest challenges in realising C-RAN are summarised as follows.

To start with, massive deployment of RRHs is required to achieve higher data rates and capacity of increased number of connected users. Hence, fronthauling of large numbers of RRHs becomes complex. Secondly, dark fibre is usually needed for fronthauling large scale RRHs.

Due to the high capacity and high data rate requirements, large numbers of dark fibre are needed that resulting in increased cost for operators to deploy the fronthaul links. Spectral efficient technologies, RoF technique and mm-wave frequency band are therefore attracting attention in industry and academia to provide both high bandwidth and cost-effective fronthaul solutions. Finally, current protocols in fronthaul, including Common Public Radio Interface (CPRI) and Open Base Station Architecture Initiative (OBSAI), also cause problems in realising high-speed fronthaul networks. For instance, CPRI is based on synchronous digital hierarchy-based (SDH-based) transmission mode, thus only constant data rate is possible [15, 16] and the flexibility to accommodate various traffic loads is low. Besides, in CPRI, signals are digitised and transmitted as digital datastream over fronthaul links and the sampling data rate depends on the number of antennas. This feature makes it impossible for future high-speed data rate services and massive MIMO deployment. In summary, more cost-effective fronthaul solutions capable of meeting future customers' demand must be discovered and investigated. New fronthaul interface is required and analog fronthaul options with small cell deployment will play an important role in realising future C-RAN architecture.

The transmission of radio signals over fibre fronthaul link has become attractive due to the growing requirements and the separate advantages of both wireless and wired technologies. To some extent, the combination of optical fibre transport and distribution of radio signals in wireless networks is inevitable and is becoming a necessity in the near future. When combined, namely the hybrid fibre-wireless system, optical fibre and wireless networks are complementary to each other and able to overcome their separate limitations to provide customers with new features. Hybrid fibre-wireless system is also commonly known as RoF system, as wireless signals are carried by optical carriers over optical distribution networks. The fast development of mobile networks also brings an opportunity to develop an evolved network architecture which could enable new applications and services in next generation wireless networks.

1.3 Thesis Outline

The objective of this thesis is to explore cost effective opto-electronic technologies, system architectures and advanced spectrally efficient techniques in hybrid fibre-wireless fronthaul

systems to address the ever-increasing need for network capacity and transmission data rate, thus enabling next generation networks with high mobility and broadband mobile wireless access. Two cost effective 60-GHz RoF fronthaul links are proposed and experimentally demonstrated. Thorough investigations on the link performance are carried out both experimentally and theoretically. Cost reduction design of the proposed system architecture is further investigated using integrated photonic filters in the BBU. To satisfy the stringent requirements of next generation communication networks, advanced spectral efficient techniques such as CoMP and NOMA are studied and employed in the fronthaul network, overcoming the optical bottleneck imposed by existing 60-GHz mm-wave RoF systems. Fronthaul system employing CoMP transmission is demonstrated, serving one user located at the cell boundaries of two small cells. The diversity gain induced by CoMP is exploited to increase the achievable data rate of cell-edge users and to extend the mm-wave small cell coverage. A two-user 60-GHz fronthaul using multi-level code (MLC) based NOMA scheme is experimentally demonstrated. The proposed MLC based NOMA scheme can overcome the practical issues faced by conventional superposition code (SPC) based NOMA scheme, enabling improved received signal quality and spectrum efficiency, low-complexity receiver, and increased cell coverage. A multi-cell NOMA scheme is experimentally demonstrated together with the CoMP function. The benefits include mitigated impact of inter-cell interference on the far users located at cell boundaries of two small cells, as well as improved spectrum efficiency of the system. Finally, analytical model for the NOMA based fronthaul performance in a small cell is presented. The impacts of user distributions, cell size, and number of users in the cell are studied theoretically.

The thesis is organised as follows:

Chapter 2: Literature Review

A comprehensive literature review will be provided in this chapter about the key targets, requirements, and techniques for RoF fronthaul system operating in the 60 GHz mm-wave frequency range. Current fronthaul solutions will be reviewed and discussed to reveal their advantages and challenges such that improvements can be made to better support future large

scale high-speed small cells deployment. A thorough review of the radio-over-fibre technique, which is proved to be a feasible and promising fronthauling approach for future access networks, is carried out and discussed in detail. Optical mm-wave signal generation methods and transmission schemes are investigated as well as the transmission impairments of optical mm-wave signals along analog fronthaul links. Furthermore, advanced techniques to mitigate the inter-cell interference and improve the spectral efficiency, including CoMP and NOMA are reviewed and discussed.

Chapter 3: Physical Layer Fronthaul Options Comparison

In this chapter, two 60-GHz RoF fronthaul links employing modified double sideband suppressed carrier (DSB-SC) and optical single sideband (OSSB) modulation techniques are proposed and experimentally demonstrated. Experimental demonstration, including experimental setup and system BER performance results, is presented. System performance of two proposed fronthaul options are investigated with regard to optical carrier-to-sideband suppression ratio (OCSR), error vector magnitude (EVM) performance comparison, and typical fronthaul system parameters. 60-GHz RoF fronthaul using integrated microwave photonics filters is also investigated aiming at lowering the system cost. Experimental results regarding the system employing integrated photonic filters will also be presented in this chapter.

Chapter 4: Analytical Modeling of Fronthaul Links

This chapter presents the comprehensive theoretical analysis of the two proposed fronthaul links mentioned in Chapter 3. Thorough analytical model of the modified DSB-SC and OSSB links are given, including the 60 GHz mm-wave signal generation, photo-detection and electric frequency down-conversion process. OCSR analysis, the noise process and simulation results for the modified DSB-SC and OSSB systems are also presented. Analytical model matches well with the experimental results and confirms the inherent reason of better performance in the modified OSSB fronthaul system. Finally, the analysis of chromatic dispersion impact on the modified DSB-SC fronthaul link is derived and discussed.

Chapter 5: Advanced Techniques in Fronthaul Networks

This chapter presents the extended study of the advanced techniques, namely CoMP and NOMA, in the fronthaul networks that are promising in mitigating inter-cell interference, improving the cell edge user throughput, spectrum efficiency, and small cell coverage. Firstly, the downlink 60-GHz RoF fronthaul with CoMP transmission is demonstrated, including implementation principle, channel estimation methods, time delay compensation and experimental results demonstration. Secondly, we proposed a MLC-based NOMA scheme in the fronthaul network aimed at improving the system spectral efficiency. The performance improvements of proposed MLC-based NOMA are presented and compared with conventional NOMA scheme based on superposition code (SPC). Furthermore, the feasibility of combined CoMP and NOMA scheme in the fronthaul scenario is verified and discussed.

Chapter 6: Analytical Modeling of Fronthaul Networks based on CoMP and NOMA

In this chapter, a tractable model for RoF fronthaul system based on NOMA with coordinated base stations is developed. The advanced spectral efficient technique of NOMA is further investigated in the context of stochastic demography distribution in a small cell, including three user distribution schemes (user clustering to cell centre, clustering to cell edge and uniform distribution). Besides, two NOMA user pair clustering schemes are presented and discussed. Theoretical investigations of downlink NOMA fronthaul system are demonstrated, including closed-form expressions of effective signal-to-inteference-plus-noise ratio (SINR) and cell throughput containing random number of users and different NOMA clustering schemes. The optimum power allocation ratio to achieve maximum cell throughput in the cell is derived particularly. Finally, simulation results and discussions are presented, including comparison of various user distribution and clustering schemes and the comparison of cell average spectral efficiency in NOMA and OMA fronthaul systems.

Chapter 7: Conclusion

In this chapter, we summarise the conclusions derived from this research project. Future investigation and suggestions are given to shine light upon the direction of research based on the key findings in the thesis.

1.4 Original Contributions

Aligned with the main objective of thesis on cost-effective optoelectronic technologies, archiectures and approaches for the fronthaul of future mobile networks, this section presents major original contributions of the research undertaken. The first set of major contributions stem from this research are related to the proposal, experimental demonstration and theoretical analysis of two 60-GHz radio-over-fibre fronthaul system for future high-speed communication. This is followed by contributions in the form of cost-effective design of 60-GHz RoF fronthaul system employing integrated microwave photonic filters. Another major body of investigation was around the deployment of advanced techniques such as CoMP and NOMA in the RoF fronthaul system that can improve the cell edge user throughout, extend the cell coverage and improve system spectral efficiency. Based on this research, MLC-based NOMA scheme was proposed to improve the system performance and avoid the error propogation effect compared with traditional SPC-based NOMA scheme. This was followed by experimentally demonstrating a fronthaul system utilising CoMP, NOMA scheme and NOMA with coordinated BSs covering up to three users in the small cell, and the theoretical modeling of the fronthaul systems incorporating CoMP and NOMA techniques in a stochastic demography distribution in the small cell. To illustrate the specific contributions covered in each chapter, main original contributions are summarised below. The detailed publications originated from this work are also listed in section 1.5 for convenience.

Chapter 3

Chapter 1

- Proposed and experimentally demonstrated two 60-GHz radio-over-fibre fronthaul options for the next generation mobile communication networks based on a variation of OSSB and DSB-SC modulation techniques, achieving 8-Gbps, 16-QAM signal transmission along 10-km fibre fronthaul link
- Experimentally investigated and compared the link performance, including signal transmission along different length fibre fronthaul and the RF fading effect caused by chromatic dispersion of the two proposed fronthaul candidates
- Proposed and experimentally demonstrated a cost-reduction design of the fronthaul system using two cascaded integrated microwave photonic filters in the BBU to provide a small size and low-cost optical filtering function
- Compared the link performance of fronthaul system employing integrated filters with the system employing Waveshaper and validated that fronthaul link performance can be further improved with smaller insertion loss and steeper roll-off integrated filters

Chapter 4

- Mathematically modelled the proposed two fronthaul systems for analysing the EVM performance using different mm-wave signal generation methods
- Formulated the mathematical expression of the OCSR in two fronthaul systems to validate the impact of RF fading induced by chromatic dispersion
- Studied the noise arisen from the photonic links and electronic components in high-speed fronthaul links and derived the total noise power in the fronthaul system

- Validated the derived fronthaul models with simulation using MATLAB to investigate the EVM performance under different bit rates and fibre lengths of two fronthaul systems
- Built the analytical model of the dispersion induced RF power fading in fronthaul systems and analysed the dispersion impact on the modified DSB-SC fronthaul scheme
- Compared the impact of dispersion on our proposed DSB-SC fronthaul system with traditional DSB modulation based fronthaul system

Chapter 5

- Proposed and experimentally demonstrated a 60-GHz RoF fronthaul network using CoMP transmission to improve the cell edge user throughput and to extend the cell coverage
- Explored the downlink CoMP channel estimation and time delay compensation approaches in the coordinated fronthaul links
- Experimentally investigated the CoMP diversity gain, impact of synchronisation errors and characterised the CoMP fronthaul link performance
- Realised the transmission of 60-GHz RoF signals along fronthaul link using proposed MLC-based NOMA transmission scheme and compared the near/far user performance with that of traditional NOMA transmission based on SPC scheme
- Experimentally investigated the multi-user scenario where NOMA transmission with coordinated fronthaul links is implemented

Chapter 6

Chapter 1

- Built up a generic model of the 60-GHz RoF fronthaul network based on NOMA with coordinated BSs and carried out theoretical studies to demonstrate the feasibility of the proposed scheme
- Further investigated the analytical model of downlink NOMA RoF fronthaul system
- Explored the impact of user distribution, NOMA clustering schemes and noise originated from photonic side in the model to provide a realistic representation of real applications
- Derived mathematical expression of user effective SINR, user throughput and cell throughput employing dynamic power allocation ratio scheme and fixed power allocation ratio scheme
- Investigated the spectral efficiency gain achieved using NOMA and compared the performance with OMA fronthaul system

1.5 Publications

Publications arising from this thesis are listed below.

[1] Y. Tian, S. J. Song, K. Powell, K. L. Lee, C. Lim, A. Nirmalathas, and X. K. Yi. "A 60-GHz Radio-Over-Fiber Fronthaul Using Integrated Microwave Photonics Filters." *IEEE Photonics Technology Letters* 29, no. 19 (2017): 1663-1666.

[2] Y. Tian, K. L. Lee, C. Lim and A. Nirmalathas, "60 GHz Analog Radio-Over-Fiber Fronthaul Investigations." *Journal of Lightwave Technology* 35, no. 19 (2017): 4304-4310.

[3] Y. Tian, K. L. Lee, C. Lim and A. Nirmalathas, "Experimental comparison of DSB-SC & OSSB based 60 GHz radio-over-fiber fronthaul links." In *Microwave Photonics (MWP), 2016 IEEE International Topical Meeting on*, pp. 141-144. IEEE, 2016.

[4] Y. Tian, K. L. Lee, C. Lim and A. Nirmalathas, "Performance Improvement of 60 GHz Radio-over-fiber Fronthaul using Coordinated Multipoint Transmission." 2017 *XXXIInd URSI General Assembly and Scientific Symposium (URSI GASS)*, Montreal, 2017

[5] Y. Tian, K. L. Lee, C. Lim and A. Nirmalathas, "Performance Evaluation of CoMP for Downlink 60-GHz Radio-over-Fiber Fronthaul," 2017 *IEEE International Topical Meeting on Microwave Photonics (MWP)*, Beijing, China, 2017

[6] Y. Tian, K. L. Lee, C. Lim and A. Nirmalathas, "Demonstration of Non-Orthogonal Multiple Access Scheme using Multilevel Coding without Successive Interference Cancellation with 60 GHz Radio-over-Fiber Fronthaul," In *Optical Fiber Communication Conference*, pp. Tu3J-4. Optical Society of America, 2018.

[7] C. Lim, Y. Tian, K. L. Lee and A. Nirmalathas, "Transport schemes for fiber-based fronthaul for transporting 60 GHz wireless signals." In *Transparent Optical Networks (ICTON), 2017 19th International Conference on*, pp. 1-4. IEEE, 2017.

[8] C. Lim, A. Nirmalathas, K. L. Lee, C. Ranaweera, E. Wong, and Y. Tian. "Radio-over-Fiber Technology: Past and Present." In *Asia Communications and Photonics Conference*, pp. S3E-1. Optical Society of America, 2017.

Chapter 2 Literature Review

2.1 Introduction

Future communication networks, such as 5G and beyond, face challenging requirements arising from anticipated use scenarios including Internet of things (IoT), low latency or real time communications (e.g. driverless cars and telesurgery), enhanced mobile broadband [17]. It is well-established that centralised/cloud radio access network (C-RAN) can offer significant benefits to future communication network aiming at high-speed, low latency, high throughput, connection to explosive number of users, and reduced operational and capital expenditure associated with massive small cell deployment. As mentioned in Chapter 1, the fronthaul network between baseband units (BBUs) and remote radio heads (RRHs) is the bottleneck that constraints the realisation of C-RAN architecture as well as the high speed and massive connection requirements of next generation mobile communication. Recent research has identified main enablers for realising the stringent requirements of fronthaul network including small cells for network densification, the license-free mm-wave frequency band, massive MIMO, and advanced spectrally efficient techniques [2, 18-20]. Network architecture improvements, cost reduction design, improved inter-cell interference mitigation techniques as well as new air interfaces are expected to be the main drivers for capacity increase in fronthaul networks.

Among several candidates for fronthaul, analog radio-over-fibre (RoF) technology has been considered as a viable alternative to current digital fronthaul links based on common public radio interface (CPRI) or open base station architecture initiative (OBSAI) [21, 22]. Combined with mm-wave frequency band with large available license-free frequency bandwidth, the analog RoF fronthaul network could provide high-speed, high-capacity optical access. Inter-cell interference is one of the challenges in cellular wireless communication especially with the deployment of large numbers of small cells. Conventional frequency reuse schemes in 2G systems and intercell interference coordination (ICIC) in long-term evolution (LTE 3G/4G) provide solutions to the interference issue with limited gain and spectrum efficiency [19].

Investigation on more advanced interference mitigation technologies such as coordinated multipoint (CoMP) and non-orthogonal multiple access (NOMA) is necessary to offer significant gains at system level.

This chapter provides a comprehensive literature review of candidate fronthaul solutions and key enablers for high-speed and spectral efficient fronthaul network to articulate the motivation for the following topics conducted in this thesis. In Section 2.2, the possible wireless fronthaul candidates including fronthaul network based on free space optical system, sub-6 GHz based fronthaul, Wi-Fi based fronthaul and mm-wave based fronthaul are surveyed. In Section 2.3, wired fronthaul solutions are reviewed mainly focused on optical fronthaul access solutions. Current fronthaul utilising digitised techniques and analog RoF fronthaul is presented in terms of their advantages and limitations. RoF technology is reviewed in detail as a promising solution for future fronthaul network. In addition, the state-of-the-art research achievements in analog RoF fronthaul systems are surveyed. Literature about optical mm-wave signal generation and transmission schemes in RoF fronthaul is discussed in Section 2.4. In Section 2.5, the review on analog RoF fronthaul incorporating CoMP transmission to achieve transmit diversity gain and to mitigate the inter-cell interference is provided. Finally, in Section 2.6, NOMA based RoF fronthaul network aiming at increasing the system spectral efficiency is investigated.

2.2 Wireless Fronthaul Solutions

Efficient fronthauling between the BBU pool and the RRHs is a critical part in realising the C-RAN architecture. Many fronthaul solutions have been studied over the past decade. According to the type of transmission media in fronthaul links, the fronthaul solutions can be classified into two categories: wireless fronthaul links and wired fronthaul links. The illustration of a C-RAN architecture employing different fronthaul solutions is shown in Fig. 2.1.

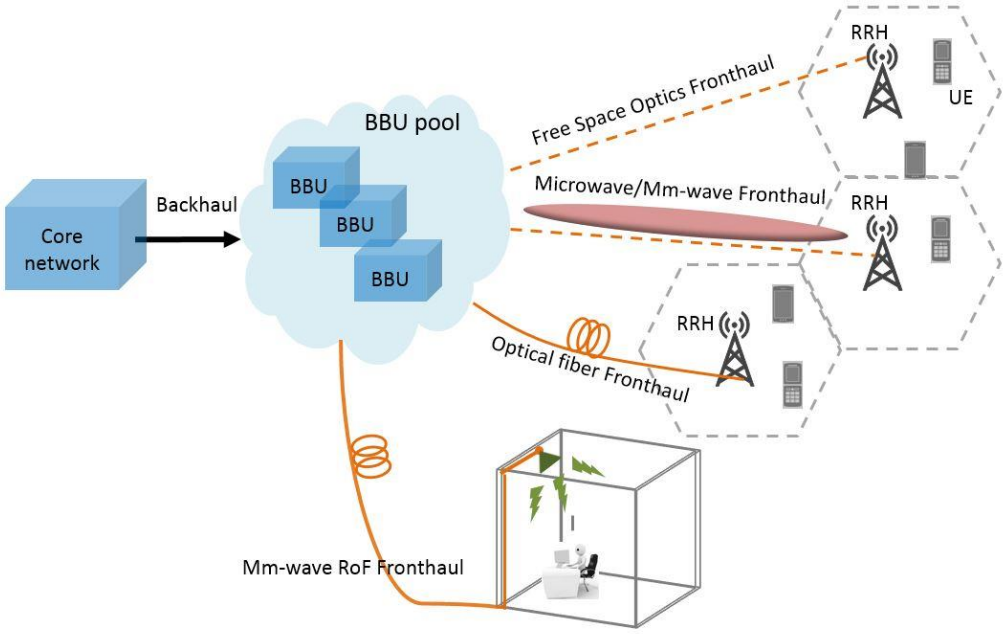

Fig. 2.1 An example of C-RAN architecture and wire/wireless fronthaul solutions. BBU: baseband unit, RRH: remote radio head, UE: user equipment

In this section, wireless fronthaul networks will be investigated and discussed, including the use of unlicensed spectrum around 5-GHz frequency band, free space optical communication and mm-wave frequency band. In [23], theoretical studies were conducted in terms of the system block error rate (BLER) performance in a wireless fronthaul network and proposed two power minimisation schemes with BLER constraints to reduce the fronthaul energy consumption. A joint design of fronthaul and radio access links for a C-RAN with wireless fronthaul links is investigated theoretically in [24]. However, in both papers, the exact frequency bands used in wireless fronthaul links are not specified and thus the wireless signal propagation characteristics are not investigated. The detailed advantages and constraints of using different frequency bands in wireless fronthaul links are presented below.

- *Fronthaul based on unlicensed spectrum around 5 GHz*

Currently 2G, 3G and 4G networks have occupied the most of the low frequency bands and the unlicensed 2.4 GHz and 5 GHz bands are used by Wi-Fi as well. This leads to around 500 MHz unlicensed spectrum band around 5 GHz to be used in fronthaul links. Fronthauling the massive small cells using the unlicensed spectrum around 5 GHz provides two benefits as follows:

Firstly, the cost of purchasing frequency bands for fronthaul links can be saved. Secondly, the spectral efficiency in the low frequency bands can be improved and reuse of the unlicensed spectrum in access links and fronthaul links is possible. However, as the available frequency band is limited, multi-gigabit communication and massive connections are not possible.

- *Fronthaul based on free space optics (FSO):*

Wireless fronthaul network based on free space optics (FSO), which relies on license-free point-to-point narrow optical beams, is a cost-effective solution when line-of-sight (LOS) channel is possible. The advantages of FSO-based fronthaul links include: license-free frequency band (above 300 GHz) which reduces the cost for the fronthaul deployment, directional laser beam can maintain inherently secure and the link will be robust to electromagnetic interference, and wide optical bandwidth available in FSO which enables much higher capacity [25] fronthaul networks compared with other existing fronthaul solutions.

However, there are still some challenges in realising the FSO-based fronthaul option and more research need to be done in the future. First of all, the FSO-based fronthaul links are severely influenced by the weather conditions, especially for long-distance transmissions. In the presence of thick clouds and fog, the link performance degrades greatly [25]. A possible solution is to use hybrid mm-wave/FSO in the fronthaul links [26]. As already known, the mm-wave signals are attenuated by rain rather than fog. Hence, these two techniques will complement with each other during different weather conditions and provide relatively high capacity and link availability. In addition, the cost of equipment, power and maintenance is high in FSO-based fronthaul solution [27] and it is expected to decrease as the technologies enabling FSO fronthaul mature in the future.

- *Fronthaul based on mm-wave frequency band*

The low frequency bands are experiencing spectrum congestion and are not suitable for future ultra-dense small cell deployment. Spectrum expansion by shifting the operation frequency bands to mm-wave band (30-300 GHz) has attracted attention due to the large available bandwidth in this range. Compared with wired fronthaul link solutions, the wireless fronthaul networks using mm-wave frequency bands provide more flexible and dynamic re-

configurations and enable moving networks such as drone-cells in [28]. Besides, mm-wave based fronthaul links can be installed in locations which are too costly or impossible to reach with optical fibres, while providing large capacity at the same time. The modeling and measuring of mm-wave channels have been carried out in many literatures [29-33]. Different feasibility evaluations of mm-wave based fronthaul links have been carried out recently: the suitability of mm-wave frequency bands for transporting fronthaul traffics are examined in [34, 35]; in [36] system level simulation is conducted to evaluate the performances of mm-wave based integrating fronthaul and backhaul (Xhaul); outdoor experiments are conducted in Berlin to shown 16-QAM high capacity fronthaul links over distances up to 185 meters using mm-wave frequency band [37]. It is verified in [37] that mm-wave mesh network can be a feasible solution to support future C-RAN requirements.

However, the mm-wave link performance can be greatly impacted in the presence of rain, which can be solved by using hybrid mm-wave/FSO fronthaul links as mentioned earlier. Another impairment of mm-wave based fronthaul links is the high path loss especially for high mm-wave frequency bands, which means that only short-reach fronthaul link is possible. It should also be noted that only LOS link is possible for both FSO and mm-wave based fronthaul. Thus, optical fibre will be a better choice for inbuilding cells as shown in Fig. 2.1. There is also research on the combination of fibre and wireless fronthaul options [38] to overcome their separate limitations and provide a robust fronthaul solution.

2.3 Wired Fronthaul Solutions

Wired fronthaul solutions consist of coaxial cables and optical fibre. Compared with coaxial cables, fibre is a better choice considering the advantages like light-weight, low loss, high bandwidth, low power consumption and immunity to electromagnetic interference (EMI). In this section, only fibre-based fronthaul solutions will be considered. Signals transmitted over the fronthaul links can be classified into two types: digitised signals and analog signals. Therefore, the review of the optical fronthaul solutions will be divided into two groups: digital fronthaul solutions and analog fronthaul solutions.

2.3.1 Digital Fronthaul

There are three popular fronthaul interfaces currently in use to connect the BBU and RRH, namely CPRI [16], OBSAI [39] and Open Radio equipment Interface (ORI) [40]. Therefore, it is straightforward to develop digital fronthaul solutions to fulfil basic LTE bandwidth requirements in current RANs. However, there are several factors that limit the digital fronthaul solutions to be utilised in future C-RAN.

Firstly, delay and jitter are unavoidable in both CPRI and OBSAI, resulting in degraded performance in high-speed services that require precise synchronisation. Secondly, digitised signals with high sampling resolution are transmitted along fronthaul using the CPRI protocol at the air interface. As a result, the fronthaul links need to transmit much higher bandwidth signals than the actual RF signals [41]. This is not suitable for the future fronthaul link solution considering the anticipated large amounts of data and high data rate requirements. Hence, bandwidth reduction techniques [42] or redefinition of the fronthaul configuration [43] are essential for digital fronthaul links. Bandwidth reduction is mainly achieved by using data compression technique. However, more efficient compression techniques with less distortion and lower latency are still needed to meet the future fronthaul requirements. Redefinition of the function splits between BBU and RRH is a more fundamental method to solve this issue. There are many possible split-function options, but there is a trade-off between inter-cell coordination function with transmission bandwidth [43, 44]. RoF technique assisted by digital signal processing (DSP) [45] has been conducted for mobile fronthaul to improve the signal quality. However, the challenges in bandwidth limitation, unavailability or high-cost of high-speed ADC/DAC operating in mm-wave frequency are still problematic in this approach.

2.3.2 Analog RoF Fronthaul

Considering the limitations of digital fronthaul links mentioned above, analog optical fronthaul approach is being actively researched globally to transmit analog signals along fronthaul links and it shows large fronthaul capacity potential. The transmission bandwidth along analog fronthaul links is the same as the wireless signal bandwidth, thus this technology eases the burden of bandwidth requirements on fronthaul interfaces. The optical bandwidth efficiency

can be fully exploited by using analog fronthaul transmitting advanced modulation format signals [46] [32].

In C-RAN architecture, analog RoF technology enables high-level centralisation and reduced complexity in fronthaul systems. The baseband signal processing and RF signalling happen in the centralised BBU, thus enabling resource sharing and inter-cell coordination among all the fronthaul links and small cells. A centralised mobile fronthaul architecture supporting various radio access structures based on RoF technique is experimentally demonstrated in [21], showing that resource sharing and high capacity can be achieved through efficient centralisation. In [47], a passive optical network (PON) based point-to-multipoint analog RoF fronthaul solution is demonstrated with improved capacity that can accommodate 120 channels of 20-MHz 64-QAM LTE-A signals. However, 3.5-GHz wireless carrier is used which is not suitable for future massive MIMO applications. Analog transport of intermediate frequency (IF)-over-fiber signals has also been demonstrated [48] to transmit 48 20-MHz LTE signals with a data rate of 59 Gbps and round-trip DSP latency of less than 2 μs. On the contrary, the approach of transmitting optical mm-wave frequency signals over analog fronthaul links has the merits of overcoming the constraints of digitised fronthaul while offering large available bandwidth to avoid the spectrum congestion in microwave region [49]. In this situation, the coverage is small of each small cell served by mm-wave frequency bands. Hence, the cost of RRHs should be reduced to facilitate massive deployment of RRHs, which can be realised by using centralised BBU structure in fronthaul networks.

Even through analog RoF fronthaul links achieve simplified cell-site design and solve the issue of bandwidth requirements, it will suffer from the transmission impairments which is less of an issue in digitised fronthaul links [50]. Many research investigations have been done to address the transmission impairments and efficient solutions have been proposed and demonstrated [51]. Optical mm-wave generation and transmission, including the impairments mitigation approaches are surveyed in the next section.

2.4 Optical Millimetre-Wave Generation and Transmission

The spectrum in the millimetre-wave (mm-wave) frequency bands, especially the license-free 60 GHz mm-wave frequency band, has attracted numerous attention and been widely explored in the next generation mobile fronthaul link to provide unprecedented broadband capabilities [52, 53]. Meanwhile, simplified RRH structures with smaller physical footprint are possible utilising the free licensed mm-wave frequency. This in turn enables the cost-effective wide geographical deployment of next-generation small cells.

Photonic mm-wave generation methods can be classified into four groups, namely nonlinear effect based on stimulated Brillouin scattering [54] and four-wave mixing [55], optical heterodyning [56], dual-mode lasers [57] and dual-lasers based on phase locking techniques, and external modulation techniques [58, 59]. Mm-wave generation based on nonlinear effects in waveguide device has low conversion efficiency and high input optical power is needed [60]. The scheme based on optical heterodyning requires two or more optical carriers to be transmitted simultaneously and heterodyning at the receiver to generate the desired mm-wave frequency signals. This scheme requires precisely biased modulator and laser with very narrow linewidth and extremely high frequency stability to acquire acceptable phase noise, which increase the system cost [61]. For dual-mode laser-based mm-wave generation, the mm-wave signal frequency is constant and will not be compatible for future system upgradation. Among the various photonic mm-wave generation methods, external modulation technique emerges as one of the preferred approaches for its ease of operation, relatively low phase noise, and high spectrum purity signals. Basically, the schemes for mm-wave signals generation using external modulation technique include: double-sideband (DSB), optical single sideband (OSSB), and optical carrier suppression (OCS). The schematic representation of generating these modulation formats are shown in Fig. 2.2. In these schemes, mm-wave signals are generated using an external modulator such as Mach-Zehnder modulator (MZM) or electro-absorption modulator (EAM). The modulator is driven by a local oscillator (LO) signal and biased at half transmission point (for DSB and OSSB) or minimum transmission point (for OCS). Upon photodetection at the receiver, the desired mm-wave signal with frequency of f_{mm} can be generated.

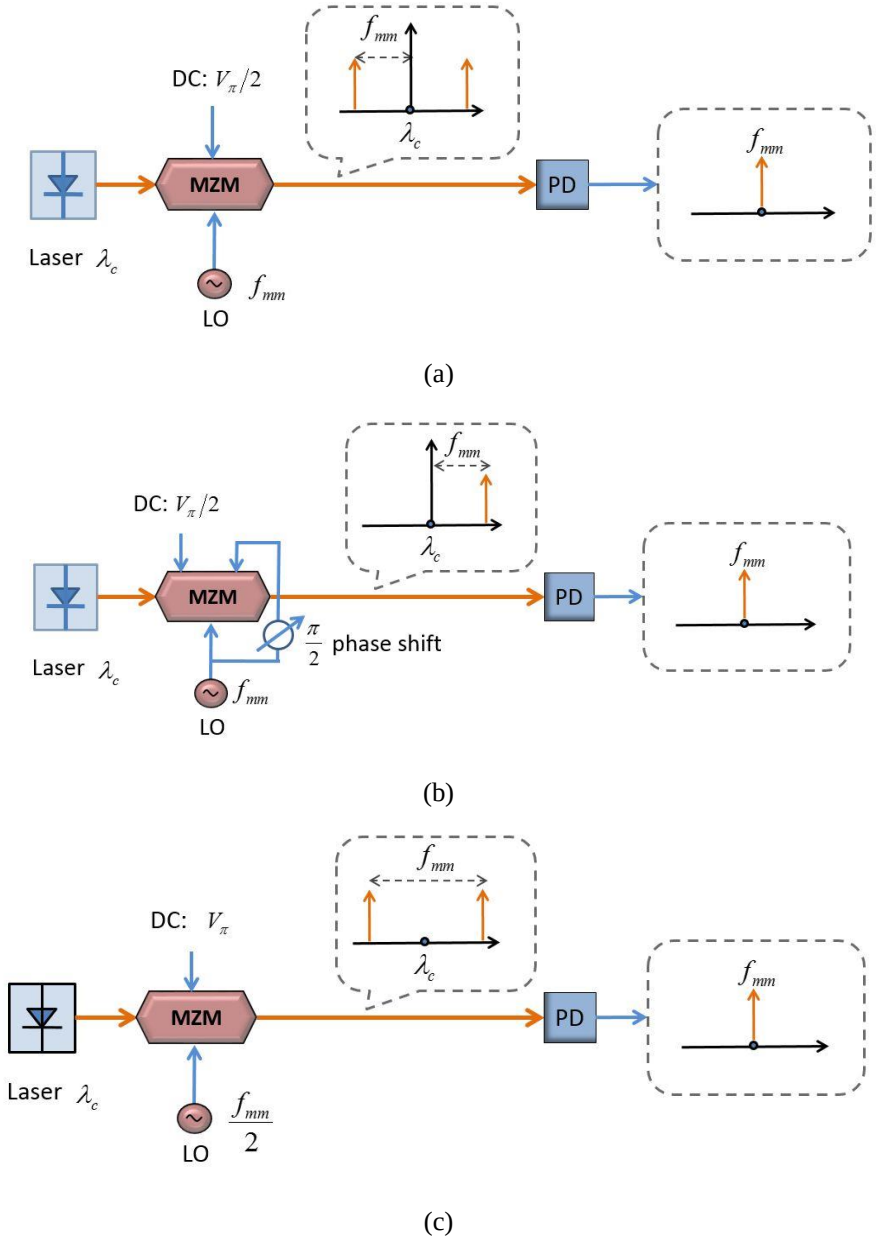

Fig. 2.2 Optical mm-wave signal generation using external modulators. (a) DSB modulation, (b) OSSB modulation, (c) OCS modulation

Among the three schemes, OCS modulation scheme has the highest receiver sensitivity, highest spectrum efficiency and smaller power penalty after long distance transmission [51]. DSB modulation scheme is susceptible to the impact of fibre chromatic dispersion, which limits the

fibre transmission distance severely [62-64] . On the other hand, OSSB and OCS schemes are tolerant to the RF power fading induced by chromatic dispersion and have been extensively explored in the past years [58, 65-67]. In addition, there are also various techniques that have been devised to overcome the dispersion effects in RoF systems, such as external filtering [68, 69], fibre nonlinearities [70] and chirped fibre gratings [71]. Among there dispersion mitigation techniques, OSSB technique offers more flexibility and is easier to implement.

The noise and distortion caused by the nonlinearity of RF and opto-electronic components also degrade the analog RoF fronthaul link performance. Nonlinearity in analog fronthaul links mainly originated from two sources: the optical modulators at transmitter and the RF amplifiers at the RRH. To eliminate the distortion induced by nonlinearity, several linearisation techniques have been investigated [72] including electrical analog linearisation, optical linearisation and electrical digital linearisation. Electrical analog linearisation can be realised by using analog pre-distortion circuit as demonstrated in [73], where both third- and fifth-order nonlinear distortions in 1-6 GHz frequency range can be greatly suppressed using pre-distortion circuit based on two Schottky diodes. Linearisation bandwidth up to 40 GHz is achieved in [74], resulting in more than 10 dB spurious-free dynamic range (SFDR) improvement. Optical linearisation methods include mixed-polarisation [75, 76], dual wavelength [77] and optical channelization [78] have been demonstrated. Typically, optical linearisation techniques can achieve at least 10 dB SFDR improvement. In mixed-polarisation method, the nonlinear components generated by transverse electric (TE) mode and transverse magnetic (TM) mode can be cancelled by each other if they have $n\pi$ phase difference. By controlling the polarisation angles, the second and third order nonlinear distortion can be mitigated. The principle of dual wavelength method is similar to the mixed-polarisation method: nonlinear components at two wavelengths can be suppressed if they are $n\pi$ out of phase. While for optical channelisation, it requires coherent detection at the receiver to cancel the nonlinear distortion [79]. However, digital linearisation approach is not feasible for future high-speed fronthaul links due to the limited bandwidth of analog-to-digital converter. Further investigation is still needed in the digital linearisation approach to simplify the linearisation process and increase the bandwidth.

2.5 Fronthaul Network based on CoMP

For the densely deployed small cells in fronthaul networks, although the utilisation of massive MIMO and beamforming techniques mitigate the impact of large-scale fading and path loss results from long distance transmission, the inter-cell interference is still a factor that will limit the performance such as coverage and spectral efficiency. More advanced wireless communication technologies are also required to provide increased cell edge throughput. Coordinated multipoint (CoMP) transmission and reception techniques have been attracting attention to facilitate cooperative communications across different BSs and cells, and have been adopted in the LTE-Advanced standard [80]. In CoMP, inter-cell interference can be eliminated or even exploited for data transmission and increase user's throughput. The effectiveness of CoMP has been investigated in many literatures. The performance of CoMP transmission and reception is explored for two types of intercell radio resource management configurations through simulation [81]. Field trial demonstration of the feasibility of CoMP with multiple sites and various backhaul solutions are conducted in [10]. The potential benefits and deployment scenarios of CoMP technique in LTE-A system are also evaluated as well as the practical implementation and operation challenges [82]. The focus of these work is on the performance of CoMP technique in LTE-A backhaul systems. However, considering the limitations and challenges of deploying CoMP in backhaul scenarios, employing CoMP in C-RAN fronthaul networks is inevitable for future cellular communication systems.

There are several challenges in employing CoMP in the backhaul systems. To start with, the delay caused by network node processing and the line delay along backhaul and fronthaul links are usually assumed to be ideal [3]. However, in real applications the assumption is not true and will dissatisfy the low latency requirement of 5G networks. Besides, large amount of data, such as channel state information, control signal and user data, need to be exchanged among different cell sites [10], resulting in a severe issue in cell densification. In addition, the cooperating BSs have to be synchronised in time and frequency in order to avoid intercarrier interference and inter-symbol interference in uplink CoMP systems [83]. Synchronisation of signal timing offsets (STOs), carrier frequency offsets (CFOs) [84] and random phase rotation originated from wireless channels are required simultaneously for downlink coordinated links. The overlapped signals from coordinated access points at user equipment make it tougher to

estimate and compensate the different offsets between the two branches. The complexity of downlink CoMP should also be reduced to realise significant diversity gain [10, 85].

An effective solution to bypass the latency, enormous signaling overhead and synchronisation requirements is to deploy the CoMP function in the analog fronthaul links. The centralised BBUs in fronthaul links have the intrinsic advantages of providing much lower latency, readily synchronised phase and frequency local oscillator (LO) signals, as well as handy resources sharing architecture for joint signal processing. Hence, CoMP implementation is of cardinal importance to achieve a significant performance gain in the next generation small cell scenarios. With the centralised architecture of future C-RAN, the performance gain of CoMP can be exploited effectively and in a cost-efficient manner. The resource allocation, clustering of coordinated cells, precoding, interference management algorithms can be located in the centralised BBU pool and the cost will be shared among all the connected users. Typical fronthaul networks employing CoMP techniques in downlink transmission are depicted in Fig. 2.3. Fig. 2.3 (a) shows joint transmission (JT) based CoMP fronthaul links, in which data are transmitted from multiple RRHs simultaneously to a single UE located at the cell boundaries. In this scenario, the data for edge user are shared among various small cells and have been jointly processed in the centralised BBU pool. At a result of the joint transmission, the received signal will be coherently or non-coherently combined at the receiver [86] and the received signal quality can be improved. CoMP based on dynamic point selection (DPS) is illustrated in Fig. 2.3 (b). In DPS-based CoMP network, only one cell will be selected to transmit the signal to edge user in a certain timeslot. This selection depends on the path loss or the channel conditions of two paths. While for coordinated beamforming as presented in Fig. 2.3 (c), data for each user will only be available at one small cell, but the beamforming decisions are made in the BBU coordinatively to cancel the interference from two users located closely at the cell boundaries.

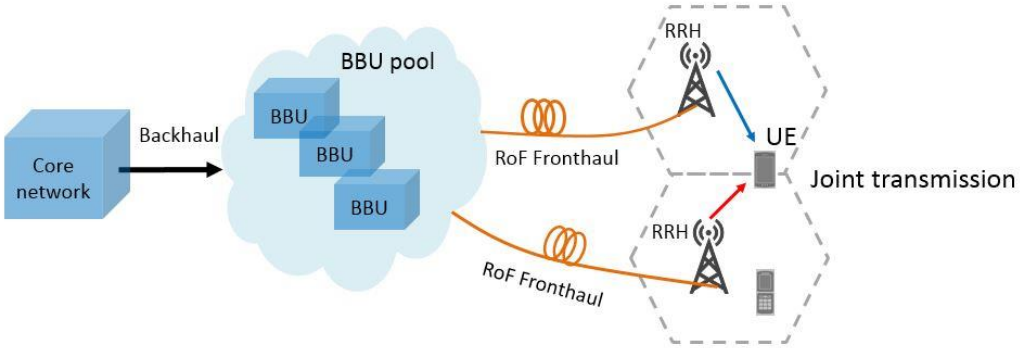

(a)

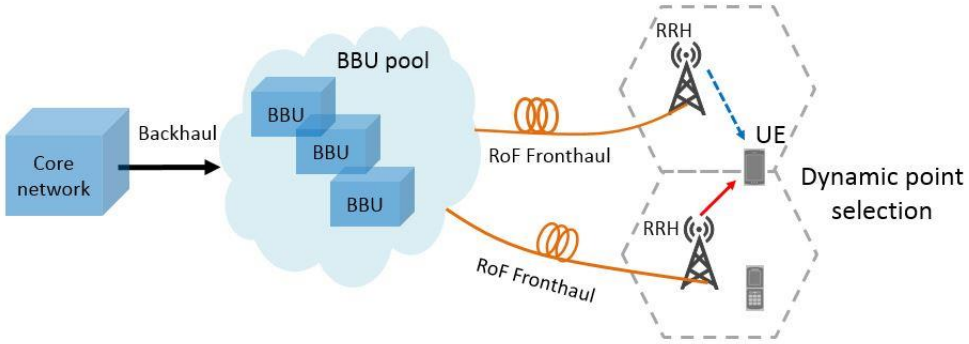

(b)

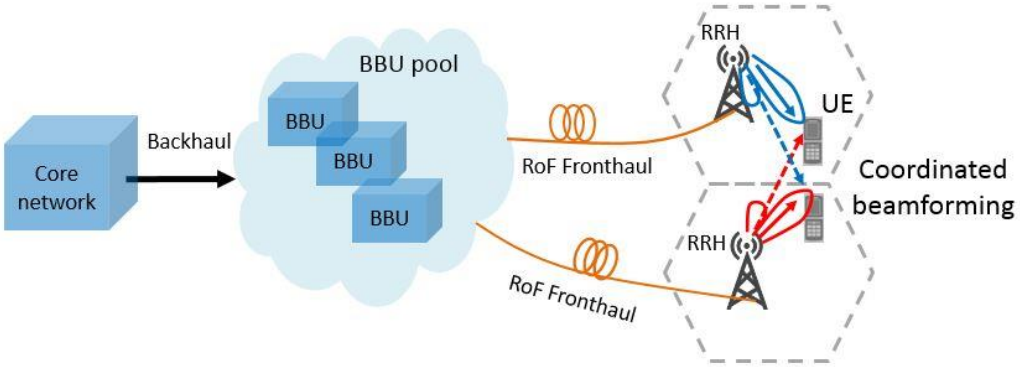

(c)

Fig. 2.3 Downlink CoMP transmission in RoF fronthaul networks: (a) joint transmission, (b) dynamic point selection, (c) coordinated beamforming for interference cancellation

Some research investigations have been performed so far in C-RAN architecture to demonstrate the feasibility of CoMP techniques and evaluate the system performances. In [87], an efficient CoMP scheme with trade-off between cooperation gain and fronthaul consumption is demonstrated. Besides, a queue-aware rate and power allocation scheme for delay-sensitive traffic C-RANs is studied theoretically. It is known that BBU pool in C-RAN is expected to be implemented on general purpose processor (GPP) platform. However, it is challenging to achieve real time CoMP processing on GPP platform due to uncertain scheduling of operating system and unstable processing delay. In [88], a real-time downlink CoMP transmission on GPP platform is implemented using optimised socket design to minimise the data to be exchanged. However, in this work, field tests are still needed in the future to analyse the system performance in real applications and unstable scheduling delay of operating system remains unsolved. An efficient dynamic nested clustering algorithm is proposed in [89] that can improve the system scalability greatly and baseband signal processing and channel estimation can be simplified. Robust compression technique in distributed uplink cloud radio access network has been developed to leverage more advantageous channel conditions in neighbouring cells [90]. Precoding and decoding design for CoMP technique has also been investigated in the C-RAN structure recently. For instance, a downlink antenna selection scheme is conducted using regularised zero forcing precoding method [91]. The optimisation of joint antenna selection and power allocation scheme to maximise the average weighted sum rate has also been investigated in [91] through simulations. In [92], network power consumption minimisation approach for C-RAN in both downlink and uplink is proposed using optimising the precoding vectors. Potential solutions to combat the impact of fronthaul-constrained radio access networks on large scale coordinated signal processing and resource allocation optimisation were discussed in [13].

There have been extensive theoretical studies on the CoMP technique in future cloud radio access networks as mentioned above. However, there are only limited number of experimental demonstrations of CoMP transmission in mm-wave RoF fronthaul systems. A photonic-aided CoMP transmission with space-frequency block coding (SFBC) in mm-wave RoF system was demonstrated in [93-95] to attain CoMP gains. Experimental results show that the CoMP RoF system achieves 3-dB improvement in received optical power and transmission distance of the 60-GHz wireless signal is extended by more than 50%. The CoMP performance in fronthaul

networks in terms of the impact of imperfect knowledge of channel state information (CSI), impact of synchronisation and uplink performance still need to be evaluated experimentally.

2.6 Fronthaul Network based on NOMA

The increased need for real-time services, such as online gaming, video streaming and telesurgery, makes it increasingly important to improve the system spectral efficiency (SE). In wireless communication systems, there are two critical limiting factors to achieve high spectral efficiency, namely the interference problem and the optimal radio resource usage [96]. Inter-cell interference will be a crucial issue in future small cell deployment scenarios as more users will be located at the cell edge. The CoMP technique is expected to mitigate and exploit the interference and provide diversity gain for cell edge users as elaborated in last section. The use of license-free mm-wave in future small cell deployment also facilitate the improvement of system SE, since more active frequency re-use will be possible among small cells. Optimised radio resource management is also important to obtain full exploitation of the radio resources. First, we will give a brief review of existing research investigations in terms of improving SE, and then we will focus on the NOMA enabled fronthaul networks for improved SE.

In 4G networks, orthogonal frequency-division multiplexing (OFDM) has been adopted using orthogonal subcarriers to enhance the bandwidth utilisation of multi-carrier systems. However, frequency offset in OFDM systems can lead to inter-carrier interference (ICI) and severely degrade the performance. Much higher spectral efficiency can be obtained by overlapping the subcarriers intentionally and violating the orthogonality rule, leading to the technique known as spectrally efficient frequency-division multiplexing (SEFDM). The concept of SEFDM was first proposed in [97] to handle smaller ICI than those of OFDM. The detailed investigation of SEFDM is given in [98] where the trade-off between the bandwidth gain and the receiver complexity is discussed. Experimental results with regard to the feasibility of SEFDM in optical domain are demonstrated [99] with bandwidth saving up to 25% compared with optical OFDM technique. SEFDM has also been adopted in mm-wave RoF systems for beyond 4G cellular networks. A first experimental demonstration of the SEFDM in RoF system is presented in [100] with a data rate of 36 Mbps. SEFDM has also be employed in 60 GHz mm-wave RoF systems to increase the achievable data rate without altering the signal bandwidth

and modulation format, and 3.75-Gbps 4-QAM SEFDM signal is transmitted experimentally with the data rate increased up to 67% compared with OFDM signal transmission [101]. However, the challenges on the SEFDM systems with regard to the complexity in detection remain unsolved and need further investigation.

Recently, NOMA has been introduced in analog fronthaul transmission system to satisfy the large number of connected users in the small cells. Numerous investigations have been carried out to exploits the high spectral efficiency of NOMA in wireless communications in the last decades [102-105]. As the name indicates, NOMA is achieved using non-orthogonal resource allocation and can accommodate much more users compared with traditional orthogonal multiple access (OMA) techniques. In conventional OMA schemes, signals are multiplexed in frequency/time/code domain, while NOMA schemes achieve multiplexing in the power or code domain. The employment of NOMA technique offers increased system throughput, increased SE, and has the ability to accommodate massive connectivity. The optimal approach to achieve NOMA is to share the same time/frequency resources among users while multiplexing users' information in power domain [102, 106]. Some other techniques to achieve non-orthogonal multiple access have also been proposed and investigated, such as code-division multiple access (CDMA) [107-109], pattern-division multiple access (PDMA) [110], bit-division multiple access (BDMA) [111, 112] and interleave-division multiple access [113]. However, these techniques introduced redundancy via coding/spreading to facilitate users separation at the receiver, thus leading to reduced SE in the system [114]. A thorough investigation of different NOMA schemes in 5G systems in terms of their principles, key features and advantages and limitations is presented in [115].

Fig. 2.4 shows the principle of downlink 2-user NOMA scheme using power domain multiplexing. Signals of multiple users are multiplexed in the power domain linearly at the transmitter using superposition code (SPC) and successive interference cancellation (SIC) is required for multi-user signal detection at the receiver side [102]. The far user (UE2 in Fig. 2.4) will be allocated more power than the near user (UE1). At UE2 receiver, the received signal is directly decoded using single user detection approach and treated the UE1 signal as interference. While at UE1, the receiver will first estimate far user's information and cancel it using SIC. Then UE1 signal can be decoded after SIC.

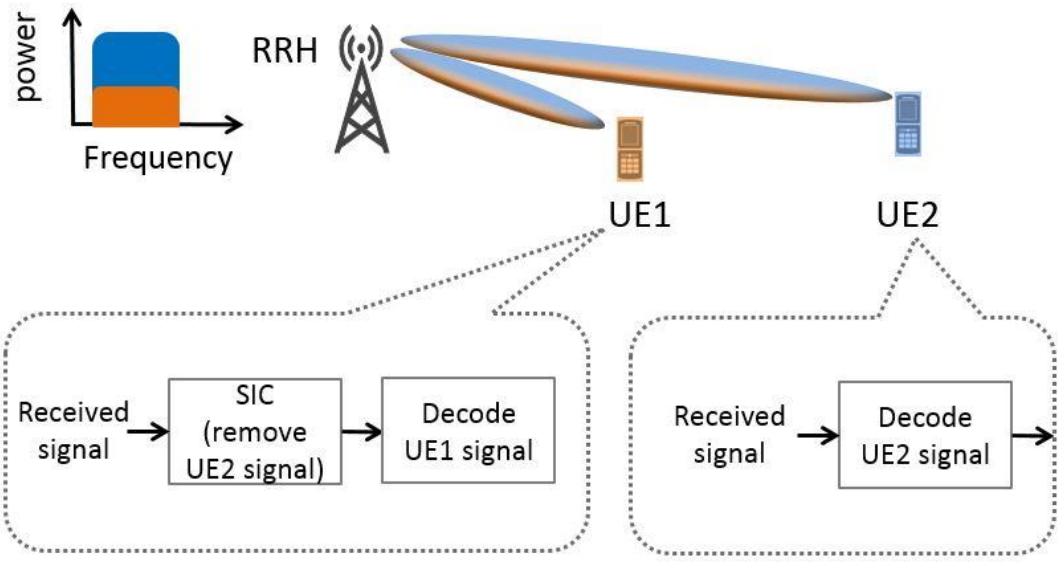

Fig. 2.4 A downlink 2-user NOMA using SPC at transmitter and SIC at receiver.

The non-orthogonal feature of NOMA improves system throughput and SE significantly and has been investigated both theoretically and experimentally. The feasibility of digital domain NOMA transmission over 25-km single-mode fibre is demonstrated in [116] and nearly doubled system SE can be achieved with proper FEC coding. The performance of NOMA in visible light communication (VLC) system is evaluated theoretically [117] and the mathematical expression of system coverage probability is derived and shows the existence of optical power allocation ratio in a 2-user NOMA cluster. In [118], the experimental results show that NOMA performance in VLC system can be further improved using a phase pre-distortion method. Since transmission power is allocated to various users differently according to their channel conditions in NOMA, user clustering, fairness and optimal power allocation methods become critical in the system design. Lots of literatures have focused on these issues in NOMA based systems. Dynamic user clustering to achieve user fairness is investigated in [119] and three sub-optimal algorithms are proposed to balance the trade-offs of complexity

and throughput of the user with worst channel conditions. The impact of power allocation on the user fairness performance of NOMA in 5G systems is explored [120]. Power allocation schemes to guarantee quality of service (QoS) [121] and optimal power and subcarrier allocation schemes [122, 123] are also theoretically studied. As an essential component of 5G mobile networks, the performance of NOMA with randomly deployed users in 5G scenarios is theoretically studied in [11]. Besides, applications of NOMA scheme are fully reviewed in [124], including its combination with the promising techniques such as MIMO and CoMP, and the interplay between NOMA and cognitive radio. The performance of NOMA in mm-wave cells is presented in [125] to exploits the large available bandwidth and improved spectral efficiency. Up to 70% channel capacity gain can be obtained in NOMA based mm-wave cells compared with conventional OMA schemes. NOMA has been jointly deployed with CoMP technique to offer improved spectral efficiency while maintain reduced inter-cell interference simultaneously [126-128].

Even through NOMA can provide attractive benefits as mentioned above, there are still some challenges to deploy NOMA in real applications. These challenges include increased error propagation that will degrade the system performance, trade-off between user performance and the receiver complexity, and increased latency induced by SIC at the receiver. NOMA technique without using SIC method has been proposed in literature [129] to reduce the complexity at receiver. Theoretical results from [130] suggests that Gray labelling provides better performance than natural labelling and non-Gray labelling in terms of symbol error rate, where no SIC is performed at any receiver. Further research on how to mitigate the influence of error propagation and NOMA without SIC scheme is still needed to realise NOMA applications in real scenarios.

2.7 Summary

In this chapter, a comprehensive literature review of the key technologies and approaches seeking to address the challenges in the fronthaul of future generations of mobile networks with significant amount of small cell deployment have been investigated. In particular, various fronthaul solutions, optical mm-wave signal generation and transmission, and advanced techniques such as CoMP and NOMA in the context of optical fronthaul approaches have been

analysed. In Section 2.2, wireless fronthaul solutions including fronthaul based on unlicensed spectrum around 5 GHz, fronthaul using free space optics, and fronthaul based on mm-wave frequency band are reviewed. The advantages and challenges of each fronthaul solutions are also discussed. In Section 2.3, optical fronthaul solutions are investigated. The limitations of digital optical fronthaul approaches are analysed and the motivation of employing analog optical fronthaul schemes are elaborated. Section 2.4 reviewed the optical mm-wave signal generation and transmission methods in fronthaul scenarios. Besides, the impairments of mm-wave signal transmission along optical fronthaul links are studied. The transmission distance of optical mm-wave signals is severely limited by RF power fading caused by fibre chromatic dispersions. Several techniques that can solve this issue have been surveyed. In addition, noise and distortion caused by nonlinearity of components are studied in detail in analog fronthaul links as well as the methods to mitigate these impairments. In Section 2.5, CoMP transmission and reception technique aimed at reducing inter-cell interference and improving system spectral efficiency is thoroughly reviewed and discussed. Previous research activities of CoMP technique focus on deploying CoMP in backhaul links, but there exist several challenges makes it unavailable for future high speed radio access networks. The effective method of deploying CoMP in fronthaul links is presented. The state-of-art research of CoMP based fronthaul systems are surveyed. Future directions of CoMP based fronthaul systems are also provided. In Section 2.5, a brief review of existing investigations in terms of improving system spectral efficiency is given. Then NOMA schemes that can provide significant SE improvement are discussed in detail. The operating principle of NOMA in a 2-user cluster is demonstrated. The limitations of code domain NOMA are also provided, followed by motivation and current research studies on power domain NOMA. Finally, the limitations and future directions of power domain NOMA are presented.

Chapter 3 Experimental Comparison of Physical Layer Fronthaul Options

3.1 Introduction

The massive volume of data we are experiencing today which is expected to further increase in an explosive manner in the near future has put stringent requirements on the network capacity, data rate, and the number of connected users. To cope with the rapid proliferation of network data traffic, various techniques have been investigated, including small cell architectures, millimetre-wave (mm-wave) frequency radio-over-fibre (RoF) networks [131-133] and massive MIMO [19, 134]. Among them, the license-free spectrum in the 60-GHz mm-wave frequency band is appealing with high bandwidth availability and thus could effectively accommodate the requirements for high data traffic. To enable future densely packed small cells transmitting mm-wave radio signals, analog RoF network is attractive in providing low loss, high bandwidth and cost-effective solutions for fronthauling these small cells.

On the other hand, to enable future deployment of the fibre-based fronthaul next-generation wireless network, it is imperative to maintain high reliability while minimising the overall cost [135]. Therefore, low-cost deployment of analog mm-wave RoF based fronthaul will be one of the key considerations. To reduce the cost of the system, a centralised baseband unit (BBU) is utilised in the fronthaul network to enable resource sharing among large numbers of remote radio heads (RRH). Besides, generating the mm-wave frequency signals in the electrical domain is not economically viable with the need of high-speed electrical components [136] such as RF mixers and oscillators operating at the 60 GHz or even higher frequency bands. These electrical components are either expensive or not commercially available. In this regard, generating mm-wave signals in the optical domain is attractive for the RoF fronthaul applications. Photonic mm-wave signal generation offers high throughput RoF fronthaul links

for the next generation radio access and has the ability to overcome the limitations imposed by the electrical components.

Many investigations and studies have been carried out with photonic mm-wave generation and transmission in the analog links [54-56, 58, 59]. However, there is a lack of systematic and thorough experimental demonstration and comparison of these schemes for fronthaul networks operating at frequency up to 60 GHz. Hence, in this chapter, we firstly proposed and experimentally demonstrated two fronthaul solutions to generate broadband analog 60 GHz photonic mm-wave frequency signals using cascaded external modulators to meet the requirements of high data rate, high bandwidth and improved capacity of the future fronthaul networks. Modulation techniques used in these two solutions include the popular double sideband suppressed carrier (DSB-SC), optical carrier suppression (OCS) and optical single sideband (OSSB) modulation schemes. Our proposed two schemes are named as modified DSB-SC scheme and modified OSSB scheme in this context. Secondly, a cost reduction design of the proposed fronthaul network is demonstrated using integrated photonic filters in the BBU to optimise the fronthaul system. Microwave photonic filters offer more compact and reconfigurable features compared with the traditional microwave filters. Meanwhile, the simplification of RRH structure is enabled by moving the baseband signal processing functions to the centralised BBU. The resource sharing among large numbers of RRHs is also possible in the centralised BBU, which further helps in lowering the hardware cost.

This chapter is organised as follows:

In Section 3.2, the principle and operation of the proposed two fronthaul schemes are introduced. In Section 3.3, the systematic experimental demonstration of the proposed modified DSB-SC and modified OSSB fronthaul options are explained and discussed, including the experimental setup, the optical-to-carrier-suppression ratio (OCSR) comparison, the error vector magnitude (EVM) performance, and the parameters used in the experiments. Section 3.4 presents the cost reduction design of the proposed fronthaul network where compact and low cost integrated microwave photonic filters are used in the BBU to perform the optical filtering function. Finally, a summary of the investigations is provided in Section 3.5.

Chapter 3

3.2 Principle of Downlink 60 GHz Analog Radio-over-Fiber Fronthaul Schemes

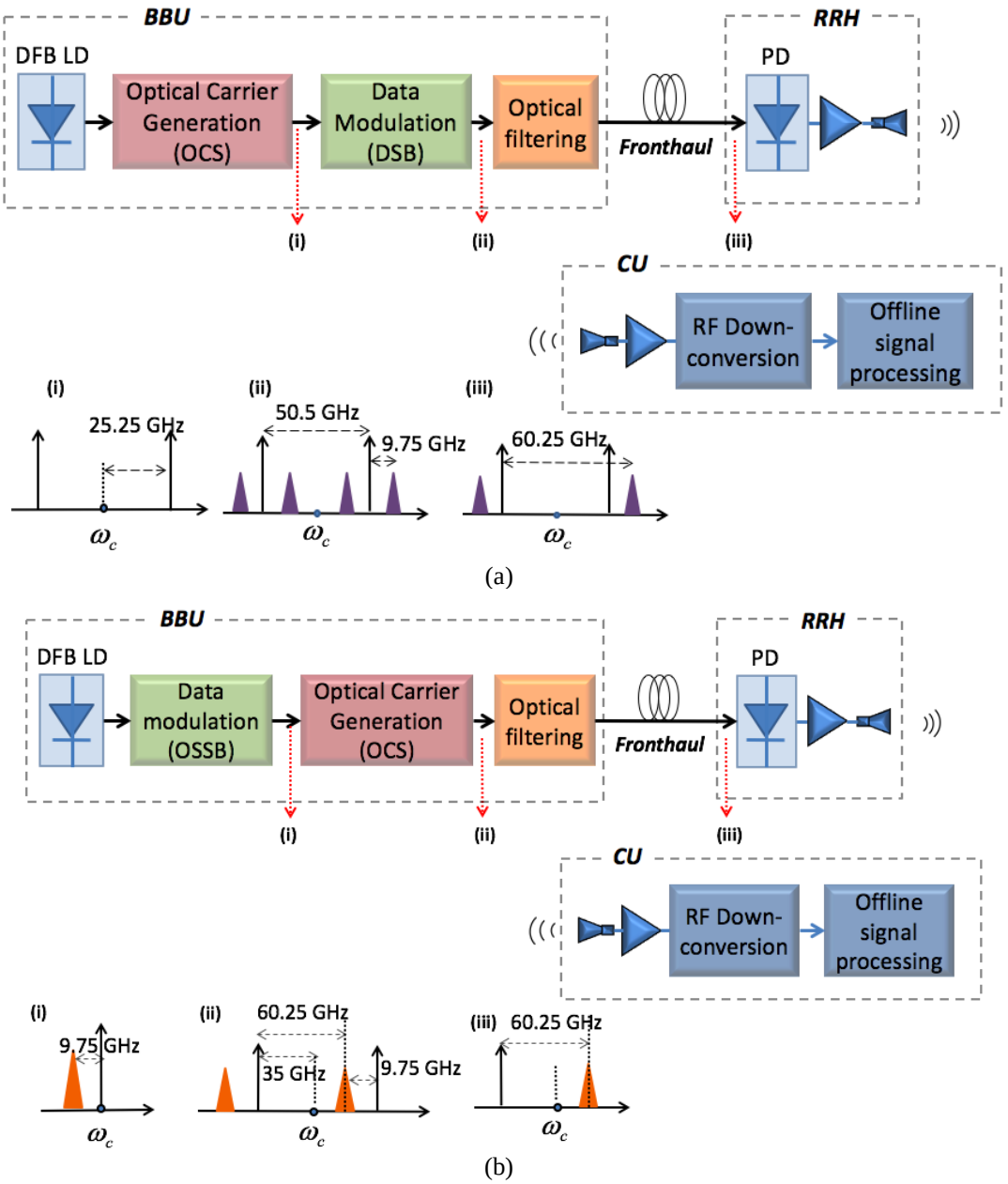

Fig. 3.1 The principle of proposed radio-over-fibre fronthaul links employing (a) cascaded OCS and DSB modulation (DSB-SC system) and (b) cascaded OSSB and OCS modulation techniques (OSSB system).

Fig. 3.1 shows the block diagram of the proposed mm-wave RoF architecture for the two proposed fronthaul schemes, namely the modified DSB-SC system and modified OSSB system. In both schemes, the BBU performs two basic functions: 60-GHz photonic mm-wave

carrier generation and data modulation. Fig. 3.1 (a) depicts the schematic of the modified DSB-SC scheme. DSB-SC technique is used in the first modulation stage to generate two optical carriers with a frequency separation of 50.5 GHz and a quadrature amplitude modulation (QAM) signal with an intermediate frequency (IF) of 9.75 GHz is modulated onto the two optical subcarriers in the subsequent data modulation module. In the experiments, the optical filtering function is performed using a Waveshaper (WS), acting as a highly programmable optical filter to remove undesired frequency components before the optically modulated mm-wave signals are transmitted along the front-haul link. As we can see in the Fig. 3.1 inset (iii), the optical signal transmitted along the fronthaul link is a variation of the traditional DSB-SC modulation. Upon detection at the Remote Radio Head (RRH), mm-wave signals with frequency up to 60.25 GHz are generated for wireless transmission. Finally, mm-wave signals are received and down-converted in the customer unit (CU), followed by offline signal processing using MATLAB.

The schematic shown in Fig. 3.1 (b) is the modified OSSB fronthaul option, where OSSB technique is utilised to modulate the IF QAM signal (9.75 GHz) onto an optical carrier and the following OCS modulation is employed to generate the desired 60.25 GHz mm-wave optical signal. The WS acts as an optical filter to remove the residual optical carrier component, the upper-sideband optical carrier, and the lower-sideband RF signal after OCS modulation, to minimise saturation of the photodiode. The resulted optical spectrum is a variation of the traditional OSSB modulation as shown in inset (iii) Fig. 3.1 (b). The WS removes the additional noise and optical carrier components to achieve better performance as well as enabling a fair comparison of the two schemes.

3.3 Experimental Demonstrations for Analog RoF Fronthaul

3.3.1 Experimental Setup

To investigate and compare the performance of the mm-wave RoF link with different modulation techniques, we have experimentally demonstrated two schemes operating at 60.25 GHz mm-wave frequency band carrying 4 QAM signals with bit rates of 2.5 Gbps and 5 Gbps, and 16 QAM signals with bit rates of 5 Gbps and 8 Gbps, respectively.

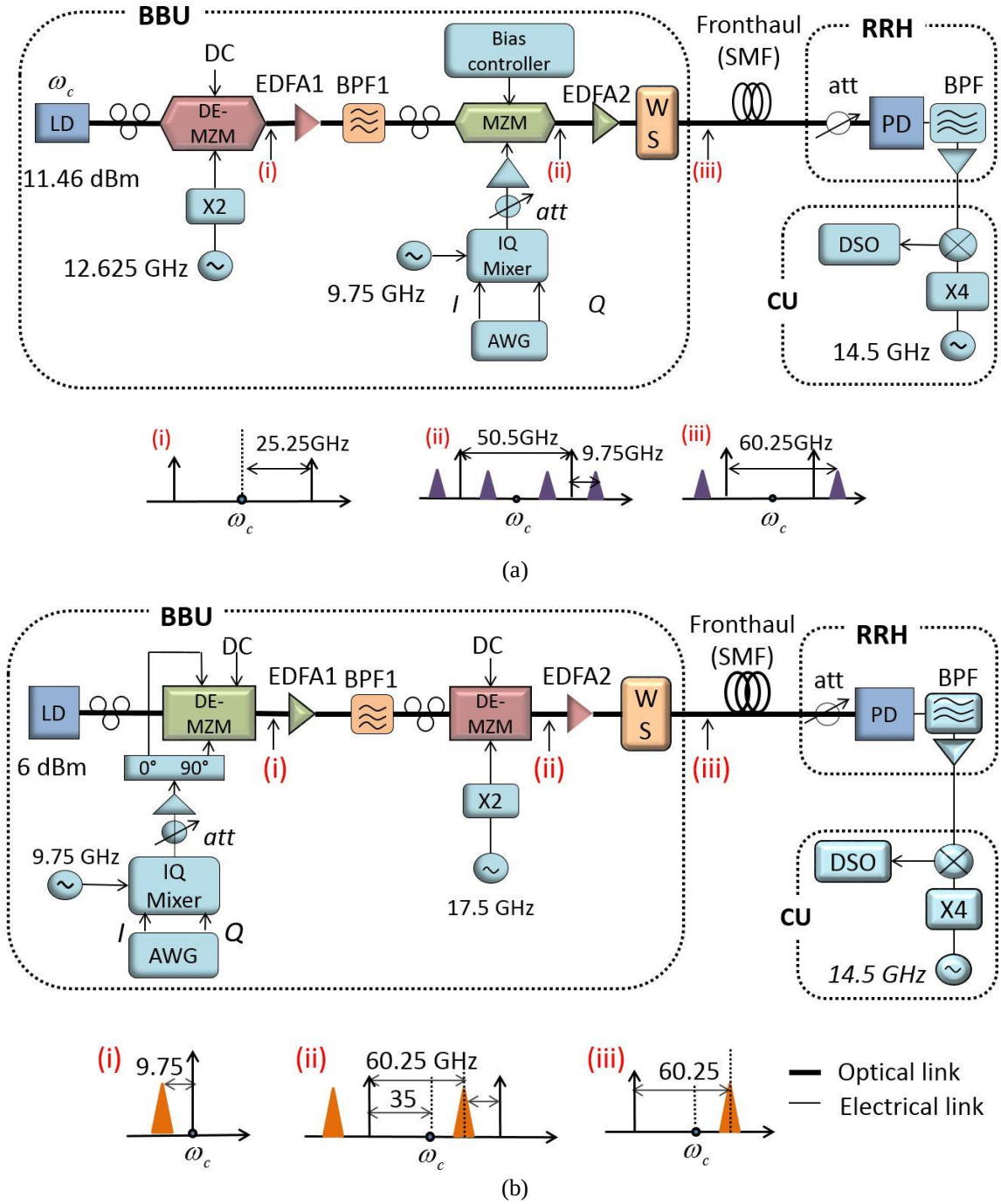

Fig. 3.2 Experimental setup for (a) modified DSB-SC scheme and (b) modified OSSB scheme. X2: frequency doubler. X4: frequency quadrupler. att: attenuator. WS: waveshaper. BBU: baseband unit. RRH: remote radio head. CU: customer unit. WS: waveshaper.

Fig. 3.2 presents the experimental setup for the 60.25 GHz mm-wave RoF fronthaul link configurations of the proposed DSB-SC scheme and OSSB scheme showing the theoretical spectra of optical mm-wave signals in the insets. In both schemes, the two cascaded Mach-

Zehnder modulators (MZMs) located at the BBU were utilised to provide optical mm-wave signal generation and data modulation functions, respectively. Due to the lack of high-speed single electrode MZM in our laboratory, a 40-GHz dual-electrode MZM (DE-MZM) was utilised as an alternative to achieve the OCS modulation (the first DE-MZM in Fig. 3.2 (a) and the second DE-MZM in Fig. 3.2 (b)). In the data modulation stage, the QAM signal generator is composed of a Tektronix 10 GS/s dual-output arbitrary waveform generator (AWG7102), a double balanced IQ mixer and a 9.75-GHz LO signal source. The in-phase (I) and quadrature phase (Q) components of QAM signal were generated using Matlab and then loaded into the AWG. The balanced I/Q outputs were applied to the double-balanced IQ mixer, where an LO signal was used to up-convert the QAM signal to 9.75-GHz IF frequency.

3.3.1.1 Modified DSB-SC scheme

The experiment setup for the RoF fronthaul system with modified DSB-SC scheme is shown in Fig. 3.2 (a). In the BBU, a distributed-feedback laser diode (DFB LD) at 1550 nm with an output power of 11.46 dBm was externally modulated by a 40 GHz DE-MZM. Only one electrode of the first DE-MZM was driven by a 25.25-GHz RF signal, while the other electrode was terminated. This DE-MZM was biased at minimum transmission point so that OCS signal with a frequency separation of 50.5 GHz was modulated onto the 1550 nm continuous-wave (CW) optical carrier. In the second stage, the 9.75-GHz IF QAM signal was first attenuated using a 4-dB attenuator to avoid saturating the 12.5-Gbps driver amplifier. After amplification, the IF signal had a peak-to-peak voltage of 3.4 Volts. It was then modulated onto the two optical subcarriers using a JDS Uniphase 10-Gbps zero chirp single drive intensity modulator biased at the quadrature point using an ultra-compact dither-free modulator bias controller to achieve the DSB modulation. The low-noise Erbium-doped fibre amplifiers (EDFA1 and EDFA2) were used to compensate for the insertion loss of the MZMs. A bandpass filter (BPF1) was used to remove out-of-band amplified spontaneous emission (ASE) noise. To minimise the polarization-dependent losses, a polarisation controller (PC) was used before each of the modulation stages. The Waveshaper (WS) used in our system was a Finisar WaveShaper 4000S Multiport Optical Processor based on high-resolution Liquid Crystal on Silicon (LCoS) technology, allowing full control of amplitude and phase characteristics of the targeted optical signals. The WS has a custom-designed filter profile to drop the lower signal sideband of the

upper optical subcarrier and the upper signal sideband of the lower optical subcarrier (as illustrated in Fig. 3.2 (a) inset (iii)), thus generating an almost ideal 60.25-GHz DSB-SC equivalent optical signal.

This 60.25-GHz optical signal was then transmitted along the fibre-based fronthaul link connecting the BBU and RRH. The 60-GHz photodetector (PD) located at the RRH was utilised to convert the optical signal into 60.25-GHz electric signal, which was then filtered and amplified before being radiated into the air. At the customer unit (CU), the signal was down-converted to recover the QAM data. Note that no wireless link was demonstrated in the current experiment stage, due to the non-availability of 60-GHz antenna in our laboratory when the experiment was carried. Driven by a 58-GHz signal generated by quadrupling a 14.5 GHz LO signal, the mixer down-converted the wireless signal to an IF carrier frequency of 2.25 GHz. This signal was then acquired by a Tektronix TDS6154C 40-GS/s digital storage oscilloscope (DSO). Time synchronisation, IF down-conversion, decision feedback equaliser (DFE) for nonlinearity correction, QAM demodulation, and error vector magnitude (EVM) evaluation were performed using Matlab offline processing.

3.3.1.2 Modified OSSB scheme

Similarly, the experiment setup for the RoF fronthaul link with mm-wave generation using cascaded OSSB and OCS modulation technique is illustrated in Fig. 3.2 (b). A CW lightwave was generated by a DFB LD with an output power of 6 dBm at 1550 nm and then externally modulated using a 20-GHz DE-MZM biased at the quadrature point with a 90° phase shift between the two IF QAM signals driving the two arms of the modulator. The 90° phase shift was introduced via a 90° hybrid coupler with a 2-dB insertion loss. The output power of laser in the modified DSB-SC scheme (11.46 dBm) is higher than that of the modified OSSB scheme (6 dBm). The reason is that the DE-MZM in DSB-SC scheme was biased at minimum transmission point, resulting in much higher insertion loss compared with the OSSB scheme. Higher output power of laser in DSB-SC scheme is needed to compensate for the high insertion loss. The peak-to-peak voltage of the signals driving the two arms was 3.4 V for fair comparison with the modified DSB-SC scheme. In the second stage, a minimum-biased 40-GHz DE-MZM was utilised to generate two optical carriers with a frequency spacing of 70 GHz. Note that, only one electrode of the second stage DE-MZM was driven by a 35-GHz RF

signal, while the other electrode was terminated. The second stage DE-MZM adopted the OCS modulation, generating two duplicate OSSB signal sidebands located on both side of the already suppressed centre optical carrier (1550 nm). The Waveshaper in OSSB scheme had a different filtering profile as that in the DSB-SC scheme. Here in the OSSB scheme, the lower sideband signal of lower optical carrier and the upper sideband optical carrier will be removed in order to generate an OSSB signal with frequency separation of 60.25 GHz. (as shown in Fig. 3.2 (b) inset (iii)). EDFA2 with 25 dB gain was used to compensate for the insertion losses of the MZM and the optical path. The RRH and CU perform similar functions as that in the DSB-SC scheme. After photodetection in RRH and RF down-conversion in CU, the signal will be recovered using Matlab offline processing.

We ensure that both schemes were operated at their optimum conditions for fair comparison.

3.3.2 Experimental Results and Discussions

3.3.2.1 Optical-Carrier-to-Sideband Ratio (OCSR) Comparison

Fig. 3.3 and Fig. 3.4 present the optical spectra for the two investigated schemes before photodetection measured using an optical spectrum analyser with 20-MHz (0.16 pm) resolution bandwidth. As depicted in Fig. 3.3, before optical filtering using WS (blue), the suppression ratio between the centre optical carrier and two optical subcarriers is more than 30 dB. The centre components exist due to the fact that this component cannot be completely suppressed during the OCS modulation stage. The upper and lower optical subcarriers each carries double sideband RF signals. After the filtering function, the higher order harmonics and centre optical components are suppressed. The optical-carrier-to-sideband ratio (OCSR) is 31.7 dB. The large OCSR is due to the weakly modulated mm-wave signals, i.e. the low modulation efficiency of the second stage data modulation module

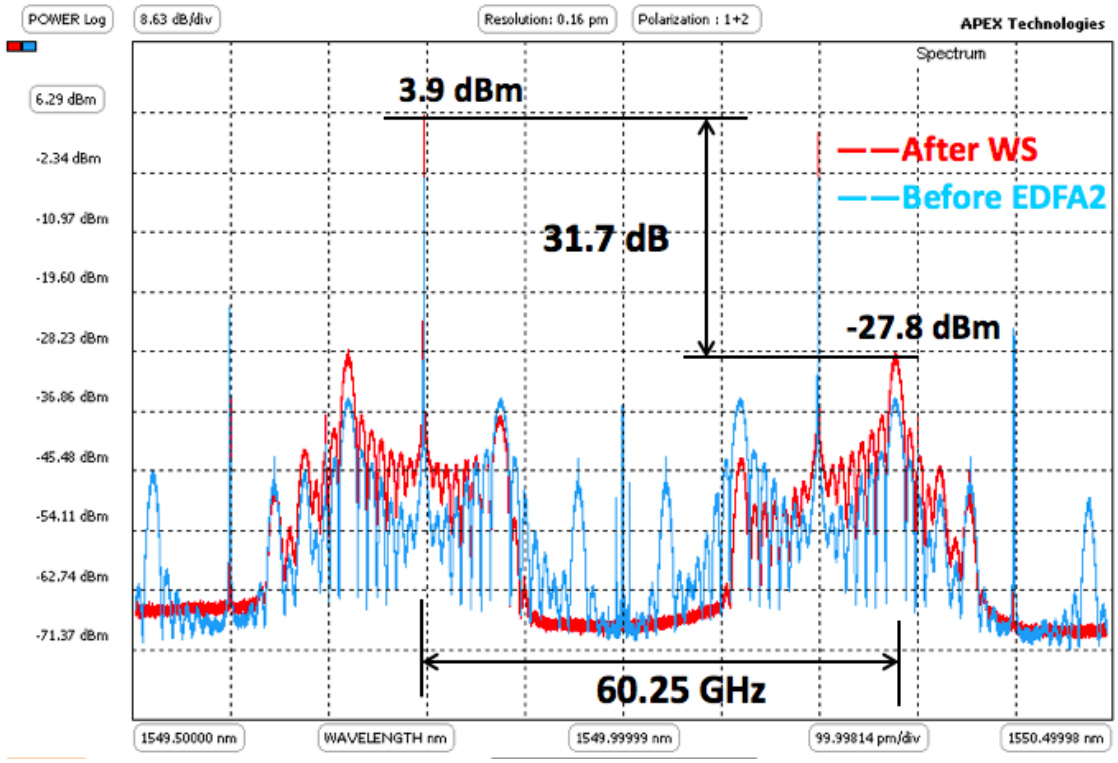

Fig. 3.3 The optical spectra for the modified DSB-SC fronthaul scheme before EDFA2 (blue) and after the Waveshaper (red).

Shown in Fig. 3.4 are the optical spectra for the modified OSSB scheme. As shown in this figure, the residual optical carrier and lower sideband wireless data are completely suppressed after passing through the WS; the upper sideband optical subcarrier is also suppressed. The resulting optical spectrum contains the optical carrier and corresponding QAM signal with a frequency spacing of 60.25 GHz. The OCSR is 25.2 dB, resulting from the much higher modulation efficiency compared to that of DSB-SC system. Smaller OCSR up to 0 dB is possible in both systems with custom-designed filter profile using the WS, leading to improved system performance for the proposed fronthaul options.

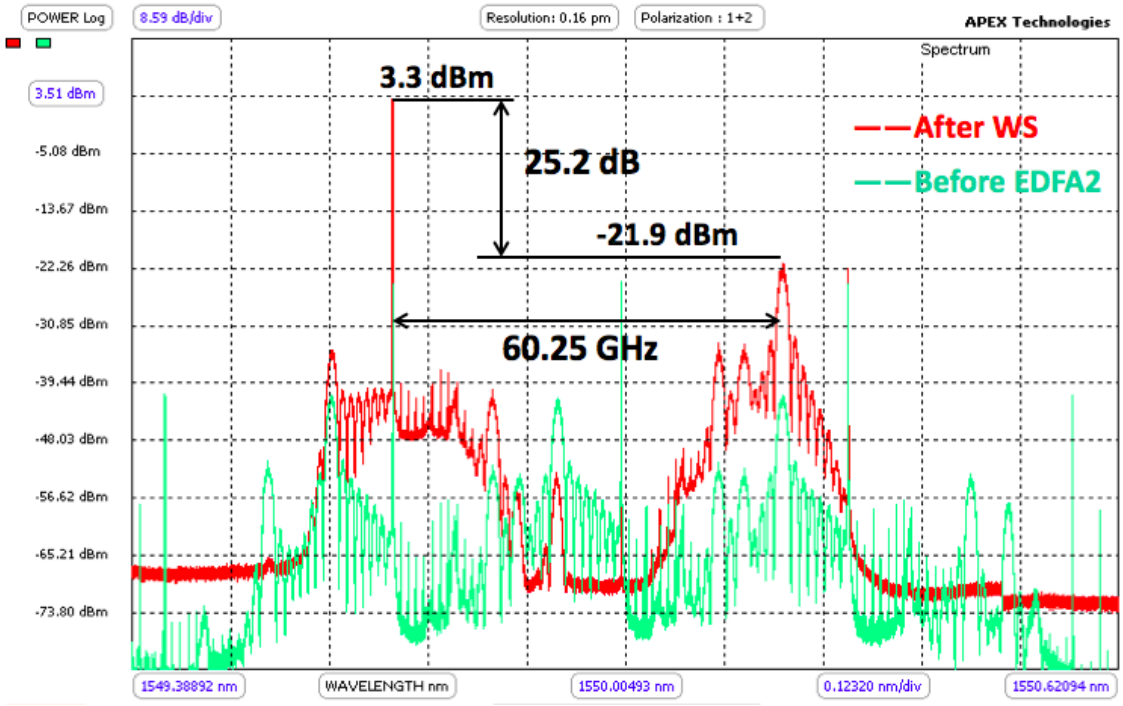

Fig. 3.4 The optical spectra for the modified OSSB fronthaul scheme before EDFA2 (green) and after the Waveshaper (red).

3.3.2.2 EVM performance analysis

In order to compare the performance of the proposed RoF links and the scalability to bit rate, the modified DSB-SC and modified OSSB systems were tested in the 60-GHz band transmitting 4 and 16 QAM signals with different bit rates and different fronthaul distances. The received QAM signals were obtained for different received optical power to the PD controlled by a tunable optical attenuattor. The calculated error vector magnitude (EVM) against received optical power for 4 QAM (resp. 16 QAM) signal for both OSSB and DSB-SC analog fronthaul links are illustrated in Fig. 3.5 (resp. Fig. 3.6).

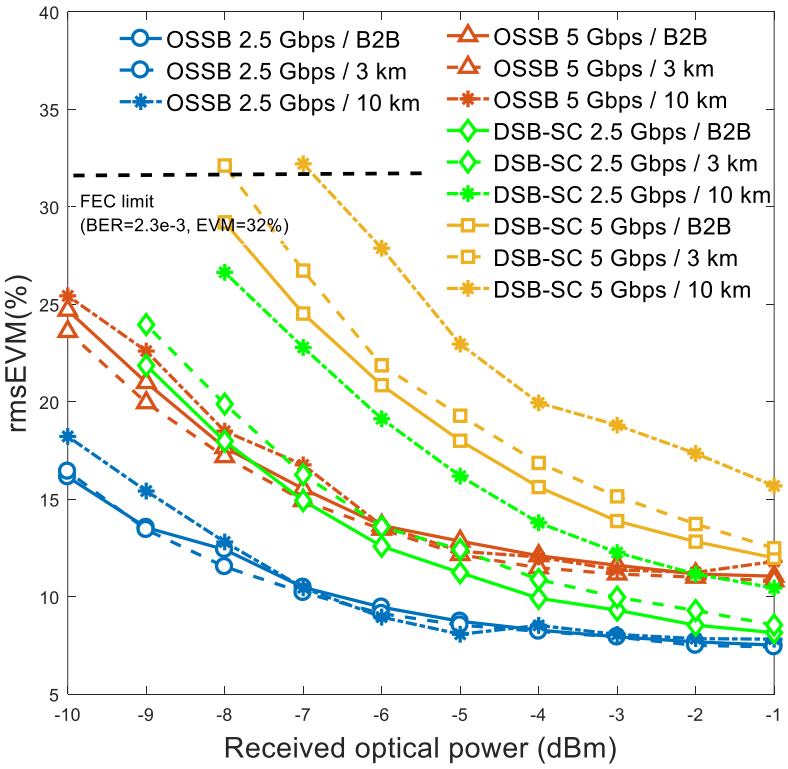

Fig. 3.5 rmsEVM against received optical power for DSB-SC and OSSB systems with 4 QAM signals for different bit rates.

For 4 QAM signal transmission shown in Fig. 3.5, 2.5-Gbps and 5-Gbps data rate were transmitted to evaluate the link for different lengths of fronthaul links. As can be seen from the curves, higher data rate in DSB-SC and OSSB schemes will result in the degradation of link performance because of the increased signal bandwidth. The back-to-back (B2B) transmissions offer the baseline for the system performance. When we increase the fronthaul transmission distance from 3 km to 10 km, there is minimal impact on the OSSB scheme. However, the performance of the DSB-SC scheme degrades significantly with increasing fronthaul transmission distance with a power penalty of ~0.5 dB and ~2 dB for 3 km and 10 km, respectively, for 4 QAM transmission. The calculated EVMs for 4 QAM signals are well below the forward error correction (FEC) limit with 7% overhead, corresponding to a bit-error-rate (BER) of 2.3×10^{-3} and approximately 32% EVM in the experiment. Some examples of the specific FEC coding are convolutional code, low-density parity-check (LDPC) coding, and Reed-Solomon code.

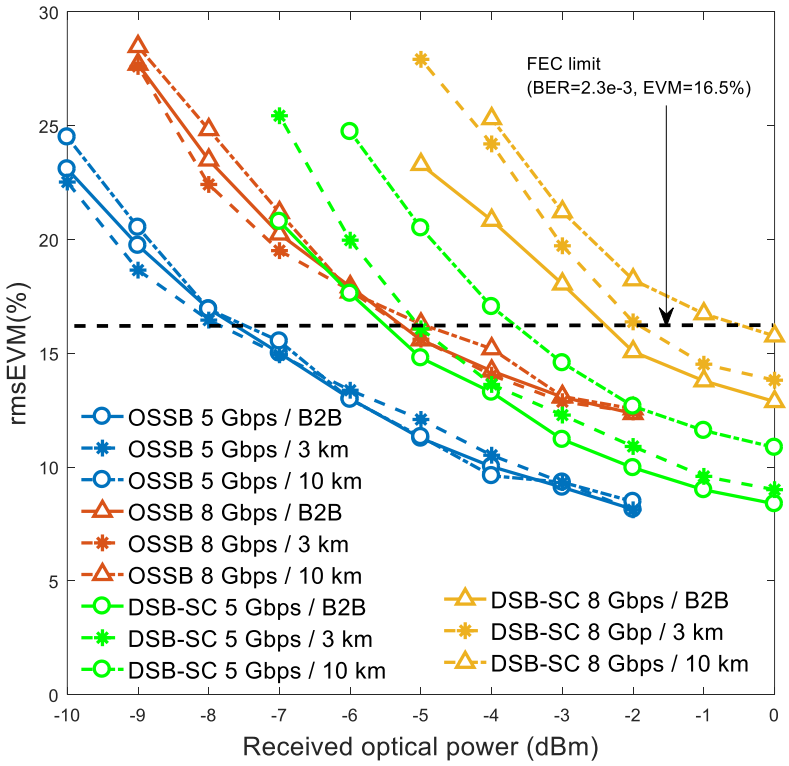

Fig. 3.6 rmsEVM against received optical power for DSB-SC and OSSB systems with 16 QAM signals for different bit rates.

Similarly, for 16 QAM signal transmission depicted in Fig. 3.6, OSSB scheme outperforms DSB-SC scheme with 2.5 dB lower receiver sensitivity at the FEC limit (BER=2.3x10^{-3}, EVM=16.5%) for 5-Gbps back-to-back signal transmission. However, when the bit rate was increased to 8 Gbps, the DSB-SC scheme cannot obtain error-free reception within the FEC limit for transmission over 10-km fronthaul link.

Hence, we conclude that OSSB scheme provides better receiver sensitivity for both 4 QAM and 16 QAM signals. This is mainly due to the higher modulation efficiency (lower OCSR) of OSSB system compared to DSB-SC system. Higher bit rate is realised at the cost of receiver sensitivity for the two schemes. The maximum bit rate in our experiment is 8 Gbps, limited by the bandwidth of our BPF (59-61.5 GHz) located at the RRH. Higher data rate can be achieved with a bandpass filter of higher bandwidth. Besides, the OSSB scheme can overcome fibre chromatic dispersion effect in short-reach analog fronthaul link.

In Table 3.1, we summarise the system parameters of the two schemes. As we can see, the OSSB fronthaul option requires a lower laser emission power and achieves smaller OCSR, leading to better receiver sensitivity. However, the DSB-SC option requires lower frequency LO signals, smaller bandwidth MZM and lower EDFA gain in the BBU, leading to reduced system cost. Considering these trade-offs, when deploying RoF fronthaul networks in real scenarios, the two mm-wave fronthaul can be selected according to the requirements (fronthaul distance, system cost, etc.) of the fronthaul applications.

Table 3.1 Comparison of Modulation Schemes

Parameters	***DSB-SC System***	***OSSB System***
Laser Power	11.46 dBm	6 dBm
LO Frequency	Up-convert: 12.625 GHz Down-convert: 14.5 GHz	Up-convert: 17.5 GHz Down-convert: 14.5 GHz
MZM type & Bandwidth	40 GHz DE-MZM, 10 Gbps amplitude modulator	20 GHz DE-MZM, 40 GHz DE-MZM
OCSR	31.72 dB	25.2 dB
Optical Amplification	EDFA1: 25 dB EDFA2: 15 dB	EDFA1: 25 dB EDFA2: 25 dB
Receiver Sensitivity at FEC limit	5 Gbps 4 QAM: -7.7 dBm 8 Gbps 16 QAM: -2.6 dBm	5 Gbps 4 QAM: -10.2 dBm 8 Gbps 16 QAM: -5 dBm

3.4 Mm-Wave RoF Fronthaul Using Integrated Photonics Filters

3.4.1 Principle of Operation

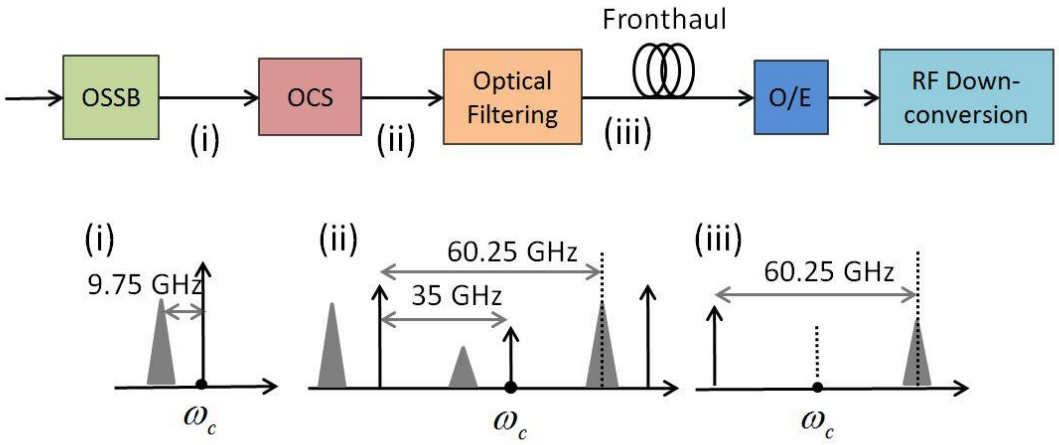

Fig. 3.7 Block diagram of the analog 60 GHz RoF fronthaul link employing cascaded OSSB & OCS modulation techniques for photonic mm-wave signal generation.

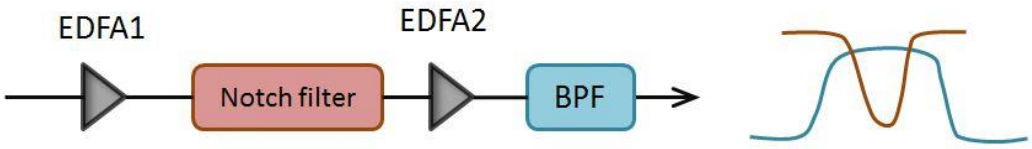

Fig. 3.8 Cascaded notch filter and BPF performing optical filtering function and the resulting filter profile with dual-passband.

In this section, we experimentally demonstrated a 60.25-GHz RoF fronthaul employing two compact and low cost integrated filters. The fronthaul link scheme used here is the modified OSSB fronthaul option as described in Section 3.2. In this demonstration, the WS in the BBU is replaced by the integrated filters to provide the optical filtering function. The block diagram is illustrated in Fig. 3.7. The detailed principle of operation for data modulation and mm-wave carrier generation in the BBU is the same as that described in Section 3.2. Here we only demonstrate the operating principle of the optical filtering module as depicted in Fig. 3.8.

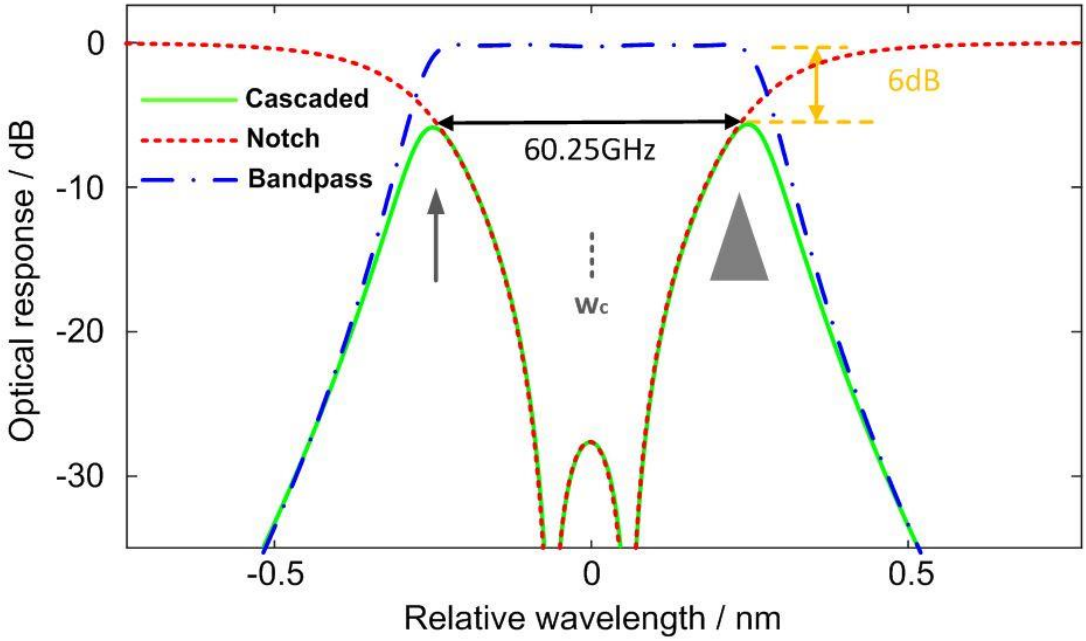

Fig. 3.9 Simulated amplitude of the cascaded (green solid line), notch (red dash line) and bandpass (blue dash dot line) filters.

The optical filtering module comprises two integrated filters (a BPF and a notch filter) and two EDFAs. The notch filter is composed of two resonators laterally coupled with a pair of bus waveguides, thus achieving a narrow stopband with enhanced rejection ratio and slope steepness [137]. The simulated amplitude of the notch filter with ring radii of 9 μm is shown as the red dash line in Fig. 3.9. Due to the weak electromagnetically induced transparency (EIT)-like behaviour, a rejection ratio as high as 27.5 dB can be achieved throughout the stopband. On the other hand, a 6^{th} order coupled resonators optical waveguide (CROW) structure which consists of six identical microring resonators are employed to suppress the undesired out-band frequency components. To obtain a BPF with a bandwidth of 70 GHz, the ring radii of the BPF are set to a value of 4 μm [138, 139]. Fig. 3.9 shows the simulated amplitude of the BPF filter as well as the overall amplitude of the optical filtering module. It can be seen that a dual transmission band with a frequency separation of 60.25 GHz is successfully achieved after cascading two integrated filters, thus ensuring the correct filtering of our 60 GHz signals over the RoF fronthaul links. Two EDFAs are used to compensate for the insertion loss of the integrated filters.

Finally, in the CU, IF QAM signal was acquired by frequency down-conversion using a local oscillator signal. Time synchronisation, IF down-conversion, decision feedback equalisation, phase estimation and QAM demodulation were post-processed offline in MATLAB.

3.4.2 Experimental Setup and Results Discussions

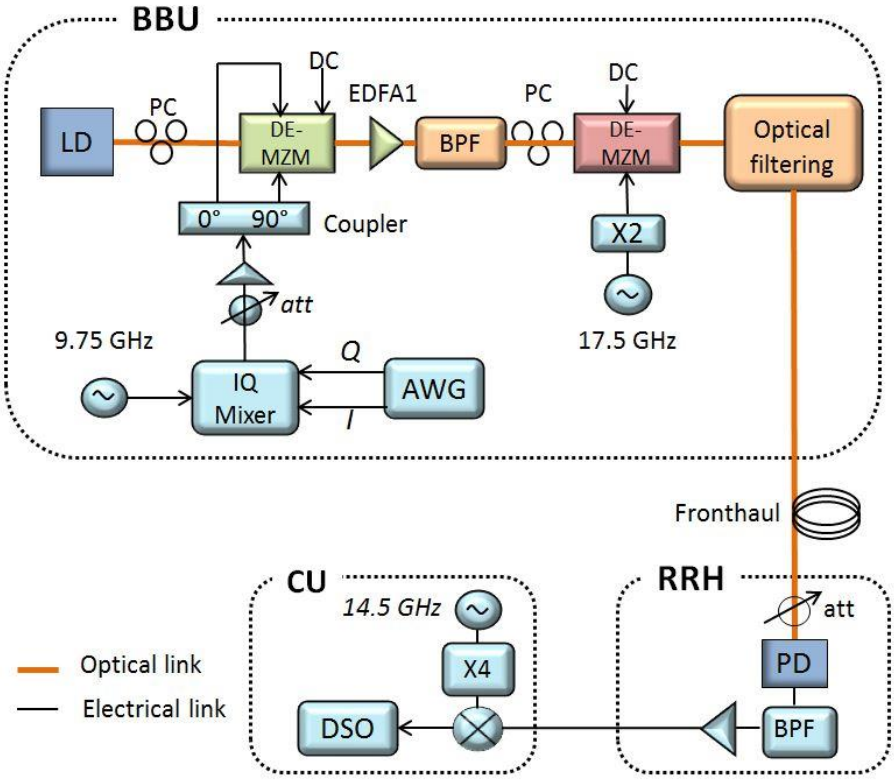

Fig. 3.10 Experimental setup for 60 GHz RoF fronthaul link. LD: laser diode. X2: frequency doubler. X4: frequency quadrupler. PC: polarisation controller. att: attenuator.

Fig. 3.10 depicts the experimental setup for the integrated filters enabled 60-GHz RoF fronthaul link. The experimental setup is similar to that of the modified OSSB scheme in Fig. 3.2 (b), except that the Waveshaper is replaced with the optical filtering module composed of cascaded integrated filters and EDFAs (Fig. 3.8). The description of the principle and operation of the experimental setup is explained in detail in Section 3.3. In this section, we only focus on the performance of the RoF fronthaul link employing the proposed optical filtering module.

The optical filtering module is necessary to remove the undesired frequency components and out-of-band ASE noise. Eliminating the undesired frequency components has the merits of

avoiding the saturation of photo-detector and increasing the optical signal-to-noise ratio (OSNR). Future upgrades such as interleaving signals from multiple channels and sub-carrier multiplexing will also be possible with a clean optical spectrum.

3.4.2.1 Optical Filtering using Waveshaper

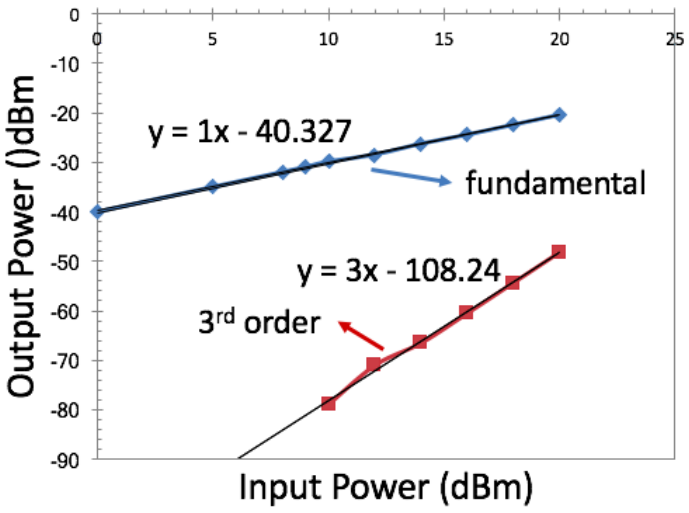

Fig. 3.11 SFDR of the system with Waveshaper

We first demonstrated the fronthaul system with the optical filtering function performed by an EDFA followed by the WS as a reference. The WS used in our system was a Finisar WS 4000S Multiport Optical Processor based on high resolution Liquid Crystal on Silicon (LCoS), allowing full control of amplitude and phase characteristics. The custom designed filter profile was a dual-passband BPF with a separation of 60.25 GHz to emulate the filter profile of the cascaded integrated filters. We measured the spurious-free dynamic range (SFDR) of this link configuration using two tone RF signals with frequency of 9.74 GHz and 9.76 GHz. Fig. 3.11 shows the slope of the fundamental frequency component curve and the third order response curve. The Output System Noise Floor was measured to be -98.33 dBm/Hz. Then the SFDR ($63.9\ \mathrm{dB \cdot Hz^{2/3}}$) was estimated from Fig. 3.11.

3.4.2.2 Two Cascaded Integrated Filters

We then replaced the WS with the two integrated filters as illustrated in Fig. 3.12 (a). The two cascaded integrated filters were fabricated on a silicon-on-insulator (SOI) wafer via ePIXfab

and utilised to remove the undesired frequency components. The insets of Fig. 3.12 (a) show the scanning electron microscope (SEM) images of the fabricated integrated optical filters. The height and width of the silicon core waveguide is 220 nm and 450 nm respectively, for both the bus and racetrack waveguide. Tuning the integrated bandpass filter and the notch filter with a tuning rate of 15.11 °C/nm was achieved via separate heating or cooling of the filters using thermo-electric modules. The optical response of two integrated filters would drift in wavelength when the temperature changes. The reason is that the refraction index of silicon depends on the temperature. As a result, the stability of the microwave photonic filter can be guaranteed when a temperature controller is used in the experiment. The corresponding gains of the EDFAs and the output optical power after each component are labelled in Fig. 3.12 (a). The EDFAs were used to compensate for the high insertion losses of the filters and a wideband BPF2 was used to remove the excess ASE noise. The measured optical spectra are shown in Fig. 3.12 (b) and (c). In Fig. 3.12 (b), the blue line shows the original OSSB signal launched into the filtering module. The red and green lines are the filter profiles for the notch filter and the integrated BPF respectively. Fig. 3.12 (c) depicts the output OSSB signal spectrum after the filtering module. The SFDR for the fronthaul link employing two cascaded integrated filters is measured to be $56.5\ \mathrm{dB \cdot Hz^{2/3}}$. Compared with optical filtering using Waveshaper, the SFDR degrades in the two cascaded filter solution. The reasons lie in larger insertion losses, slower edge roll-off of the integrated filters, and increased ASE noise results from more EDFAs in the link.

The calculated EVMs versus received optical power for transmitting 5-Gbps 4 QAM signal along the fronthaul link is presented in Fig. 3.14 as the black line. Also depicted in Fig. 3.14 is the EVM curve for the fronthaul link deployed by using the WS (green line), which could provide an almost ideal dual-passband filter profile. By comparing the black line with the green line, it can be concluded that the loss of the two integrated filters coupled with the ASE noise from the three EDFAs will degrade the link performance. Besides, the slow edge roll-off of the integrated BPF filter is not able to suppress the upper sideband optical carrier (as seen in Fig. 3.12 (c)). As a result, receiver sensitivity employing WS is more than 5 dB lower than that employing three cascaded filters at the FEC limit with 7% overhead.

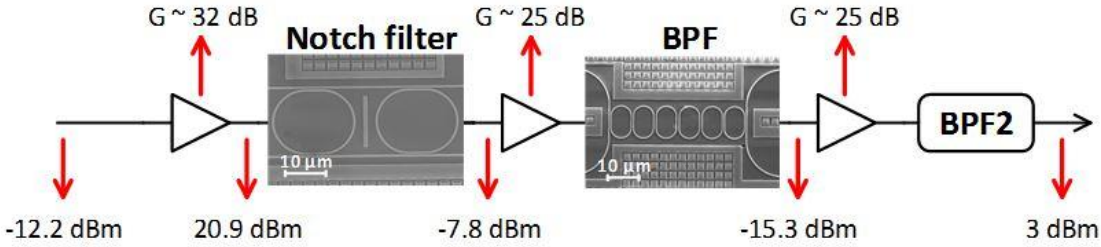

(a)

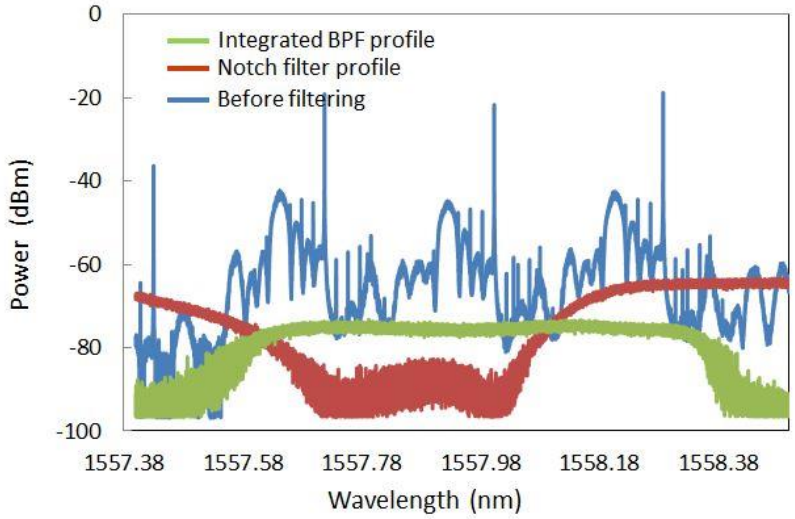

(b)

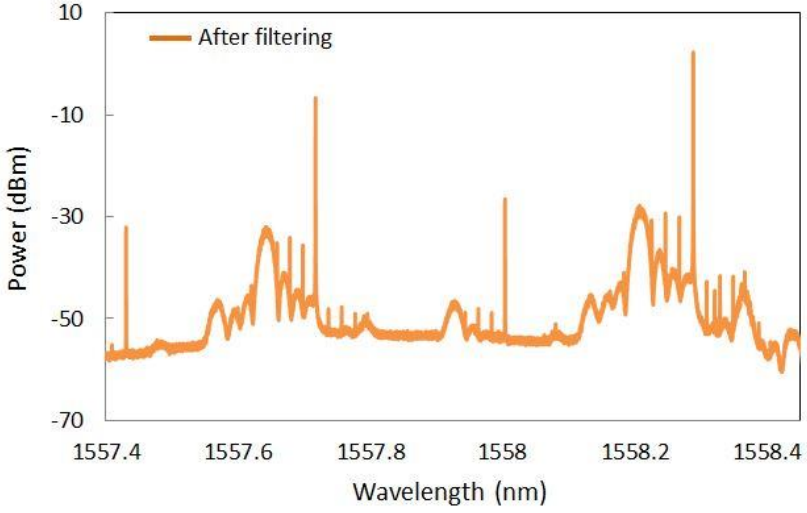

(c)

Fig. 3.12 (a) Optical filtering module employing two cascaded integrated filters followed by an amplifier for power compensation. Inset: top-view SEM images of the fabricated on-chip filters. (b) Optical spectrum of the OSSB signal before filtering (blue), the notch filter profile (red), and the integrated BPF profile (green). (c) Optical spectrum of the OSSB signal after optical filtering.

3.4.2.3 An Integrated Notch Filter Cascaded with a Commercial Available Ultra-Sharp Tunable Filter

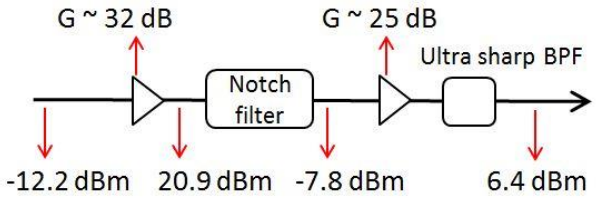

(a)

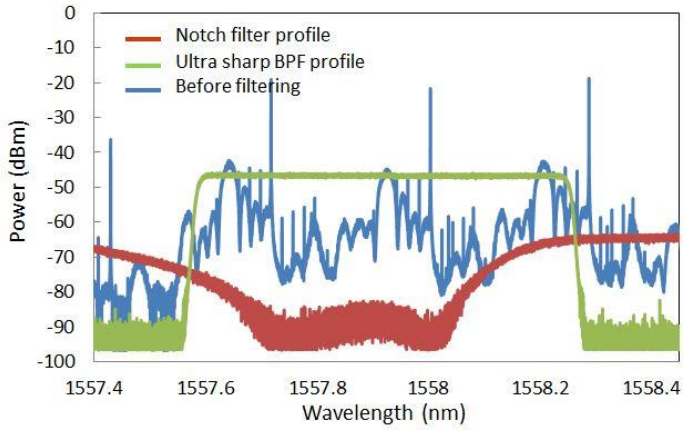

(b)

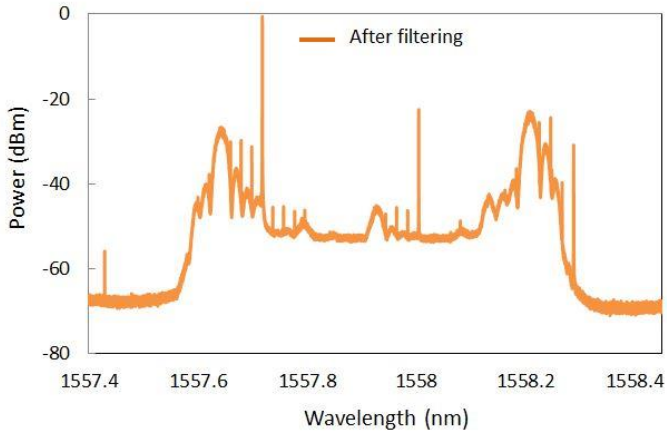

(c)

Fig. 3.13 (a) Optical filtering module employing one integrated notch filter cascaded with a commercial available ultra-sharp tunable filter. (b) Optical spectrum of the OSSB signal before filtering (blue), the notch filter profile (red), and the ultra-sharp BPF profile (green). (c) Optical spectrum of the OSSB signal after optical filtering.

In order to further confirm that the link performance degradation is caused by the large losses and slow roll-off of the integrated filters, we further investigate the filtering function with the notch filter followed by a commercially available ultra-sharp tunable filter (Alnair Labs BVF-300CL) as depicted in Fig. 3.13 (a). In this case, only two EDFAs were needed and the output optical power was 6.4 dBm. Shown in Fig. 3.13 (b) is the filter profile of the ultra-sharp BPF (green line) and the output signal spectrum is presented in Fig. 3.13 (c). The ultra-sharp BPF with a roll-off of 1500dB/nm is able to suppress the upper sideband optical carrier and the ASE noise is removed as well. It should be noted that the ASE noise level is high when we cascade three (resp. two) EDFAs in Fig. 3.12 (a) (resp. Fig. 3.13 (a)). The SFDR for this fronthaul configuration is measured to be 61.5 $dB \cdot Hz^{2/3}$, which is better than the SFDR of the fronthaul link employing two integrated filters. The corresponding EVM curve is shown in Fig. 3.14 as the red line. We can see that the smaller insertion loss of the commercial filter helps in reducing the number of EDFAs needed, which in turn reduces the ASE noise. Meanwhile, the sharp roll-off provides better ability to remove the out-of-band ASE noise. Hence, the 60.25-GHz fronthaul link can achieve similar receiver sensitivity as the one using Waveshaper as depicted in Fig. 3.14.

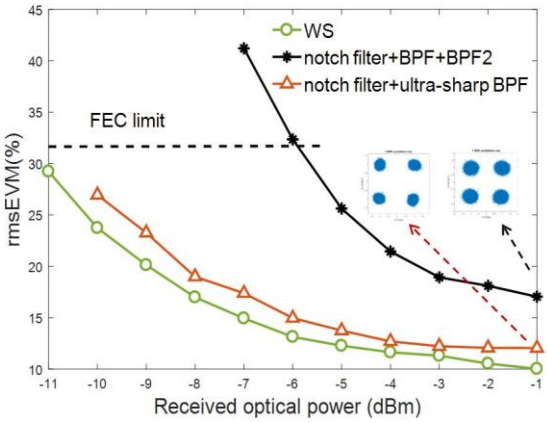

Fig. 3.14 EVM curves against received optical power

3.5 Summary

In this chapter, we proposed two analog RoF fronthaul options for the next generation mobile communication networks based on a variation of OSSB and DSB-SC modulation techniques.

Both schemes were achieved using two cascaded external modulation stages that relax the stringent requirements for high speed electrical components. The proposed fronthaul alternatives take advantages of the low-loss and cost-effective RoF links and the large available bandwidth in the 60-GHz frequency band, providing high-bandwidth and high data rate to cater for future mobile communications.

Firstly, the principle of operation of the proposed fronthaul schemes was analysed. Secondly, we experimentally carried out a systematic comparison of the system performance of the two fronthaul alternatives and quantified the impact of chromatic dispersion along different length fronthaul links. 4 QAM and 16 QAM 60.25-GHz mm-wave signals are transmitted over different lengths (3 km and 10 km) fibre fronthaul links for the two proposed transport schemes at various bit rate (2.5 Gbps, 5 Gbps and 8 Gbps). We have demonstrated that the modified OSSB scheme has a better receiver sensitivity compared with the modified DSB-SC scheme. Besides, RF fading caused by chromatic dispersion effects can be overcome using the modified OSSB scheme, making it a superior transport option for future broadband fronthaul networks.

Secondly, we utilised integrated microwave photonics filters in the BBU to provide a small size and low cost optical filtering function. A wavelength tunable notch filter and a bandpass filter (BPF) were cascaded. We tuned the stop band of the notch filter to the centre passband of the BPF to form a dual-passband filter profile with a frequency separation of around 60 GHz. The 60 GHz RoF fronthaul link employing two low cost integrated filters was demonstrated through experiment and achieved a receiver sensitivity of -5.8 dBm at the 7% overhead FEC limit transmitting 5-Gbps 4 QAM signals. The performance of the proposed system was also compared with the benchmark link employing WS as an optical filtering module. Experimental results showed that the system employing WS outperformed the system employing integrated filters due to the fact that the integrated filters have large insertion loss and slow roll-off. We also validated that the fronthaul link performance can be further improved with smaller insertion loss and steeper roll-off integrated filters through experimental demonstration.

Chapter 4 Analytical Modeling of Fronthaul Links

4.1 Introduction

Analog radio-over-fibre fronthaul links operating at millimetre-wave (mm-wave) frequency band have the potential to offer high-bandwidth and high data rate to cater for future 5G mobile communications. Analytical models of mm-wave RoF systems have been widely investigated in the past decades [58, 65, 140, 141] to characterise the system performance. However, there is a lack of thorough theoretical analysis and comparison of the analog RoF fronthaul link performance in the 60-GHz range employing different external modulation formats.

In Chapter 3, we have proposed and experimentally demonstrated two schemes to generate 60.25-GHz millimetre-wave signals based on a variation of optical single sideband (OSSB) and optical double sideband suppressed carrier (DSB-SC) modulation techniques. In this chapter, comprehensive time-domain analytical models for the two proposed analog fronthaul schemes are derived.

In the derived analytical models for the two fronthaul schemes, a small signal analysis is performed with regard to mm-wave signal modulation. The better receiver sensitivity of the modified OSSB scheme, which has inherently lower optical carrier-to-sideband ratio (OCSR) than the DSB-SC scheme, can be verified by the derived analytical models. In addition, the noise sources in the fronthaul systems are also analysed and included in the derived models to characterise the signal-to-noise ratio (SNR) performance.

Fibre chromatic dispersion is the phenomenon where a wave will have different group velocity at different frequencies. The impact of chromatic dispersion on the performance of analog mm-wave RoF systems has been widely investigated [142, 143]. In mm-wave RoF communication links, the chromatic dispersion will severely limit the transmission distance and data rate [64, 144], especially for transmitting radio signals with frequencies above the 20-GHz range. This is due to the dispersion-induced RF power fading that will degrade the received RF power after photodetection when using conventional DSB modulation format [64]. Several techniques have

been proposed to overcome the RF power fading, including the optical single-sideband with carrier (OSSB+C) modulation scheme [59], external filtering [145], and fibre nonlinearities [70]. Analytical models have been derived in order to characterise the influence of chromatic dispersion in analog RoF communication links.

In Chapter 3 we concluded that the dispersion effect had negligible effect on the proposed modified OSSB fronthaul scheme, while the modified DSB-SC scheme suffered from the RF power fading that will limit the transmission distance. In this chapter, the exact time domain model is derived with regard to the dispersion induced RF power fading in the modified DSB-SC fronthaul link. Besides, comparison of the RF power fading effect between the modified DSB-SC fronthaul scheme and the traditional single stage DSB modulation technique is made. The modified DSB-SC scheme is less sensitive to the dispersion induced RF power fading due to the utilisation of two cascaded stage of external modulation.

This chapter is organised as follows: in Section 4.2 and 4.3, the theoretical analysis and comprehensive time domain modelling of the modified DSB-SC and the modified OSSB fronthaul schemes are presented; in Section 4.4, system performance comparison and analysis are given including the OCSR analysis, the noise process, and simulation results for the proposed two fronthaul schemes; in Section 4.5, the chromatic dispersion effect in the modified DSB-SC scheme is derived and discussed.

4.2 Analytical Model of the Modified DSB-SC Fronthaul Link

The schematic diagram of the modified DSB-SC scheme is demonstrated in Fig. 4.1. L_n and G_n in the figure denote the insertion loss and gain of corresponding components. It should be noted that as a proof-of-concept demonstration, here we only consider the electrical back-to-back scenario without the antennas and wireless link as shown in the diagram. The impact of wireless link (path loss, shadowing effect, etc.) will be discussed and analysed in Chapter 6.

Single-mode laser source of angular frequency ω_c and optical field amplitude E_0 is modulated by a local oscillator signal with a mm-wave frequency of ω_{mm} (25.25 GHz) using a DE-MZM biased at minimum transmission point. The DE-MZM modulates the light intensity due to the linear electro-optic (Pockel) effect, resulting in a change in the optical waveguide refractive

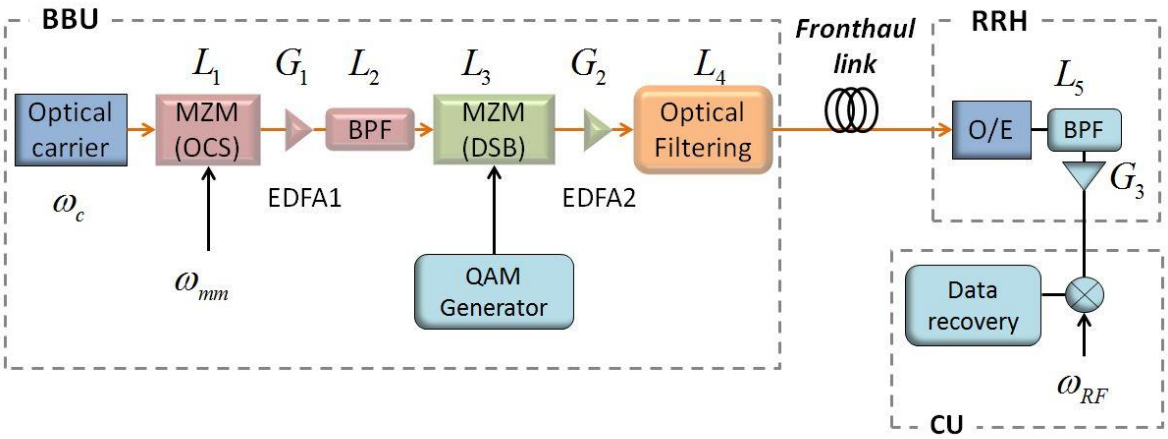

Fig. 4.1 Schematic diagram of analytical model for the modified DSB-SC fronthaul link

index which is proportional to the drive electric field. Eventually, a phase difference is electro-optically induced between two arms of the DE-MZM. As we have mentioned in Chapter 3, Section 3.3, only one electrode of the DE-MZM was driven by the LO signal, while the other electrode was terminated. As a result, the optical field at the output of the first MZM is given as [58, 146]:

$$\mathrm{E_{MZM1}} = \frac{\sqrt{L_1}}{2} E_0 e^{j\omega_c t}\left(e^{j\pi\frac{V_1(t)}{V_{\pi 1}}} + e^{j\pi\frac{V_2(t)}{V_{\pi 1}}}\right) \tag{1}$$

where $\mathrm{V_1}(t) = \mathrm{m_1}\cos(\omega_{mm}t + \phi_1) + \mathrm{V_{\pi 1}}$ and $\mathrm{V_2} = 0$ are local oscillator (LO) driving signals for two arms of DE-MZM. $\mathrm{m_1}$ is the amplitude of driving signal and ϕ_1 is the phase noise of LO signal. $\mathrm{V_{\pi 1}}$ denotes the switching voltage of the DE-MZM. Therefore, (1) is written as

$$\mathrm{E_{MZM1}} = \frac{\sqrt{L_1}}{2} E_0 e^{j\omega_c t}\left(1 - e^{\frac{jm_1\pi}{V_{\pi 1}}\cos(\omega_{mm}t+\phi_1)}\right) \tag{2}$$

According to Jacobi-Anger expansion $e^{iz\cos\theta} \equiv J_0(z) + 2\sum_{n=1}^{\infty} i^n J_n(z)\cos(n\theta)$, we can get

$$\begin{aligned} e^{\frac{jm_1\pi}{V_{\pi 1}}\cos(\omega_{mm}t+\phi_1)} &\approx J_0\left(\frac{m_1\pi}{V_{\pi 1}}\right) + 2jJ_1\left(\frac{m_1\pi}{V_{\pi 1}}\right)\cos(\omega_{mm}t+\phi_1) \\ &= J_0(a) + jJ_1(a)\left(e^{j\omega_{mm}t+j\phi_1} + e^{-j\omega_{mm}t-j\phi_1}\right) \end{aligned} \tag{3}$$

where J_n is the n^{th}-order Bessel function of the first kind. The modulation index is defined as $a = m_1\pi/V_{\pi 1}$. Noted that higher order harmonics are ignored in (3) for simplicity [147]. Now (2) can be expanded as follows:

$$E_{MZM1} = \frac{E_0\sqrt{L_1}}{2}\left[\left(1 - J_0(a)\right)e^{j\omega_c t} - jJ_1(a)e^{j(\omega_c+\omega_{mm})t+j\phi_1} - jJ_1(a)e^{j(\omega_c-\omega_{mm})t-j\phi_1}\right] \quad (4)$$

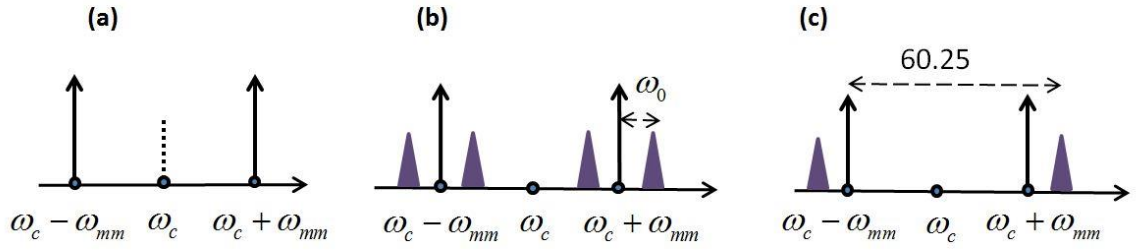

Fig. 4.2 Optical frequency components (a) after the first stage modulation, (b) second stage modulation, and (c) after optical filtering module

As illustrated in Fig. 4.2 (a), three frequency components with frequency of ω_c, $\omega_c + \omega_{mm}$, and $\omega_c - \omega_{mm}$ exist at the output of the first DE-MZM. Meanwhile, $1 - J_0(a)$ is relatively smaller than $J_1(a)$ considering small signal modulation, the centre optical carrier with frequency of ω_c is suppressed in order to generate OCS signal with frequency separation of $2\omega_{mm}$ after the first modulation stage. EDFA1 is used to compensate for the insertion loss of DE-MZM and the bandpass filter (BPF) removes the unwanted optical components and out-of-band amplified spontaneous emission (ASE) noise.

In the second modulation stage, the QAM signal is first up-converted to an IF frequency ω_0 (9.75 GHz) using an IQ mixer. The up-converted IF QAM signal is expressed as:

$$s(t) = I(t)\cos\omega_0 t - Q(t)\sin\omega_0 t \quad (5)$$

where $I(t)$ and $Q(t)$ are the in-phase and quadrature-phase components of the QAM signal. The second balanced single electrode MZM is biased at quadrature point to generate DSB modulated mm-wave signals [148]. The optical field at the output of the MZM is written as:

$$E_{MZM2} = \frac{E_{MZM1}\sqrt{L_2 L_3 G_1}}{2}\left(e^{j\pi\frac{s(t)+V_{\pi 2}/2}{V_{\pi 2}}} + e^{j\pi\frac{s(t)+V_{\pi 2}/2}{V_{\pi 2}}}\right)$$
$$= E_{MZM1}\sqrt{L_2 L_3 G_1}\cdot e^{j\pi\frac{s(t)+V_{\pi 2}/2}{V_{\pi 2}}} \tag{6}$$

$V_{\pi 2}$ denotes the switching voltage of the single electrode MZM. For small-signal modulation we use $e^x \approx 1 + x$ for simplicity. Then (6) can be simplified to

$$\begin{aligned} E_{MZM2} = {} & \frac{E_0\sqrt{L_1 L_2 L_3 G_1}}{2}\times \\ & \{j(1-J_0(a))e^{j\omega_c t} + jJ_1(a)(e^{j\phi_1}e^{j(\omega_c+\omega_{mm})t} + e^{-j\phi_1}e^{j(\omega_c-\omega_{mm})t}) \\ & -\frac{\pi}{2V_{\pi 2}}(I(t)+jQ(t))[(1-J_0(a))e^{j(\omega_c+\omega_0)t} \\ & -jJ_1(a)e^{j\phi_1}e^{j(\omega_c+\omega_{mm}+\omega_0)t} - jJ_1(a)e^{-j\phi_1}e^{j(\omega_c-\omega_{mm}+\omega_0)t}] \\ & -\frac{\pi}{2V_{\pi 2}}(I(t)-jQ(t))[(1-J_0(a))e^{j(\omega_c-\omega_0)t} \\ & -jJ_1(a)e^{j\phi_1}e^{j(\omega_c+\omega_{mm}-\omega_0)t} - jJ_1(a)e^{-j\phi_1}e^{j(\omega_c-\omega_{mm}-\omega_0)t}]\} \end{aligned} \tag{7}$$

The terms with frequency of $\omega_c + \omega_{mm}$, $\omega_c - \omega_{mm}$, $\omega_c + \omega_{mm} + \omega_0$, and $\omega_c - \omega_{mm} - \omega_0$ are the desired mm-wave frequency carriers and QAM signals as shown in Fig. 4.2 (b). While the terms with frequency of ω_c, $\omega_c + \omega_0$, and $\omega_c - \omega_0$ are the residual centre optical carrier and signals originating from the finite optical carrier suppression ratio of the OCS modulation. The terms with frequency of $\omega_c - \omega_{mm} + \omega_0$ and $\omega_c + \omega_{mm} - \omega_0$ correspond to the undesired signal sidebands as shown in Fig. 4.2 (b). These central optical carrier and unwanted signal components will be removed after the optical filtering module as shown in Fig. 4.2 (c). The corresponding electrical field after filtering is represented as

$$\begin{aligned} E_{OF} = {} & \frac{E_0\sqrt{L_1 L_2 L_3 L_4 G_1 G_2}}{2}\{jJ_1(a)(e^{j\phi_1}e^{j(\omega_c+\omega_{mm})t} + e^{-j\phi_1}e^{j(\omega_c-\omega_{mm})t}) \\ & + \frac{j\pi J_1(a)}{2V_{\pi 2}}[(I(t)+jQ(t))\cdot e^{j\phi_1}e^{j(\omega_c+\omega_{mm}+\omega_0)t} \\ & +(I(t)-jQ(t))\cdot e^{-j\phi_1}e^{j(\omega_c-\omega_{mm}-\omega_0)t}]\} \end{aligned} \tag{8}$$

The signal is received at the RRH after transmission along the fronthaul link. Here we consider a back-to-back case (0-km fibre transmission) where the fibre chromatic dispersion effect is not considered. The impact of chromatic dispersion effect in the proposed fronthaul schemes will be investigated in Section 4.5. The detected photocurrent is thus given by

$$\begin{aligned} i_p(t) &= \Re(E_{OF} \cdot E_{OF}^{*}) \\ &= \frac{\Re E_0^2 L_1 L_2 L_3 L_4 G_1 G_2 J_1^2(a)}{4} \times \\ &\left\{ \begin{array}{l} 2 + \frac{\pi^2}{2V_{\pi 2}^2}(I^2 + Q^2) + e^{j2\omega_{mm}t + j2\phi_1} + e^{-j2\omega_{mm}t - j2\phi_1} \\ + \frac{\pi}{V_{\pi 2}}[(I + jQ)e^{j\omega_0 t} + (I - jQ)e^{-j\omega_0 t}] \\ + \frac{\pi^2}{4V_{\pi 2}^2}[(I + jQ)^2 e^{j2\phi_1} e^{j(2\omega_{mm} + 2\omega_0)t} + (I - jQ)^2 e^{-j2\phi_1} e^{-j(2\omega_{mm} + 2\omega_0)t}] \\ + \frac{\pi}{V_{\pi 2}}[(I + jQ)e^{j2\phi_1} e^{j(2\omega_{mm} + \omega_0)t} + (I - jQ)e^{-j2\phi_1} e^{-j(2\omega_{mm} + \omega_0)t}] \end{array} \right\} \end{aligned} \quad (9)$$

Here $\Re$ denotes the responsivity of PD. The last two terms in (9) show the desired mm-wave RF signal at frequency $\omega_0 + 2\omega_{mm}$ (60.25 GHz). These terms can be easily separated from other frequency components by using a suitable BPF. The RF signal is further amplified before sending to the customer unit. The RF signal can therefore be written as

$$RF_1 = \left[\begin{array}{l} \frac{\Re E_0^2 L_1 L_2 L_3 L_4 L_5 G_1 G_2 G_3 J_1^2(a)\pi}{2V_{\pi 2}} \times \\ [Q(t)\sin(2\omega_{mm}t + \omega_0 t + 2\phi_1) - I(t)\cos(2\omega_{mm}t + \omega_0 t + 2\phi_1)] \end{array} \right] \quad (10)$$

In the customer unit, the RF signal will be down-converted to IF frequency using a mixer and a LO signal that can be expressed as $V_{LO}(t) = m_2\cos(\omega_{RF} + \phi_2)$. ω_{RF} is set to be 58 GHz so that the down-converted frequency is ω_{IF} (2.25 GHz). The down-converted QAM signal can be written as

$$RF_2 = RF_1 \cdot V_{LO}(t) = A \cdot [Q\sin(\omega_{IF}t + 2\phi_1 - \phi_2) - I\cos(\omega_{IF}t + 2\phi_1 - \phi_2)] \quad (11)$$

Here, we define $A = \Re E_0^2 L_1 L_2 L_3 L_4 L_5 G_1 G_2 G_3 J_1^2(a)\pi m_2 / 4V_{\pi 2}$. The QAM signal demodulation process will produce the recovered in-phase and quadrature phase components

$$\begin{cases} X = RF_2 \cos(\omega_{IF} t + \phi_3) = (A/2)[I\cos(\phi) - Q\sin(\phi)] \\ Y = RF_2 \sin(\omega_{IF} t + \phi_3) = (A/2)[Q\cos(\phi) + I\sin(\phi)] \\ \phi = 2\phi_1 - \phi_2 - \phi_3 \end{cases} \quad (12)$$

Finally, by using phase estimation in MATLAB post processing ($\phi_3 = 2\phi_1 - \phi_2$), (12) is simplified as

$$X = A \cdot I(t)/2 \quad , \quad Y = A \cdot Q(t)/2 \quad (13)$$

4.3 Analytical Model of the Modified OSSB Fronthaul Link

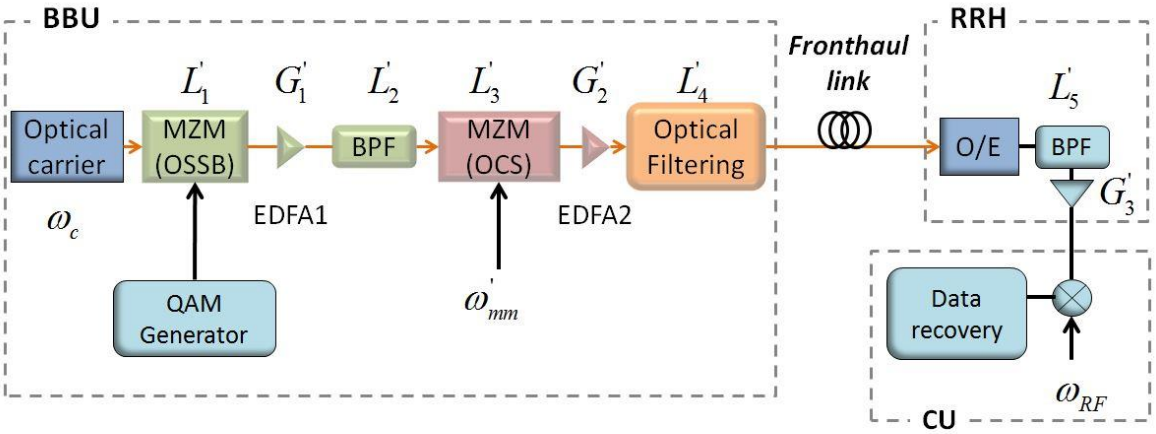

Fig. 4.3 Schematic diagram of analytical model for the modified OSSB fronthaul link

Shown in Fig. 4.3 is the schematic diagram of the modified OSSB scheme. The main difference between DSB-SC scheme and OSSB scheme lies in the BBU, where for the latter scheme OSSB data modulation is followed by OCS modulation to generated desired mm-wave frequency signal. The first DE-MZM is driven by two signals with 90˚ phase shift and the biased at quadrature point. The two driving signals are given by

$$V_1'(t) = s(t) \quad , \quad V_2'(t) = s(t + \pi/2) + V_{\pi 1}/2 \quad (14)$$

Hence, for the OSSB scheme, we substitute (14) into (1) and assume $e^x \approx 1 + x$ for simplicity, the optical fields after OSSB modulation can be written as follows

$$E_{MZM1}^{'} = \frac{E_0^{'}\sqrt{L_1^{'}}}{2}((1+j)e^{j\omega_c t} + \frac{\pi}{V_{\pi 1}}(Q(t)+jI(t))e^{j(\omega_c-\omega_0)t}) \tag{15}$$

The resulted optical fields contain two optical frequency components as shown in Fig. 4.4 (a), corresponding to an OSSB signal with a frequency of $\omega_c - \omega_0$ and an optical carrier with a frequency of ω_c.

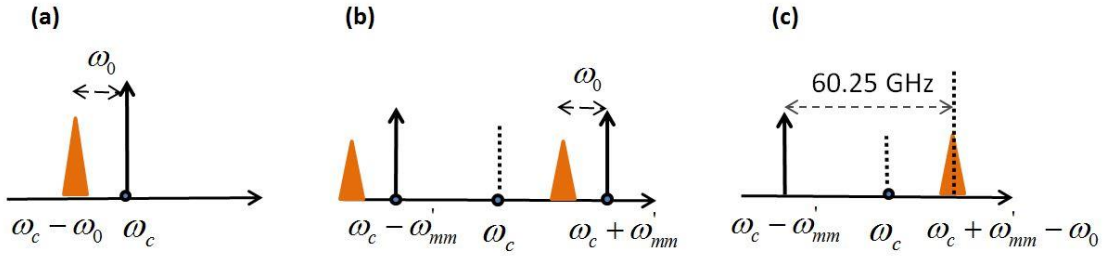

Fig. 4.4 Schematic diagram of analytical model for the modified OSSB fronthaul link

Similarly, to generate OCS modulation the second stage DE-MZM is biased at minimum transmission point. Only one electrode of the second stage DE-MZM is driven by a signal with frequency of ω_{mm}' (35 GHz), while the other electrode was terminated. The driving signal is expressed as

$$V_3^{'}(t) = m_1^{'}\cos(\omega_{mm}^{'}t + \phi_1^{'}) + V_{\pi 2}^{'} \quad , \quad V_4^{'}(t) = 0 \tag{16}$$

where m_1' is the amplitude of driving signal and ϕ_1' is the phase noise of LO signal. $V_{\pi 2}'$ denotes the switching voltage of the DE-MZM. The corresponding electrical field at the output of the second DE-MZM is expressed as follows:

$$\begin{aligned} E_{MZM2}^{'} &= \frac{E_{MZM1}^{'}\sqrt{G_1^{'}L_2^{'}L_3^{'}}}{2}(e^{j\pi\frac{V_3^{'}(t)}{V_{\pi 2}^{'}}} + e^{j\pi\frac{V_4^{'}(t)}{V_{\pi 2}^{'}}}) \\ &= \frac{E_{MZM1}^{'}\sqrt{G_1^{'}L_2^{'}L_3^{'}}}{2}(1+e^{j\pi\frac{m_1^{'}\cos(\omega_{mm}^{'}t+\phi_1^{'})+V_{\pi 2}^{'}}{V_{\pi 2}^{'}}}) \end{aligned} \tag{17}$$

By using the Jacobi-Anger expansion and ignoring the higher order harmonics, (17) can be expanded and simplified as follows:

$$
\begin{aligned}
E_{MZM2}^{'} = \frac{E_0^{'}\sqrt{G_1^{'}L_1^{'}L_2^{'}L_3^{'}}}{4}\{&(1+j)(1-J_0(b))e^{j\omega_c t} \\
&+(1-j)J_1(b)[e^{j\phi_1^{'}}e^{j(\omega_c+\omega_{mm}^{'})t}+e^{-j\phi_1^{'}}e^{j(\omega_c-\omega_{mm}^{'})t}] \\
&+(\pi/V_{\pi 1})(jI(t)+Q(t))[(1-J_0(b))e^{j(\omega_c-\omega_0)t} \\
&-jJ_1(b)(e^{j\phi_1^{'}}e^{j(\omega_c+\omega_{mm}^{'}-\omega_0)t}+e^{-j\phi_1^{'}}e^{j(\omega_c-\omega_{mm}^{'}-\omega_0)t})]\}
\end{aligned}
\tag{18}
$$

Here, $\mathrm{b} = m_1' \pi/V_{\pi 2}'$ is defined as the modulation index. In (18), the terms with frequency of $\omega_c - \omega_{mm}'$ and $\omega_c + \omega_{mm}' - \omega_0$ are the desired optical carrier and RF signal as shown in Fig. 4.4 (b). Only these two terms will be of interest after the optical filtering by the Waveshaper. The corresponding optical field after filtering is illustrated in Fig. 4.4 (c) and is represented as

$$
\begin{aligned}
E_{OF}^{'} = \frac{E_0^{'}\sqrt{G_1^{'}L_1^{'}L_2^{'}L_3^{'}}}{4}\times\{&(1-j)J_1(b)e^{-j\phi_1^{'}}e^{j(\omega_c-\omega_{mm}^{'})t} \\
&+(I(t)-jQ(t))\frac{\pi J_1(b)}{V_{\pi 1}}e^{j\phi_1^{'}}e^{j(\omega_c+\omega_{mm}^{'}-\omega_0)t}\}
\end{aligned}
\tag{19}
$$

Upon photo-detection in the RRH, the photocurrent is given by

$$
\begin{aligned}
i_p^{'}(t) &= \Re(E_{OF}^{'}\cdot E_{OF}^{'*}) \\
&= \frac{\Re E_0^{'2}L_1^{'}L_2^{'}L_3^{'}L_4^{'}G_1^{'}G_2^{'}}{16}\{2J_1^2(b)+\frac{\pi^2}{V_{\pi 1}^2}(I^2(t)+Q^2(t))J_1^2(b) \\
&+J_1^2(b)\frac{2\pi}{V_{\pi 1}}[(I(t)+Q(t))\cos(2\omega_{mm}^{'}t-\omega_0 t+2\phi_1^{'}) \\
&+(Q(t)-I(t))\sin(2\omega_{mm}^{'}t-\omega_0 t+2\phi_1^{'})]\}
\end{aligned}
\tag{20}
$$

The analytical expression after bandpass filtering and amplification can be written as

$$
\begin{aligned}
RF_1^{'} = (\Re E_0^{'2}L_1^{'}L_2^{'}L_3^{'}L_4^{'}L_5^{'}G_1^{'}G_2^{'}G_3^{'}J_1^2(b)\pi/8V_{\pi 1})\times \\
\begin{bmatrix}(I(t)+Q(t))\cos(2\omega_{mm}^{'}t-\omega_0 t+2\phi_1^{'}) \\ +(Q(t)-I(t))\sin(2\omega_{mm}^{'}t-\omega_0 t+2\phi_1^{'})\end{bmatrix}
\end{aligned}
\tag{21}
$$

Equation (21) shows the desired mm-wave frequency signal at $2\omega_{mm}' - \omega_0$ (60.25 GHz). Finally in the CU, a same LO signal ($\omega_{\mathrm{RF}} = 58\ GHz$) as in the DSB-SC scheme is used to

down-convert the mm-wave signal. Therefore, the down-converted signal can now be expressed as

$$\begin{aligned} RF_2^{'} &= RF_1^{'} \cdot V_{LO}(t) = RF_1^{'} \cdot m_2 \cos(\omega_{RF} + \phi_2) \\ &= \begin{bmatrix} B[(I(t)+Q(t))\cos(\omega_{IF}t + 2\phi_1^{'} - \phi_2^{'}) \\ +(Q(t)-I(t))\sin(\omega_{IF}t + 2\phi_1^{'} - \phi_2^{'})] \end{bmatrix} \end{aligned} \tag{22}$$

where $B = \Re E_0'^2 L_1' L_2' L_3' L_4' L_5' G_1' G_2' G_3' J_1^2(b)\pi m_2 / 16 V_{\pi 1}$. Utilizing the same QAM demodulation process as in the DSB-SC scheme, we have

$$\begin{cases} X^{'} = RF_2^{'}\cos(\omega_{IF}t + \phi_3^{'}) = \dfrac{B}{2}[I\cdot(\cos\theta - \sin\theta) + Q\cdot(\cos\theta + \sin\theta)] \\ Y^{'} = RF_2^{'}\sin(\omega_{IF}t + \phi_3^{'}) = \dfrac{B}{2}[-I\cdot(\sin\theta + \cos\theta) + Q\cdot(\cos\theta - \sin\theta)] \\ \theta = 2\phi_1^{'} - \phi_2^{'} - \phi_3^{'} \end{cases} \tag{23}$$

In MATLAB post processing, using the phase estimation to acquire $\sin\Theta + \cos\Theta = 0$, we will get the final recovered baseband in-phase and quadrature phase components as

$$\mathrm{X}' = Bcos\Theta \bullet I(t),\ \mathrm{Y}' = Bcos\Theta \bullet Q(t) \tag{24}$$

In the analytical model, QAM signal distortion induced by higher order harmonics are neglected to simplify the mathematic model. However, this model gives a thorough demonstration of the signal propagation process through the entire analog fronthaul link, considering the electrical-to-optical conversion (E/O) and optical-to-electrical conversion (O/E) energy conversion, signal amplification and insertion losses.

4.4 System Performance Comparison and Analysis

4.4.1 OCSR Analysis on Two Analog RoF Fronthaul Links

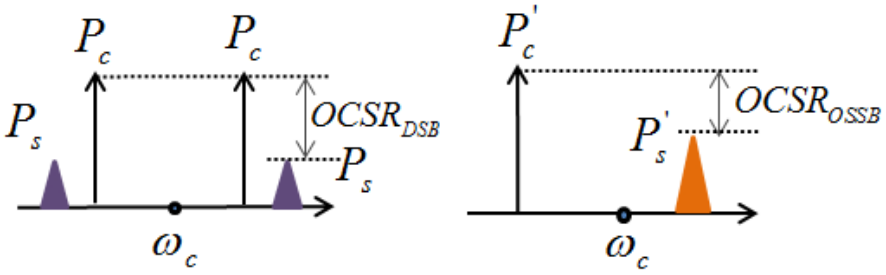

Fig. 4.5 OCSR definition for (a) the modified DSB-SC scheme and (b) the modified OSSB scheme

In order to optimise the performance of the RoF fronthaul links, the optical carrier-to-sideband power ratio (OCSR) can be altered during the experiments. There have been investigations on the performance improvements by tuning the OCSR in RoF links using OSSB modulation techniques [58, 140, 149]. In this section, a thorough analysis and comparison of the OCSR in RoF fronthaul links based on our proposed DSB-SC and OSSB schemes are demonstrated. The impact of OCSR on the link performance is also evaluated.

As depicted in Fig. 4.5 is the definition of the OCSR in the modified DSB-SC scheme and the modified OSSB scheme. According to (7) and (18), the OCSR of the modified DSB-SC and OSSB scheme can be mathematically expressed as

$$OCSR_{DSB} = \frac{P_c}{P_s} = \frac{4}{a_1^2} \quad , \quad OCSR_{OSSB} = \frac{P_c'}{P_s'} = \frac{2}{b_1^2} \tag{25}$$

where $a_1 = \pi\sqrt{I^2(t) + Q^2(t)}/V_{\pi 2}$ and $b_1 = \pi\sqrt{I^2(t) + Q^2(t)}/V_{\pi 1}$ are the modulation indexes for the QAM data modulation stage in the two schemes respectively.

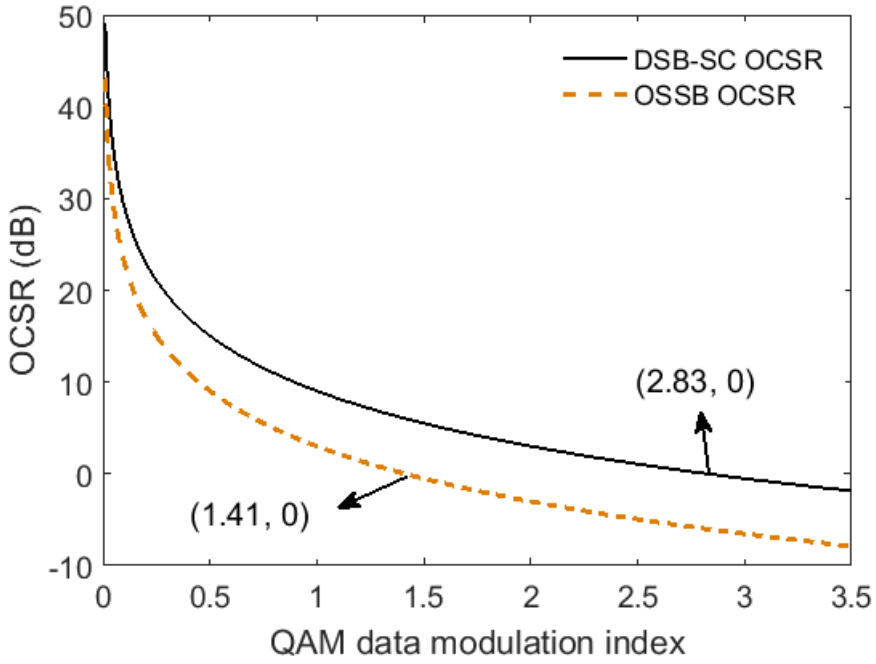

Fig. 4.6 OCSR as a function of modulation index for (a) the modified DSB-SC scheme and (b) the modified OSSB scheme

In Fig. 4.6 we show the OCSR against the modulation index for the two fronthaul schemes. In order to obtain the optimum link performance at $\mathrm{OCSR} = 0\mathrm{dB}$ [58], a much higher modulation index is needed in the modified DSB-SC scheme ($a_1 = 2.83$) than in the modified OSSB scheme ($b_1 = 1.41$). Due to the low modulation efficiency at mm-wave frequencies, the mm-wave signal is typically weakly modulated onto optical carriers. In addition, the modulation efficiency is also limited by the nonlinear effects of the optical modulators. Hence, the modulation index for the two schemes is kept small in the experiments. In order to achieve a fair comparison between two schemes, the same modulation index is utilised in the experiments. In this regard, the OSSB scheme has the ability to achieve a lower receiver sensitivity.

Now we will investigate the optimum OCSR value in the fronthaul system. Assume that all the unwanted frequency components are suppressed by the Waveshaper and can be neglected. Therefore, the total received optical power at the photodetector in back-to-back fronthaul links can be expressed as

$$P_{PD} = 2(P_c + P_s) \quad , \quad P_{PD}^{'} = P_c^{'} + P_s^{'} \tag{26}$$

here P_{PD} and P'_{PD} are the optical power received by PD in the DSB-SC and OSSB scheme, respectively. P_c, P_s, P'_c, and P'_s are the corresponding optical power of optical carriers and signal sidebands in the two schemes, respectively. According to the definition of OCSR, we have

$$OCSR_{DSB} = P_c / P_s \quad , \quad OCSR_{OSSB} = P_c^{'} / P_s^{'} \tag{27}$$

Combining equations (26) and (27), the RF signal power at frequency 60.25 GHz can be written as

$$\begin{aligned} RF_{DSB} &= 2\Re P_c P_s = \Re^2 P_{PD}^2 \frac{OCSR_{DSB}}{2(1+OCSR_{DSB})^2} \\ RF_{OSSB} &= \Re P_c^{'} P_s^{'} = \Re^2 P_{PD}^{'\,2} \frac{OCSR_{OSSB}}{(1+OCSR_{OSSB})^2} \end{aligned} \tag{28}$$

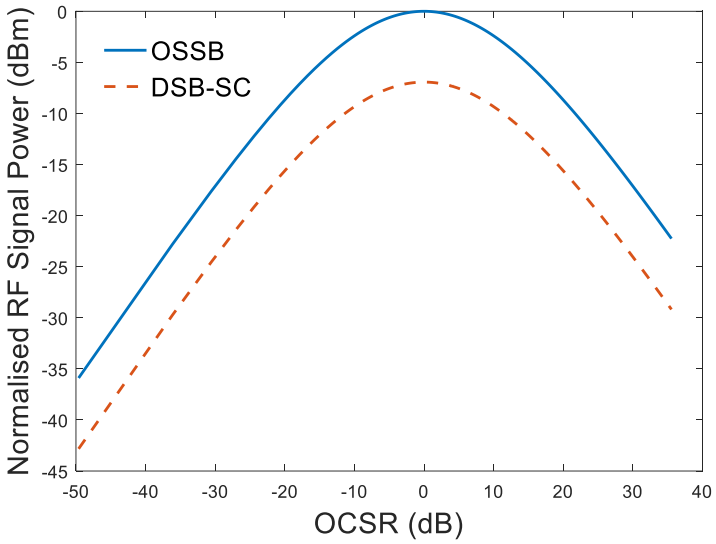

Fig. 4.7 Normalised RF signal power for (a) the modified DSB-SC scheme and (b) the modified OSSB scheme

For a certain received optical power, the relationship between the normalised RF signal power and OCSR for DSB-SC and OSSB scheme is shown in Fig. 4.7. In each scheme, the maximum RF power is obtained at OCSR = 0 dB, which is the optimum value for both cases. In the experiment, we observe an OCSR of 31.72 dB for DSB-SC scheme and 25.2 dB for OSSB scheme. As can be seen in Fig. 4.7, the RF signal power in DSB-SC scheme is smaller than in

OSSB scheme allowing for the much larger OCSR in DSB-SC scheme, leading to link performance degradation as mentioned in Chapter 3. The flexibility of having a filter with tunable profile can further improve the OCSR of the proposed systems and thus improve the received RF signal power.

4.4.2 Noise Process in Fronthaul Links

The noise process in the RoF fronthaul links is of great interest as the system performance is limited by the noise. In this section, the origins of noise in various electrical and optical devices in the analog fronthaul systems are explained and summarised. Besides, the mathematical expression of the total noise power of our proposed system is derived to characterise the system performance.

There are different noise sources within an optical transmission system [150]. The noise originated from the optical transmitter includes:

- *Relative intensity noise (RIN)*, which is caused by the instability in the laser output power level. It is generated from cavity vibration, fluctuations in the laser gain medium or from the intensity noise transferred from a pump source.
- *Laser phase noise,* caused by the fluctuations of the optical phase of the laser output.
- *Mode partition noise*, which is only considered in multimode lasers. The phase jitter generated by the variation of group velocity will result in mode partition noise. This group velocity change is created by mode hopping which causes random wavelength changes in the optical source.

The noise resulted from the optical fibre includes:

- *Modal noise,* generated in multimode fibre due to the random excitation of transversal modes and the power exchange among them. As we are using single-mode fiber (SMF) in the fronthaul networks, the modal noise will not be considered.

Optical connectors and splices are responsible for reflection-induced noise:

- *Reflection-induced noise* is often treated together with the laser intensity noise due to their same nature. It is originated from the back-reflected optical signal due to refractive index changes at connectors and optical splices.

The noise generated in optical amplifier include spontaneous emission noise and this noise will be amplified along the fibre transmission link which results in the amplified spontaneous emission (ASE) noise.

- *Spontaneous emission noise* is generated through the spontaneous emission process and is not correlated with the optical signal. It has a flat frequency spectrum and the spectral density can be expressed as

$$S_{sp}(v) = (G-1) \cdot NF_o hv/2 \tag{29}$$

where G and NF_0 are the gain and noise figure of the optical amplifier, $h = 6.63 \cdot 10^{-34} J/Hz$ is the Planck's constant, and υ is the frequency. When considering the contributions of two fundamental polarisation modes, the spontaneous emission noise power can be written as

$$P_{sp}(v) = 2\left|E_{sp}\right|^2 = 2S_{sp}(v)B_{op} = (G-1) \cdot NF_o hvB_{op} \tag{30}$$

where B_{OP} is the effective bandwidth which is determined by the bandwidth of optical amplifier.

- *Amplified spontaneous emission (ASE) noise* is the noise generated when cascading optical amplifiers along the transmission chain. The spontaneous noise will be amplified in the following amplification stage, thus resulted in the ASE noise. It should be noted that spontaneous noise will also happens in each of the amplification stage. As a result, the SNR is degraded during the transmission link.

Finally, the noise sources originated from the photodiode during optoelectronic conversion comprise thermal noise, quantum shot noise, dark current noise and electrical noise converted from the ASE noise. Since there is a beating process between the ASE noise and the signal electric fields, the beat noise components should also be considered during photo-detection. The beat noise components include signal-spontaneous beat noise and spontaneous-

spontaneous beat noise. The overall noise variance of the photocurrent generated at the output of photodiode can be written as

$$\left\langle i^2 \right\rangle_{PD} = \left\langle i^2 \right\rangle_{the} + \left\langle i^2 \right\rangle_{shot} + \left\langle i^2 \right\rangle_{sig-sp} + \left\langle i^2 \right\rangle_{sp-sp} \tag{31}$$

- *Thermal noise* is represented as the first term on the right side of (31). It arises from the random fluctuations of electron motion when temperature is above absolute zero. Specifically, the thermal noise in photodiodes is generated due to the random thermal motion of electrons in the load resistor that is used to convert the photocurrent to voltage. The thermal noise power can be represented as

$$\left\langle i^2 \right\rangle_{the} = \frac{4k\Theta\Delta f}{R_L} \tag{32}$$

  where k is the Boltzmann's constant, R_L is the load resistance, Θ is the absolute temperature in Kelvins, and Δf is the effective bandwidth of the receiver.

- *Quantum shot noise* is originated from the random distribution of electrons generated during the photodetection process. The quantum shot noise power is presented as

$$\left\langle i^2 \right\rangle_{shot} = 2qI\Delta f \tag{33}$$

  here $q = 1.6 \cdot 10^{-19}\ Coulombs$ is the electron charge, and I is the mean intensity of the photocurrent. For avalanche photodiodes (APD), the avalanche amplification process will increase the total quantum noise. The APD induced noise is characterised using avalanche shot noise which is out of the scope of this work and will not be discussed here.

- *Dark current noise* is generated in the p-n junction of a photodiode even if no light presents at the input. Generally, dark current noise is smaller compared with other noise sources and is thus sometimes neglected when calculating the SNR of an optical communication system.

- *Signal-Spontaneous beat noise* is caused by the beating process of the ASE noise and signal electric fields when converting the optical fields into electric fields. The variance of the fluctuating current caused by signal-spontaneous noise is calculated using

$$\left\langle i^2 \right\rangle_{sig-sp} = 4\Re^2 G_0 P_{in} S_{sp} \Delta f = S_{sig-sp} \Delta f \tag{34}$$

  In (34), G_0 is the gain of optical amplifier, $\Re$ is the responsivity of photodiodes, S_{sp} is the spectral density of spontaneous noise expressed as (29), P_{in} is the input optical power into the receiver.

- Spontaneous-spontaneous beat noise is caused by the beating process of the ASE field with itself and can be given by

$$\left\langle i^2 \right\rangle_{sp-sp} = 4\Re^2 S_{sp}^2 \Delta f (B_{ASE} - \Delta f / 2) \tag{35}$$

  where B_{ASE} is the bandwidth of optical filter. Noted that Δf represents the electrical filter bandwidth of the receiver in (34) and (35).

Apart from these noise sources generated in the optical transmission links, there is also noise originated from the electrical components (such as mixers, electrical amplifiers, etc.) deployed after the photodiode in the fronthaul links [151]. The main contributor to the noise from receiver electronics is the thermal noise, or the so-called Johnson noise, expressed using equation (32). The thermal noise caused by the load resister in the pre-amplifier in the photodiode will be increased by the amplifier followed in the receiver electronics. The resulted thermal noise power after passing through the amplifier with noise figure of NF_e can be written as

$$\left\langle i^2 \right\rangle_{the} = \frac{4k\Theta\Delta f \cdot NF_e}{R_L} \tag{36}$$

The noise processes within the proposed fronthaul transmission links mainly include noise originated from the cascades of optical amplifiers (EDFAs), the optoelectronic device (PD), and the electrical components in the RRH and CU. The intensity noise from the laser diode and

measuring equipment, such as the oscilloscope, is typically small compared to the other noise sources and can be ignored without impacting the overall performance.

The two EDFAs employed in the fronthaul link provide optical gain to compensate for the signal power losses, but they also induce additional noise that will degrade the quality of received analog signals. Each stage of EDFA adds broadband spontaneous emission noise to the signal as well as amplifies all the noise sources originated from the previous devices [152]. Apart from the EDFAs, the noise induced by passive devices along the fronthaul link is also considered. Since the noise power at the output of the passive device when terminating the input is always kTB, the noise factor of a passive device is given by

$$F = \frac{SNR_{in}}{SNR_{out}} = \frac{S^2/kTB}{GS^2/kTB} = \frac{1}{G} \tag{37}$$

As we can see in (37), the noise factor of a passive component is equal to the insertion loss. In order to derive the effective noise factor of the entire optical link, Friis' Formula is employed to calculate the noise factor of the cascaded stages:

$$F = F_1 + \frac{F_2 - 1}{G_1} + \frac{F_3 - 1}{G_1 G_2} + \cdots + \frac{F_N - 1}{G_1 \cdots G_{N-1}} \tag{38}$$

here F_i and G_i are the noise factor and gain of the i-th device. Expressing noise factor in dB, we can get the noise figure of cascaded stages: $NF = 10\log|F|$. The effective gain is the multiplicative gain value of all the cascaded components.

The receiver noise processes include shot noise, thermal noise, spontaneous-to-spontaneous beat noise and the dominant signal-to-spontaneous noise. As for the noise induced by the RF electronics in RRH and CU, we lump the noise sources into a thermal noise model as σ_{Rx}^2.

As a result, the total noise power for the entire fronthaul system, including receiver noise at the photodiode and noise induced by the RF electronics in the RRH and CU, is represented as

$$\begin{aligned} \sigma^2 &= \langle i^2 \rangle_{PD} + G_e NF_e \sigma_{Rx}^2 \\ &= \langle i^2 \rangle_{the} + \langle i^2 \rangle_{shot} + \langle i^2 \rangle_{sig-sp} + \langle i^2 \rangle_{sp-sp} + G_e NF_e \sigma_{Rx}^2 \end{aligned} \tag{39}$$

where G_e is the effective gain calculated using the multiplicative gain value of all the cascaded components and NF_e is the effective noise figure of the receiver electronics calculated using (38).

4.4.3 Simulation Parameters

Table 4.1 System Parameters

Parameters	Modified DSB-SC link	Modified OSSB link
Laser power	11.46 dBm	6 dBm
MZM1 insertion loss	L = 7 dB	L = 7 dB
MZM1 switching voltage	$V_{\pi 1} = 5.5V$	$V_{\pi 1} = 5.5V$
EDFA1 gain	G = 25 dB	G = 25 dB
BPF1	L = 10 dB	L = 10 dB
MZM2 insertion loss	L = 5 dB	L = 5 dB
MZM2 switching voltage	$V_{\pi 2} = 6.1$ V	$V_{\pi 2} = 5.5$V
EDFA2	G = 15 dB	G = 25 dB
Waveshaper	L = 12 dB	L = 12 dB
PD responsivity	0.5 A/W	0.5 A/W
Electric BPF	L = 5 dB	L = 5 dB
Amplifier	G = 10 dB	G = 10 dB

To calculate how different noise sources contribute to the total system noise, numerical simulation was utilised. The gain and insertion loss of all the optical and electrical devices were measured from our experimental setup. Table 4.1 shows the system parameters (insertion losses, gains, PD responsivity, etc.) measured in the experimental setup for the two fronthaul links. These parameters are used in the fronthaul link coefficients A and B in (11) and (22) in Section

4.2 and 4.3, which will be used to calculate the SNR of the transmission links. The parameters shown in Table 4.1 are typical values for 60-GHz RoF transmission.

To investigate the total power consumption of the proposed two fronthaul links, we follow the methods and models given in [153-155]. For the detailed mathematical equations and calculations, please refer to the references. The power consumption of various components in the fronthaul links are shown in Table 4.2. The estimated total power consumptions of the modified DSB-SC and OSSB links are 79.192 watts and 79.162 watts, respectively.

Table 4.2 Power Consumption of Various Components in Two Fronthaul Schemes

	Components	**Modified DSB-SC link**	**Modified OSSB link**
BBU	DAC	0.0258 W	0.0258 W
	Laser	0.125 W	0.036W
	MZM1	0.3 W	0.3 W
	EDFA1	10.021 W	10.021 W
	MZM2	0.3 W	0.3 W
	EDFA2	9.965 W	10.021 W
RRH	Photodiode	0.157 W	0.157 W
	Amplifier	0.1 W	0.1 W
CU	Amplifier	0.1 W	0.1 W
	ADC	0.1023 W	0.1023 W
	DSP chips	58 W	58 W
	Total power consumption	79.192 W	79.162 W

4.4.4 Simulation Results

Shown in Fig. 4.8 are the EVM curves obtained by the derived analytical models together with the above-mentioned noise model. Also shown are the back-to-back experimental results for the modified DSB-SC and OSSB schemes that have been measured in Chapter 3, Section 3.3.2. Both DSB-SC scheme and OSSB scheme with various data rates can obtain a close match between experiments and simulation results. This confirms that the proposed fronthaul links are noise-limited and it is reasonable to neglect the nonlinear effects caused by modulators and amplifiers in the analytical models. The derived analytical models could reflect the link performance and can be further used to characterise the impact of system parameters on link performance.

On the other hand, the experimental and analytical results in Fig. 4.8 show that: for the same symbol rate, the EVM curves in DSB-SC and OSSB schemes will overlap when received optical power is high, i.e. the two schemes have similar noise floor. Hence, we can conclude that the link performance degradation in DSB-SC scheme results from its inherently higher OCSR compared with OSSB scheme at the same received optical power. Moreover, OSSB fronthaul link can also overcome the fibre chromatic dispersion induced power fading effect, which makes it a good option for short-reach analog fronthaul links.

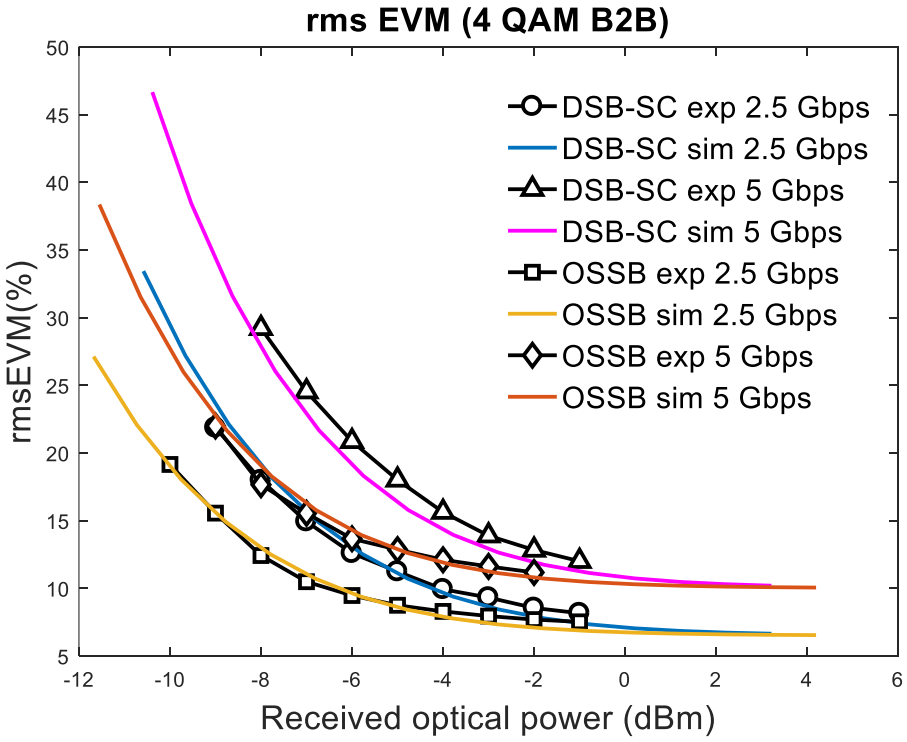

(a)

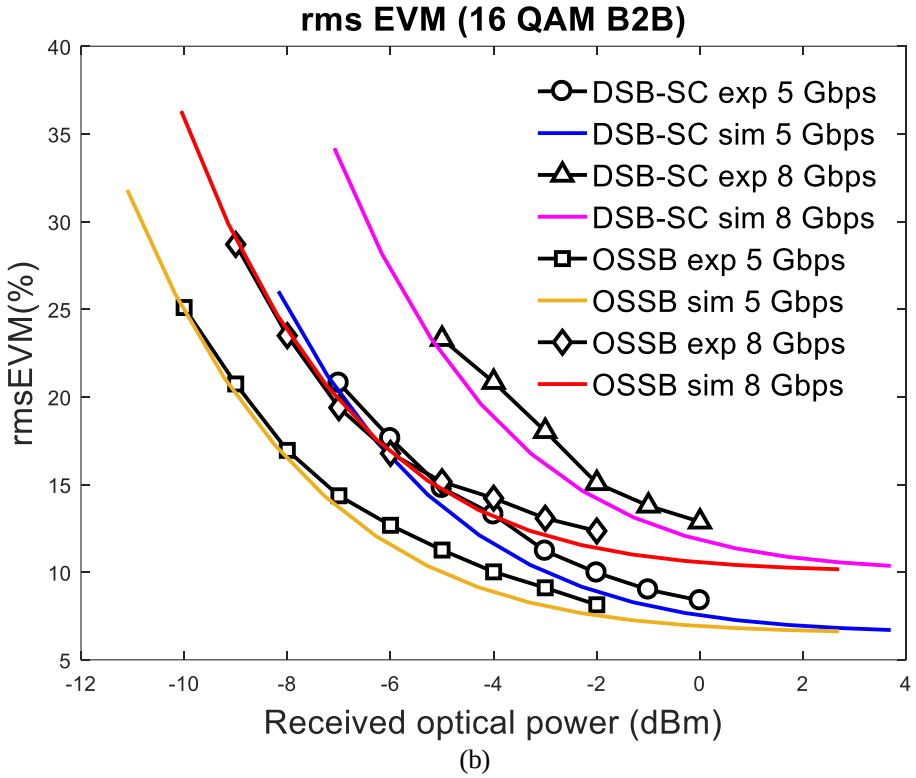

(b)

Fig. 4.8 Experimental and numerically simulated EVM curves against received optical power for (a) transmitting 4 QAM and (b) 16 QAM signal in the proposed two fronthaul schemes.

4.5 Dispersion Impact on the Modified DSB-SC Fronthaul Scheme

The modified OSSB fronthaul scheme is immune to the RF power fading caused by fibre chromatic dispersion in the fronthaul fibre links. This has been confirmed in the experimental results in Chapter 3. The performance of the modified DSB-SC scheme, on the other hand, is limited by the dispersion effect. In this section, the analytical model of the modified DSB-SC fronthaul link is updated considering the impact of chromatic dispersion after transmitting the mm-wave signal over different lengths fibre link.

When an electromagnetic wave propagates through fibre optic, different spectral components will have different phase velocity and group velocity. This phenomenon is referred to as chromatic dispersion and originates from the frequency dependence of the refractive index. Expanding the propagation constant β in a Taylor series around the centre frequency ω_c yields

$$\beta(\omega) = \beta_0(\omega_c) + \beta_1(\omega_c)(\omega-\omega_c) + \frac{1}{2}\beta_2(\omega_c)(\omega-\omega_c)^2 + \frac{1}{6}\beta_3(\omega_c)(\omega-\omega_c)^3 + \cdots \quad (40)$$

Where $\beta(\omega) = \left.\frac{d^m\beta}{d\omega^m}\right|_{\omega=\omega_0}, (m = 0,1,2,...)$.

The zero-order term in (40) describes a constant phase shift. The first order term contains the group velocity and is related to the overall time delay. The second order term is composed of the second-order dispersion and can be represented using the chromatic dispersion parameter D, the optical carrier wavelength λ_c, and the speed of light c as follows

$$\beta_2(\omega_0) = -\frac{D\lambda_c^2}{2\pi c} \quad (41)$$

As depicted in Fig. 4.9, when the optical field propagates through SMF with length L (km), the impact of fibre attenuation (α km^{-1}) and chromatic dispersion can be modeled as

$$E_{out}(t) = E_{in}(t)\cdot\exp(-j\beta(\omega)L)\cdot\exp(-\frac{\alpha L}{2}) \quad (42)$$

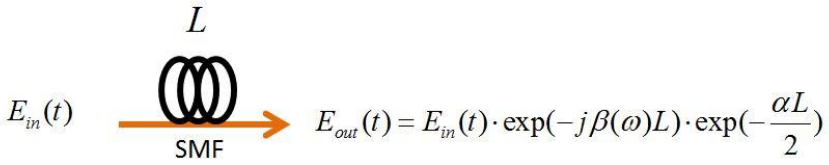

Fig. 4.9 Optical signal at the input and output of SMF with length L

The input optical field in the modified DSB-SC fronthaul scheme is expressed as (8). After the optical filtering, the optical mm-wave signal will be transmitted along the fibre fronthaul link with length L. The resulted output optical field in time domain is written as

$$\begin{aligned} E_{out}(t) = & \frac{E_0\sqrt{L_1L_2L_3L_4G_1G_2}}{2}\{jJ_1(a)(e^{j\phi_1}e^{j(\omega_c+\omega_{mm})t} + e^{-j\phi_1}e^{j(\omega_c-\omega_{mm})t}) \\ & + \frac{j\pi J_1(a)}{2V_{\pi 2}}[(I(t)+jQ(t))\cdot e^{j\phi_1}e^{j(\omega_c+\omega_{mm}+\omega_0)t} \\ & + (I(t)-jQ(t))\cdot e^{-j\phi_1}e^{j(\omega_c-\omega_{mm}-\omega_0)t}]\}\cdot\exp(-j\beta(\omega)L)\cdot\exp(-\frac{\alpha L}{2}) \end{aligned} \tag{43}$$

To simplify (43), only the second order derivative of the propagation coefficient which is related to chromatic dispersion will be considered. As a result, (43) is simplified to

$$\begin{aligned} E_{out}(t) = & \frac{E_0\sqrt{L_1L_2L_3L_4G_1G_2}}{2}\{jJ_1(a)[\exp(j\phi_1 + j(\omega_c+\omega_{mm})t - \frac{j\beta_2}{2}\omega_{mm}^2L) \\ & + \exp(-j\phi_1 + j(\omega_c-\omega_{mm})t - \frac{j\beta_2}{2}\omega_{mm}^2L)] \\ & + \frac{j\pi J_1(a)}{2V_{\pi 2}}[(I(t)+jQ(t))\cdot\exp(j\phi_1 + j(\omega_c+\omega_{mm}+\omega_0)t - \frac{j\beta_2}{2}(\omega_{mm}+\omega_0)^2L) \\ & + (I(t)-jQ(t))\cdot\exp(-j\phi_1 + j(\omega_c-\omega_{mm}-\omega_0)t - \frac{j\beta_2}{2}(\omega_{mm}+\omega_0)^2L)]\}\cdot\exp(-\frac{\alpha L}{2}) \end{aligned} \tag{44}$$

Upon photodetection at the photodiode, the received photocurrent is written as

$$
\begin{aligned}
i_p(t) &= \Re(E_{out} \cdot E_{out}^{*}) \\
&= \frac{2\Re E_0^2 L_1 L_2 L_3 L_4 G_1 G_2 \pi J_1^2(a)}{V_{\pi 2}} e^{-\alpha L} \cos(\frac{\beta_2 L}{2}(\omega_0^2 + 2\omega_{mm}\omega_0)) \times \\
&\{Q(t)\cos(2\omega_{mm}t + \omega_0 t + 2\phi_1) - I(t)\cos(2\omega_{mm}t + \omega_0 t + 2\phi_1)\}
\end{aligned}
\tag{45}
$$

In (45), only the desired RF frequency components with frequency of $2\omega_{\mathrm{mm}} + \omega_0$ are considered and all the other frequency components can be filtered using a bandwidth limited BPF in the receiver electronics. The received electric RF mm-wave signal after amplification and bandpass filtering after photodetection is given by

$$
\begin{aligned}
RF = e^{-\alpha L} \cos(\frac{\beta_2 L}{2}(\omega_0^2 + 2\omega_{mm}\omega_0)) \frac{\Re E_0^2 L_1 L_2 L_3 L_4 L_5 G_1 G_2 G_3 J_1^2(a)\pi}{2V_{\pi 2}} \times \\
[Q(t)\sin(2\omega_{mm}t + \omega_0 t + 2\phi_1) - I(t)\cos(2\omega_{mm}t + \omega_0 t + 2\phi_1)]
\end{aligned}
\tag{46}
$$

Therefore, the RF power fading effect induced by the chromatic dispersion can be derived from (46). The received RF power of the mm-wave signal is dependent on the dispersion parameter, the fibre length and the frequencies involved during the data modulation (ω_0) and optical carrier generation (ω_{mm}) stages in the modified DSB-SC scheme:

$$
P_{RF} \propto \cos^2(\frac{\beta_2 L}{2}(\omega_0^2 + 2\omega_{mm}\omega_0)) = \cos^2(\pi c L D \frac{f_0^2 + 2 f_0 f_{mm}}{f_c^2})
\tag{47}
$$

It should be noted that in (47), the received RF power variation is not directly dependent on the desired mm-wave signal frequency ($2\mathrm{f}_{\mathrm{mm}} + f_0 = 60.25GHz$). This is due to the utilisation of two-stage external modulation in the modified DSB-SC scheme. Now we compare the RF power fading phenomenon in the modified DSB-SC scheme with the traditional single stage DSB modulation scheme. In a single stage DSB modulation scheme, the RF power of the desired mm-wave frequency $2\mathrm{f}_{\mathrm{mm}} + f_0$ will vary approximately as [144]

$$
P_{RF}^{'} \propto \cos^2(\pi c L D \frac{(2 f_{mm} + f_0)^2}{f_c^2})
\tag{48}
$$

Shown in Fig. 4.10 is the calculated RF power degradation against the fibre transmission distance for the modified DSB-SC scheme and the conventional single stage DSB scheme. The

RF power degradation is defined as the power difference between the received RF signal power before and after fibre transmission. As can be seen in Fig. 4.10, the dispersion effect presents a cyclic behaviour where the received RF signal power vanishes periodically. However, the modified DSB-SC scheme is less sensitive to the fibre chromatic dispersion effect compared to the single stage DSB scheme. By properly designing the fibre transmission length of the modified DSB-SC fronthaul link, the dispersion effect can be less of an issue than the conventional single stage DSB modulation scheme.

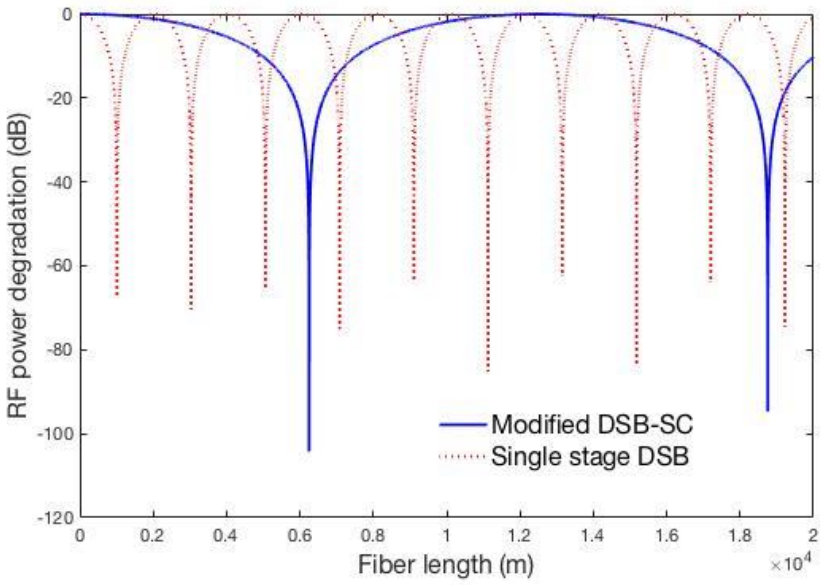

Fig. 4.10 Degradation of RF power versus fibre propagation distance for the modified DSC-SC scheme and the conventional single stage DSB scheme

4.6 Summary

In this chapter, thorough analytical models of the proposed analog mm-wave RoF fronthaul schemes for downlink transmission were presented and discussed. Received RF signal power in the two fronthaul schemes are given as a function of the system OCSR. Simulation results showed that RF signal power in the modified DSB-SC scheme was smaller than in the OSSB scheme resulting from a much larger OCSR in DSB-SC scheme. As a result, the intrinsic larger OCSR in DSB-SC scheme resulted in link performance degradation compared with the OSSB

scheme. The noise sources in the electrical and optical devices in the analog fronthaul link were also theoretically analysed, such as thermal noise, quantum shot noise, signal-spontaneous noise, and spontaneous-spontaneous noise. The mathematical expression of the total noise power in the fronthaul system was derived and presented to further evaluate the system performance. Besides, the power consumptions of the fronthaul schemes were calculated and presented using typical system parameters for 60-GHz RoF transmission.

The derived analytical models were confirmed to match the experimental results closely, thus offering a useful tool to predict the performance dependence on the system parameters in mm-wave RoF fronthaul design.

Finally, the impact of fibre chromatic dispersion on the fronthaul performance in the modified DSC-SC scheme was analytically investigated. The exact time domain analytical model of the dispersion induced RF power fading was derived. Compared with the convention single stage DSB modulation technique, the proposed modified DSB-SC scheme is less sensitive to the dispersion effect and is more applicable in real applications for short-reach fronthaul links.

Chapter 5 Advanced Techniques in Fronthaul Networks

5.1 Introduction

The fifth generation (5G) communication networks demand a capacity growth of 1000-fold, data rate increase by a factor of 10 [2], and latency as low as 1 microsecond [156] compared with the current communication networks. Among the many potential candidates of 5G, coordinated multipoint (CoMP) transmission and non-orthogonal multiple access (NOMA) [103] have the merits of achieving transmission diversity and spectrum efficiency with low decoding complexity, thus it is feasible to further improve cell-edge throughputs [10] and coverage of high data rates small cells in the next generation communication networks.

The main challenges of employing CoMP in backhaul networks comprise three aspects. Firstly, the delay caused by network node processing and the line delay along fronthaul links is usually assumed to be ideal with no latency [3]. These assumptions are hardly true in real applications and will not meet the low latency requirement of 5G networks. Secondly, large amount of data (channel state information, control signal, and user data) need to be exchanged among different cell sites [10], resulting in a severe issue impacting on cell densification. Moreover, synchronisation of signal timing offsets (STOs), carrier frequency offsets (CFOs), and random phase rotation originated from wireless channels are required simultaneously for coordinated links. The overlapped signals from coordinated access points at the user equipment make it tougher to estimate and compensate the different offsets between the two branches. An effective solution to bypass the latency, enormous signaling overhead, and synchronisation requirements is to deploy the CoMP function in analog fronthaul links. The centralised BBUs in fronthaul links have the intrinsic advantages of providing much lower latency, readily synchronised phase and frequency local oscillator (LO) signals, as well as handy resources sharing architecture for joint signal processing. Hence, CoMP implementation is of cardinal importance to achieve a significant performance gain in the next generation small cell scenarios.

A photonic-aided CoMP transmission by using space-frequency block coding in mm-wave RoF system was demonstrated in [94] to attain CoMP gains. A stochastic gradient algorithm was proposed in [87] to deal with the uncertainties caused by imperfect channel state information at transmitters. Potential solutions to combat the impact of fronthaul-constrained radio access networks on large scale coordinated signal processing and resource allocation optimisation were discussed in [13].

On the other hand, to meet the requirements of 5G network of improved spectral efficiency, a larger user-base and low transmission latency [115, 157], non-orthogonal multiple access (NOMA) has been introduced for future radio access. In contrast to orthogonal multiple access (OMA) schemes in which signals are multiplexed in frequency/time/code domain, conventional NOMA schemes achieve multiplexing in the power domain. Signals of multiple users are multiplexed in the power domain linearly at the transmitter using superposition code (SPC) and successive interference cancellation (SIC) is required for multi-user signal detection at the receiver side [102]. However, the utilisation of SPC and SIC suffers from practical issues including increased receiver complexity, incompatible with latency sensitive applications and increased error propagation that will degrade the fronthaul link performance.

In this chapter, we experimentally demonstrated a 60-GHz mm-wave RoF fronthaul network incorporating two advanced techniques including CoMP and NOMA downlink transmission scheme. The two techniques are first demonstrated in the downlink fronthaul RoF system separately. Then a multi-cell NOMA fronthaul system with coordinated base stations (BSs) are experimentally demonstrated for the first time to exploits the diversity gain introduced by CoMP and the spectrum efficiency induced by NOMA simultaneously.

Firstly, the experimental results of CoMP based fronthaul network shows that 1.3-dB receiver sensitivity improvement can be achieved compared with two fronthaul links transmission without CoMP function. The coordinated fronthaul scheme could tolerate higher time delays than would be possible for two channels transmission without space-time block coding (STBC) under rough synchronisation.

Secondly, to overcome the limitations imposed by SPC/SIC NOMA, we demonstrate a multi-user access scheme over 60-GHz RoF fronthaul incorporating NOMA based on a novel multilevel code (MLC) scheme that does not require SIC operation at the receiver. Total bit

rate of 8 Gbps for two users was achieved with 3-km fibre fronthaul and 2.5-m wireless transmission. Experimental results show that our proposed MLC NOMA scheme achieves improved spectral efficiency, simplified receiver design and increased cell coverage compared with typical SPC NOMA scheme. In addition, there is no error propagation from far user to near user, enabling more flexible power allocation ratio design at the transmitter.

Finally, we combine two advanced techniques and demonstrated the applicability of the fronthaul networks employing NOMA scheme with coordinated BSs. The performance of MLC-based NOMA with CoMP scheme is compared with the SPC-based NOMA with CoMP scheme, where larger range of power allocation ratio is feasible in the former scheme enabling more flexible NOMA pair clustering at the BBU. In addition, higher data rate is possible as well as extended mm-wave small cell coverage.

This chapter is organised as follows: section 5.2 presents the downlink 60-GHz RoF fronthaul system with CoMP transmission, including the principle of implementation, channel estimation technique in CoMP fronthaul system, time delay compensation approach and the experimental demonstration. In section 5.3, the proposed MLC-based NOMA scheme is deployed in the fronthaul system and the performance improvements compared with traditional SPC-based NOMA scheme are verified in the experiments. The applicability of combined NOMA with CoMP function in fronthaul scenario is discussed in section 5.4, where MLC-based NOMA with coordinated BSs in downlink fronthaul is demonstrated for the first time with a total data rate of 6 Gbps (three users) over a transmission distance of 10 km of optical fibre and 1.24-m wireless distance.

5.2 CoMP for Downlink 60 GHz RoF Fronthaul

5.2.1 Implementation of STBC in 60 GHz RoF Fronthaul

We consider a typical 2 × 1 coordinated RoF fronthaul network employing the orthogonal rate-1 STBC, i.e. Alamouti code [158], in the centralised BBU pool as depicted in Fig. 5.1. The centralised BBU provides 60-GHz optical mm-wave signals generation function and joint signal processing for coordinated signal transmission over RoF fronthaul links to separate RRHs. The combination diversity is realized at the user equipment (UE) located at the cell

boundaries of two small cells, followed by channel state information (CSI) estimation at the receiver and maximum likelihood decoding. In this regard, space-time diversity gain is obtained to improve the achievable data rate of the cell-edge user and the coverage of 60-GHz small cells.

The baseband data symbols at BBU are grouped into pairs for Alamouti coding. Denoting the two symbols to be transmitted by RRH1 (resp., RRH2) over the first and second time slots are x_1 and $-x_2^*$ (resp., x_2 and x_1^*). Then, the corresponding signals received at the cell-edge UE during the first and second time slots are

$$\begin{aligned} y(1) &= h_1(1)x_1 + h_2(1)x_2 + n_1(1) \\ y(2) &= -h_1(2)x_2^* + h_2(2)x_1^* + n_2(2) \end{aligned} \tag{1}$$

where $h_i(j)$ and $n_i(j)$ is the channel coefficient and Gaussian distributed noise between the i-th RRH and UE at j-th time slot, and $i, j \in \{1,2\}$, respectively. Due to the propagation characteristics of 60-GHz mm-wave signals, very fast fading caused by multipath effect can be safely ignored [94] without significant influence on the performance. In this scenario, only slow fading (shadowing effect) and very slow fading (path loss and oxygen absorption) [30] are considered and the coherent time of the channel is large compared to the delay requirement. Hence, the channel response is considered invariant over two time slots. In this case, we have $h_1(1) = h_1(2)$ and $h_2(1) = h_2(2)$.

For convenience, we express (1) as follows:

$$\begin{bmatrix} y(1) \\ y(2)^* \end{bmatrix} = \begin{bmatrix} h_1(1) & h_2(1) \\ h_2^*(1) & -h_1^*(1) \end{bmatrix} \begin{bmatrix} x_1 \\ x_2 \end{bmatrix} + \begin{bmatrix} n_1(1) \\ n_2(2)^* \end{bmatrix} = HX + N \tag{2}$$

As can be seen in (2), the time invariant properties of mm-wave wireless channels guarantee the orthogonality (H is an orthogonal matrix) of Alamouti code. The estimated signal at UE is therefore denoted as

$$\begin{bmatrix} \hat{x}_1 \\ \hat{x}_2 \end{bmatrix} = (H^H H)^{-1} H^H \begin{bmatrix} y_1 \\ y_2^* \end{bmatrix} \tag{3}$$

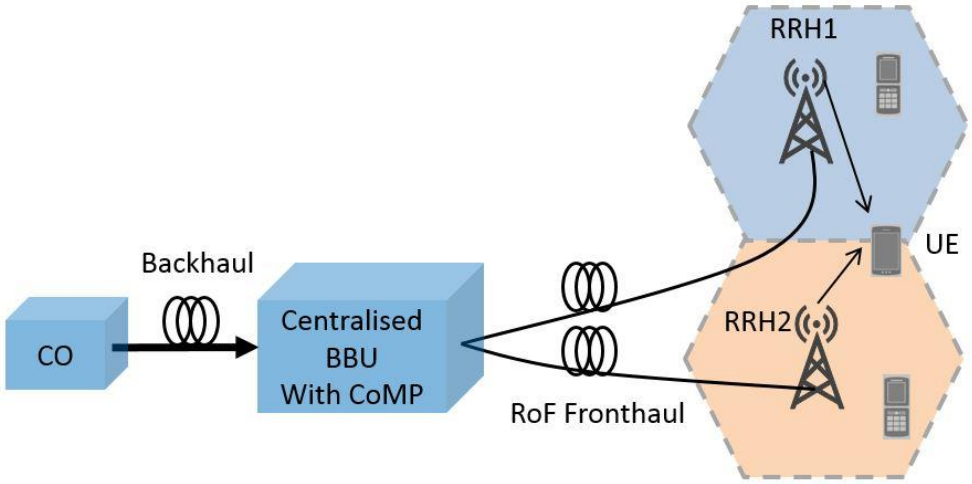

Fig. 5.1 60-GHz millimetre-wave radio-over-fibre fronthaul and radio access networks with coordinated multipoint transmission (CO: central office, BBU: baseband unit, RRH: remote radio head, UE: user equipment).

5.2.2 Downlink CoMP Channel Estimation

In general, there are two types of channel estimation, namely training-based channel estimation and blind-based channel estimation. In this work, we consider the training based approaches for downlink CoMP channel estimation. In the Alamouti STBC scheme, the received signal at the receiver is the superposition of the signals from two transmitting antennas. To accurately estimate the channel matrix, the training symbols in two channels should be carefully designed to avoid interference with each other.

Generally, three approaches can be exploited to avoid training symbol or pilot interference, including allocating training symbols in the time domain, frequency domain, and the space dimension [159]. In pilot allocation using the temporal orthogonality, pilots for two channels are transmitted at different time slots. In frequency domain pilot allocation, the pilots are transmitted on different carrier frequencies. While in spatial domain pilot allocation, pilots are designed to be orthogonal to each other. Therefore, the pilot sequences can be transmitted using the same time and frequency resources.

In offline signal processing, signal orthogonality is used to allocate the pilot sequence for the two coordinated channels. In the experiments, two pilot symbols are inserted before every 8 data symbols. The received pilot symbols during the first and second time slots are written as

$$\begin{aligned} y_1 &= h_1 p_1 + h_2 p_2 + n_1 \\ y_2 &= -h_1 p_2^* + h_2 p_1^* + n_2 \end{aligned} \tag{4}$$

Therefore, the estimated channel coefficients during the first and second time slots are given by

$$\begin{aligned} \hat{h}_1 &= \frac{y_1 p_1^* - y_2 p_2}{p_1 p_1^* + p_2 p_2^*} \\ \hat{h}_2 &= \frac{y_1 p_2^* + y_2 p_1}{p_1 p_1^* + p_2 p_2^*} \end{aligned} \tag{5}$$

Finally, interpolation is carried out to estimate the channel matrix in the entire subframe.

5.2.3 Time Delay Compensation in Coordinated Fronthaul Links

The centralised architecture of BBU has an inherent advantage of securing accurate clock, signal timing, and frequency synchronisation between two coordinated branches. Hence, the CFOs for two coordinated channels are identical and can be readily estimated and compensated by using conventional techniques. On the other hand, allowing for the fact that fixed latency induced by the fronthaul optical fibre can be pre-compensated, and that rough synchronisation is always adopted and easy to implement in practice [160], here we only consider the imperfect time synchronisation errors caused by the randomness of the wireless channels. As illustrated in Fig. 5.2, the time delay between two received signal-sequences from RRH1 and RRH2 is denoted as Δt, which is within one symbol period T. Taking this time misalignment into consideration, the received signals at UE at k^{th} time slot contains both the desired signals and the inter-symbol interference from previous time slot. The system degradation resulting from this inaccurate synchronisation in the fronthaul networks will be discussed in detail in Section 5.2.4.

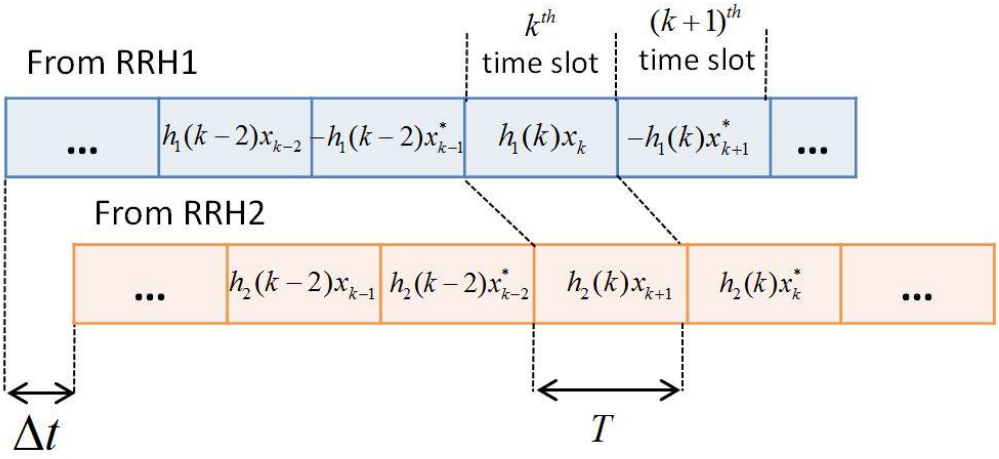

Fig. 5.2 Time delay between two received signal sequences from RRH1 and RRH2 at the UE.

5.2.4 Experimental Setup and Results

5.2.4.1 Experimental Setup

To evaluate the performance of coordinated fronthaul networks, we experimentally demonstrated a 60-GHz RoF fronthaul with CoMP function realised in the centralised BBU. As depicted in the experimental setup in Fig. 5.3 (a), an optical mm-wave carrier with a frequency separation of 57.75 GHz was generated using a 20 GHz dual-electrode Mach-Zehnder modulator (DE-MZM) biased at minimum transmission point to achieve optical carrier suppression (OCS) operation. Then an optical splitter was utilised to split the mm-wave carriers into two branches for CoMP implementation. Alamouti coding for coordinated transmission was applied on 4 QAM symbols which were then up-converted onto a 2.5-GHz intermediate frequency (IF) carrier offline in MATLAB. Data rate for both links was set to 4 Gbps. In addition, the time delay results from the fixed fibre length between two channels is measured to be $\Delta t = 120 ns$. To compensate for the time delay, 240 isolation symbols ($\text{Symbol period} = 0.5 ns$) are inserted before the signal that will be transmitted along the delayed channel. The coded data was loaded into an arbitrary waveform generator (AWG7102) for double sideband (DSB) data modulation of the two branches, respectively. As can be seen

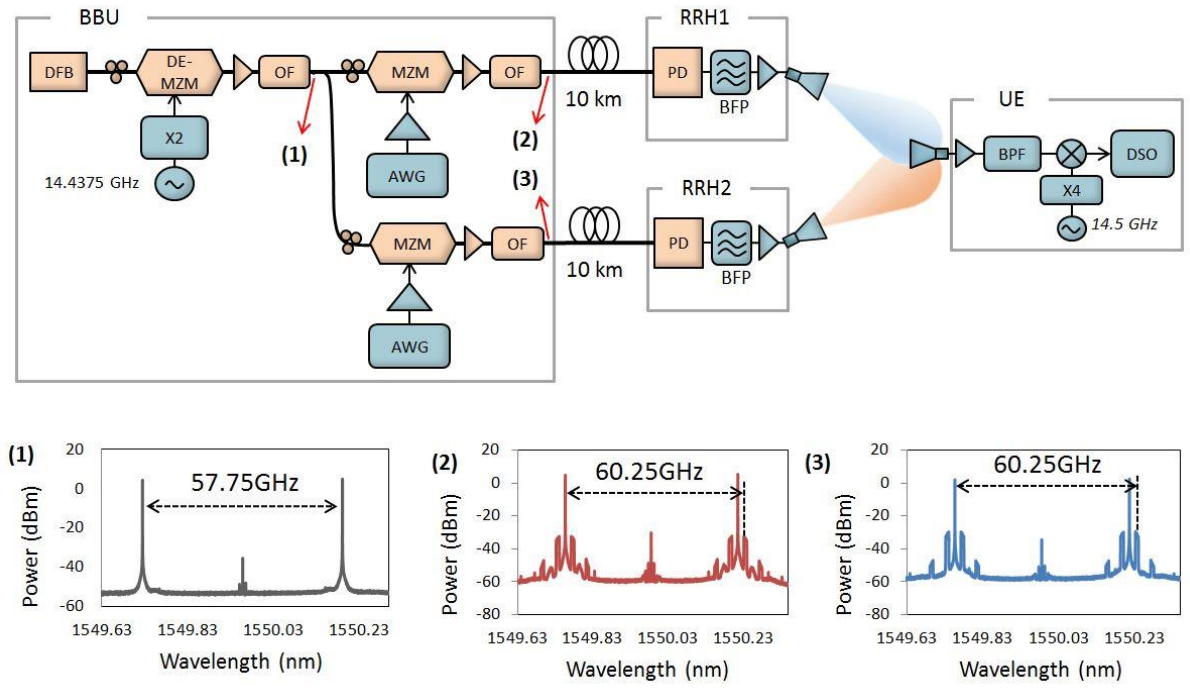

(a)

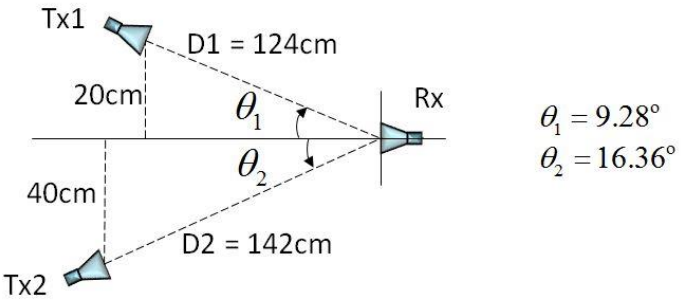

(b)

Fig. 5.3 (a) Experimental setup of CoMP based 60-GHz millimeter-wave radio-over-fiber fronthaul (CO: central office, BBU: baseband unit, RRH: remote radio head, UE: user equipment, X2: frequency doubler, X4: quadrupler). (b) Orientations of transmit and receive antennas

in insets (2) and (3) in Fig. 5.3 (a), 60.25-GHz mm-wave signals were generated. It should be noted that only the upper (resp. lower) sideband signal carried by upper (resp. lower) sideband optical carrier contain useful CoMP information. Erbium-doped fibre amplifiers (EDFAs) and optical bandpass filters (BPF) were deployed after each optical modulator to compensate for the insertion loss and to remove out-of-band amplified spontaneous emission (ASE) noise.

The well-synchronised CoMP signals were sent to RRH1 and RRH2 over 10-km of single mode fibre fronthaul link for wireless transmission. The horn antennas used in the RRHs and UE are circular horn antennas with 25 dBi gain with operating frequency range from 58 GHz to 68 GHz. In addition, the horn antennas have 3 dB beamwidth of 7°, which are reasonable to be used to emulate the nearly line-of-sight transmission property [94] of the 60 GHz mm-wave radio signals. The two antennas in RRH1 and RRH2 were adjusted to face towards the receiving antenna to achieve the best receive signal quality. Shown in Fig. 5.3 (b) is the orientations of the two transmit antennas and one receive antenna. The distances from the RRH1 and RRH2 antenna to the receive antenna are 1.24 m and 1.42 m respectively. The operating conditions of the two fronthaul links were optimised and maintained throughout the experiment.

Two copies of the received 60-GHz signals were received at the UE to obtain the CoMP signal. The received signal at UE was captured by a 40 GS/s digital storage oscilloscope (DSO) after being down-converted to 2.25 GHz. Offline signal processing including rough time synchronisation, CFO estimation, channel estimation, IF carrier down-conversion, maximum likelihood detection, and bit error rate (BER) performance evaluation were carried out with MATLAB.

5.2.4.2 CoMP Diversity Gain in 60 GHz Fronthaul

To demonstrate the diversity gain introduced by the employment of STBC in fronthaul links, the BER performance against received optical power is measured for the system with different transmission schemes, namely single channel transmission, two channels transmission with CoMP, and two channels transmission without CoMP. Single channel transmission is defined as QAM signal transmission using only one fronthaul link, while the other fronthaul link is idle and transmits no signals. Combined two channels transmission without CoMP is the scenario where two identical copies of signals are transmitted along two fronthaul links.

Fig. 5.4 shows the 60-GHz fronthaul link BER performance versus received optical power of CoMP fronthaul network (green line with circle), combined two channels transmission without CoMP (black line with diamond), and two single channels transmission (red line with triangle and blue line with square). The dashed line represents the 2.3×10^{-3} forward error correction (FEC) limit with 7% overhead. Fig. 5.4 (a) and (b) illustrate 4 QAM signal transmission along

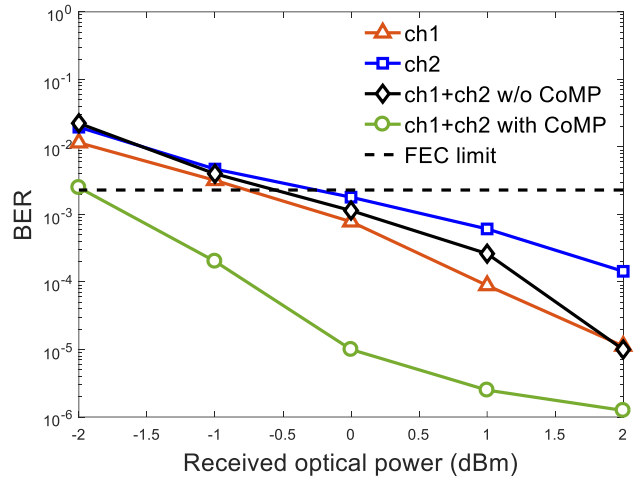

(a)

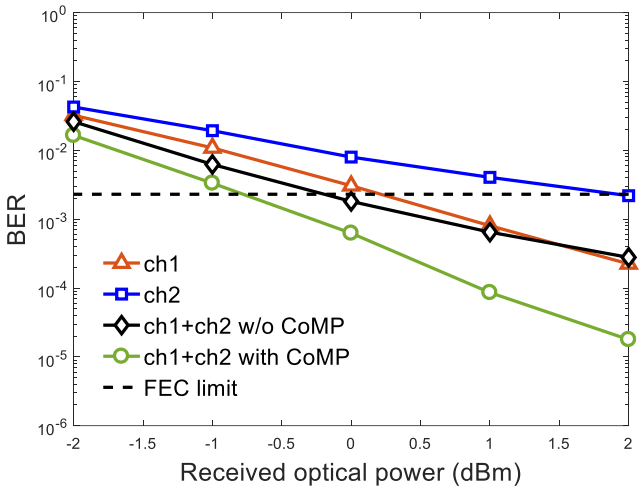

(b)

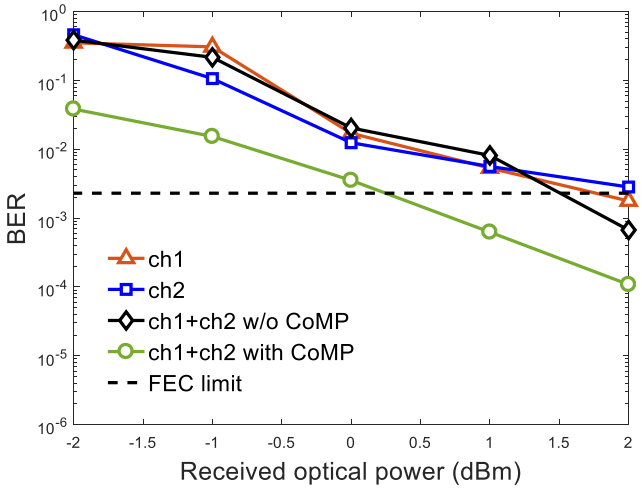

(c)

Fig. 5.4 BER against received optical power for transmitting (a) 2 Gbps 4 QAM signal over 0 km fronthaul link, (b) 4 Gbps 4 QAM signal over 0 km fronthaul link, and (c) 4 Gbps 4 QAM signal over 10 km fronthaul link

0-km fibre fronthaul link with data rate of 2 Gbps and 4 Gbps. While Fig. 5.4 (c) depicts 4 Gbps 4 QAM signals transmission over 10 km fibre fronthaul link. The BER performance is measured using antenna locations shown in Fig. 5.3 (b).

All the three investigated schemes can achieve acceptable performance below the FEC limit. However, performance gain can be realised with coordinated transmission of two fronthaul links. As shown in Fig. 5.4 (c), the optical receiver sensitivity of CoMP fronthaul is increased by ~ 1.3 dB at FEC limit in contrast with two channels transmitted simultaneously without CoMP function. The performance of two channels transmission without CoMP function falls in between single channels transmission even though higher received power is achieved (combined signal power from both RRHs) in the former scenario. This is due to the fact that the performance degradation resulted from the randomness of the two combined channels cannot be completely overcome without STBC. On the other hand, it also confirms that the performance gain of CoMP fronthaul link does not originate from increased received power at the UE. The diversity gain will therefore increase the achievable data rate boundary of fronthaul networks and extend the mm-wave small cell coverage.

5.2.4.3 Impact of Synchronization Errors

Combined with centralised BBU architecture in millimetre wave radio-over-fibre fronthaul, CFO synchronisation between two wireless branches is not an issue. Since two coordinated links shared the same LO in the BBU for mm-wave carrier generation, the CFOs induced by LO frequency and phase mismatch between the BBU and UE is identical between two coordinated fronthaul links. Thus, conventional training sequence based CFO estimation was applied in signal post-processing.

To assess the impact of imperfect timing synchronisation in CoMP fronthaul links, varied time delays (Δt) within one symbol period ($5\text{x}10^{-10}$ second) were intentionally induced in signal sequence from RRH2 as shown in Fig. 5.2. The data rate is kept as 4 Gbps and the length of the fibre fronthaul link is 10 km. Received optical power is fixed at -3 dBm for both fronthaul systems with and without CoMP for fair comparison. Experimental results in Fig. 5.5 illustrates that coordinated fronthaul links have acceptable BER performance with time delay within ±2 samples (5 samples in total in one symbol period), while the performance of the fronthaul links

without CoMP is more sensitive to time delay and will degrade rapidly with time delay larger than 1 sample.

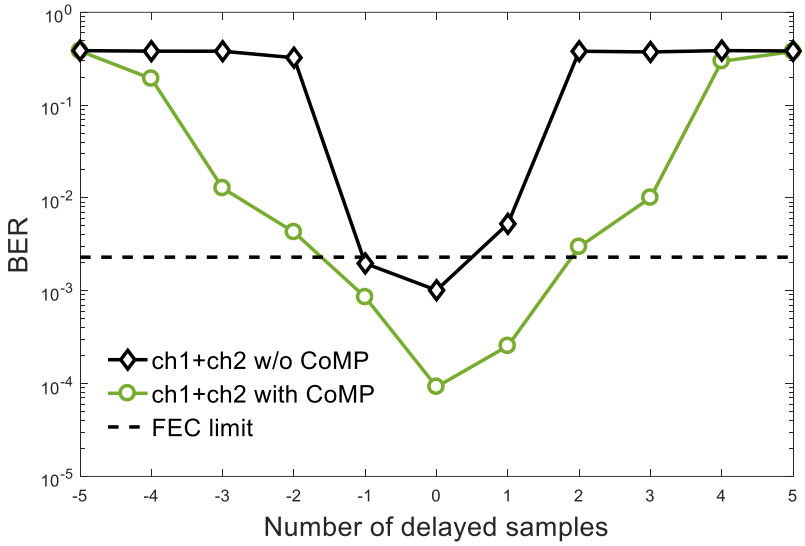

Fig. 5.5 Time delay tolerance of two channels transmission with and without CoMP transmission

5.2.4.4 CoMP Fronthaul Link Performance Characterization

In this section, experimental results will be demonstrated and discussed with regard to CoMP fronthaul link performance, including characterising the impact of signal angle of arrival, distance between two transmitters in coordinated fronthaul links, the range of reception area, and sensitivity to antennas angle misalignment. These system characterisations offer thorough references for future 60 GHz CoMP fronthaul link design. The data rate is kept as 4 Gbps and the length of fibre fronthaul link is 10 km in the following proof-of-concept demonstration.

Considering the path loss due to free space propagation and oxygen absorption, the transmission range of 60-GHz radio signals is limited within 100 meters for high speed data transmission. To overcome the atmosphere attenuation and to extend the transmission distances, beamforming and multiple-input and multiple-output (MIMO) techniques are often used in the system to switch the signal direction of propagation. The directional transmission of 60-GHz

radio signals can be achieved using horn antennas or antenna arrays. Currently, off-the-shelf 60-GHz antenna arrays are still not commercially available. Hence, we perform the investigation experiments with commercially available horn antennas to emulate the beamforming characteristics of 60 GHz radio signals. In [161], a similar approach is used where horn antennas are used to emulate the performance of a 10×10 antenna array.

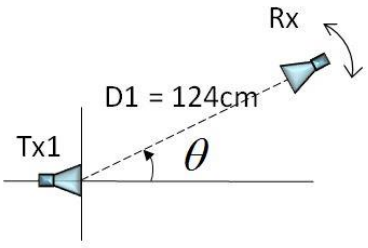

(a)

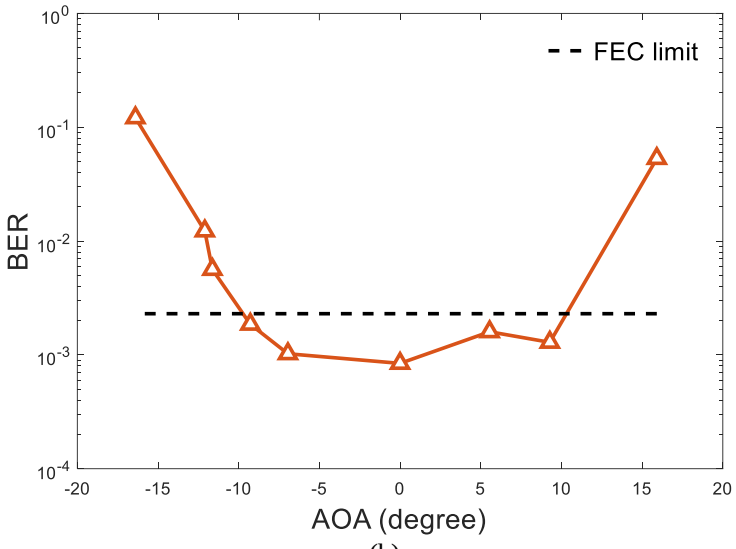

(b)

Fig. 5.6 (a) Orientation of transmit and receive antennas for characterising the impact of signal angle of arrival. (b) BER results as a function of angle of arrival

We start by evaluating the impact of signal angle of arrival (AOA) in the context of 1×1 (one transmit antenna and one receive antenna) single channel transmission. As shown in Fig. 5.6 (a), the transmit antenna is fixed while the receive antenna moves around the transmit antenna. The distance between two antennas is maintained as $D_1 = 124\ cm$. Meanwhile, the receive antenna is adjusted to always point to the transmit antenna. The AOA of the 60 GHz radio

signal is denoted as θ, which shows the direction of propagation of the radio signal incident on the antenna. Fig. 5.6 (b) illustrates the measured BER performance as a function of the AOA of the 60 GHz radio signal. As can be seen, the BER performance is acceptable within ±10˚ angle of arrival, which is determined by the 3 dB beamwidth of the circular horn antennas. With higher received optical power at the RRH and higher gain antennas, the transmission distance can be improved as well as the acceptable AOA at the receiver.

We then evaluate the optimum distance between two coordinated RRHs in the CoMP fronthaul system. Generally, multiple transmit antennas are positioned as far as possible in order to achieve maximum diversity gain [162]. This is due to the fact that the received two copies of coordinated signals will experience independent fading when two transmit antennas are geographically separated from each other. However, considering the radiation pattern of receive antenna, the distance between two transmit antennas is limited. Hence, an optimum distance between two transmit antennas exists in the CoMP fronthaul system. Fig. 5.7 (a) shows the locations of two transmit antennas and one receive antenna. The distances between the transmit antenna and the receive antenna are $\mathrm{D}_1 = D_2 = 124\ cm$. The distance between two transmit antennas is denoted as $\Delta \mathrm{d}_{\mathrm{Tx}}$. To measure the BER performance against the distance between transmit antennas, we manually adjust the distance between two transmit antennas. The distances between transmit and receive antennas are maintained the same throughout the investigation. The two transmit antennas are always directed towards the receive antenna to get optimum receive signal quality. The resulted BER performance against the distance between transmit antennas is depicted in Fig. 5.7 (b). We can see that the BER performance is improved as we increase the distance between transmit antennas from 10 cm to 40 cm. However, the BER performance will degrade if the distance is further increased. The minor BER degradation at distance equals to 10 cm is resulted from the interference between the beam patterns of two coordinated channels and the similar fading channels when antennas are placed close to each other. Besides, the BER degradation at distance higher than 40 cm is resulted from the limited directional radiation pattern of the receiver. Finally, we confirm that the optimum distance between transmit antennas is 40 cm ($\theta = 9.28°$) in the proposed coordinated fronthaul system.

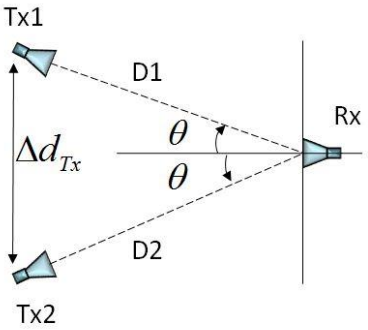

(a)

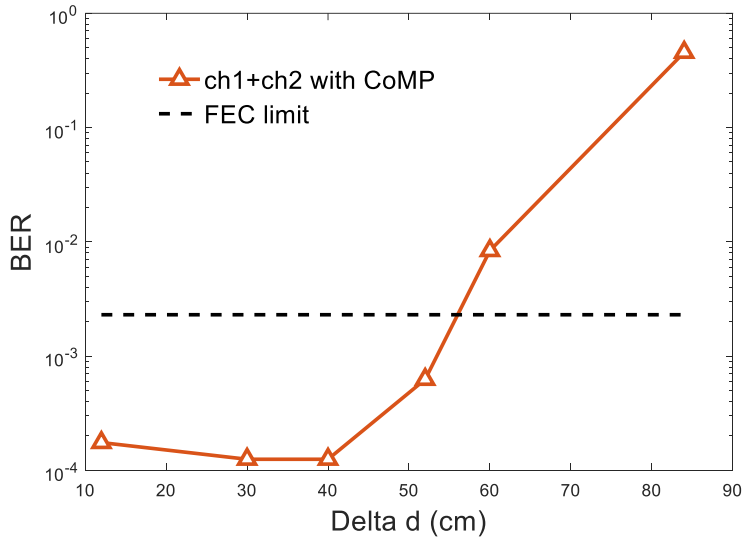

(b)

Fig. 5.7 (a) Orientation of transmit and receive antennas for verifying the optimum distance between coordinated RRHs. (b) BER performance as a function of the distance between two transmit antennas in the CoMP fronthaul system

The system robustness to antenna direction misalignment is also an issue that should be considered when designing a coordinated fronthaul system. The antennas misalignment results from inaccurate information of the user location or user movement which is faster than the user location information updates. We use the antennas orientation in Fig. 5.8 (a) to evaluate the impact of antennas misalignment in the coordinated fronthaul system. In Fig. 5.8 (a), the distances between transmit and receive antennas are $D_1 = D_2 = 124\,cm$. The distance between two transmit antennas is kept at the optimum value of 40 cm. To emulate the antenna misalignment, we manually adjusted the direction of two transmit antennas symmetrically and plotted the BER performance as a function of the angle α in Fig. 5.8 (b). Here we define α as

the transmitter AOA for simplicity. When $\alpha = 9.28°$, the coordinated system achieves the best BER performance as the two transmit antennas are pointed towards the receive antenna. Received signal quality degrades with decreasing AOA of the transmitter. The results show that the proof-of-concept fronthaul system is able to handle around ±7.8˚ antenna misalignment for the antenna arrangement in Fig. 5.8 (a).

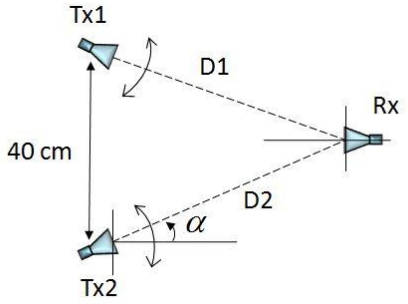

(a)

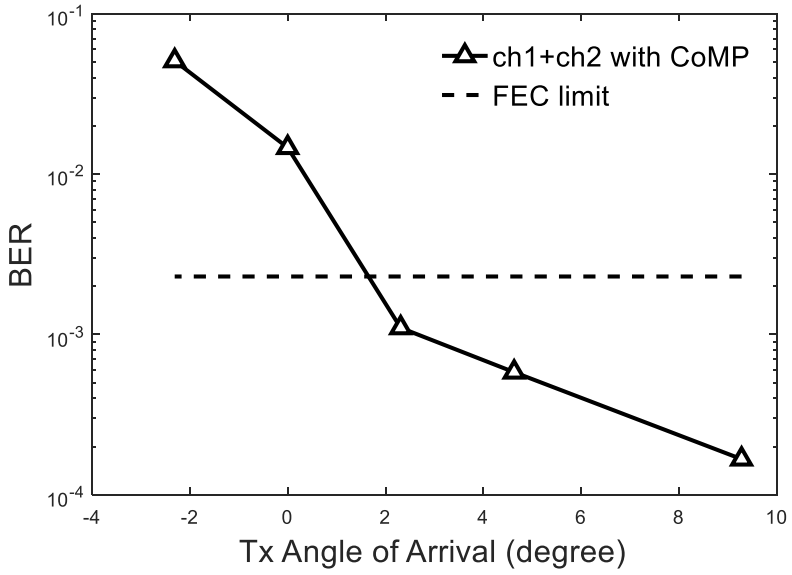

(b)

Fig. 5.8 (a) Orientation of transmit and receive antennas for evaluating the system robustness to antenna misalignment. (b) BER as a function of transmitter angle of arrival.

Finally, we study the effective reception area of the user for the antenna arrangement in Fig. 5.9 (a). We consider the scenario where the user moves along the y axis with its direction perpendicular to the x axis. During the user movement, the transmit antennas are always pointed to the original location of the receive antenna. The distance of the user from the origin

is denoted as Δd_{Rx}. As the user moves away from the origin point, received signal quality will be degraded. The tolerable distance of user movement is around ±17 cm, corresponding to minor movements such as posture change of the user. With higher gain antennas and higher received optical power at the RRHs, larger effective reception area is possible to cover user movements up to a few meters.

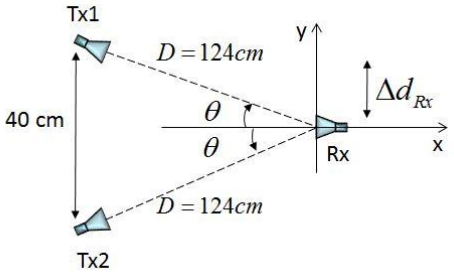

(a)

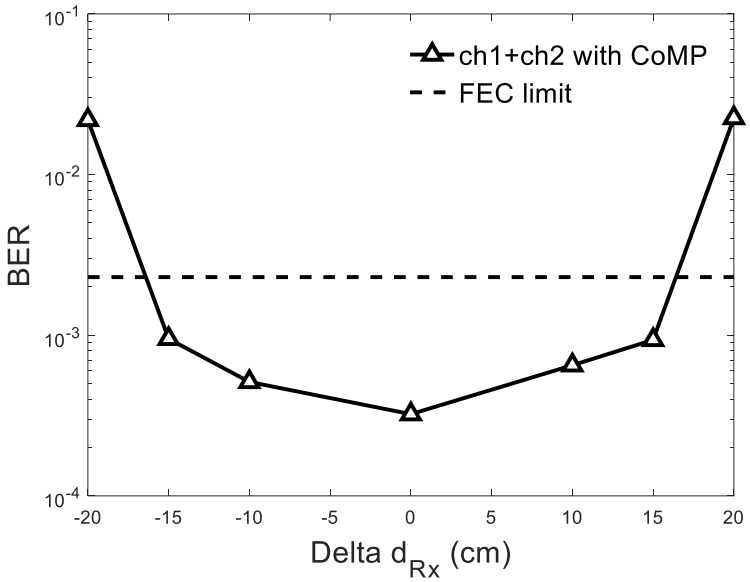

(b)

Fig. 5.9 (a) Orientation of antennas for measuring the effective reception area of the receiver. (b) CoMP fronthaul system BER performance as a function of $\Delta \mathbf{d_{Rx}}$

5.3 NOMA for Downlink 60 GHz RoF Fronthaul

In this section, a novel MLC based NOMA scheme is proposed and demonstrated in downlink 60-GHz RoF fronthaul networks to improve the system capacity and spectrum efficiency. The proposed MLC scheme can overcome the limitations imposed by traditional SPC/SIC based NOMA scheme, as no SIC operation is required at the receiver.

5.3.1 NOMA based on Conventional SPC and the Proposed MLC

Fig. 5.10 (a) depicts a 60-GHz RoF fronthaul network with one RRH serving two users in the small cell simultaneously. In the centralised BBU, baseband signals of a near user (NU) and a far user (FU) are multiplexed in power domain and allocated with significantly different electrical launched power. The photonic 60-GHz signals are generated in BBU before transmission over the RoF fronthaul link. Upon photo-detection at the RRH, 60-GHz radio signals are radiated into the air and received by the two users using 60 GHz horn antennas.

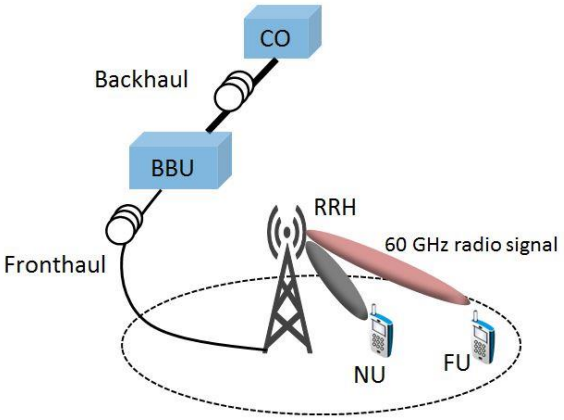

Fig. 5.10 60 GHz mm-wave RoF fronthaul serving two users in a small cell

Shown in Fig. 5.11 (a) is the principle of conventional superposition code (SPC) NOMA scheme and the composite constellation maps. In SPC NOMA scheme, bit streams of NU and FU are firstly modulated using 4 QAM modulation format independently. The resulted 4 QAM symbols (x_n for NU and x_f for FU) are linearly superposed with different power allocations,

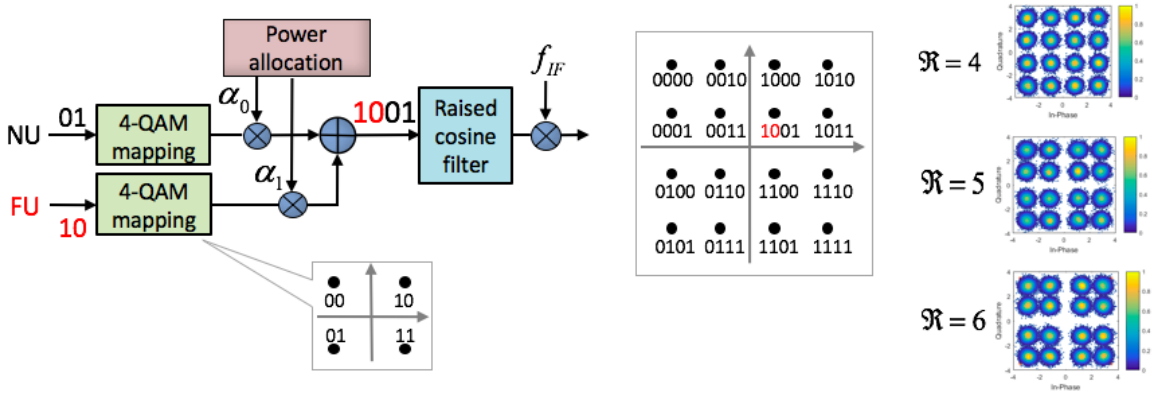

(a)

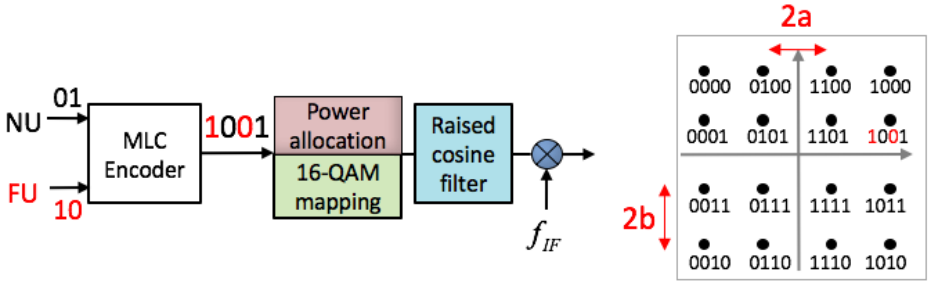

(b)

Fig. 5.11 (a) Principle of traditional NOMA based on SPC and (b) the proposed NOMA based on MLC. CO: central office, BBU: baseband unit, RRH: remote radio head, NU: near user, FU: far user

represented as $x_{Tx} = \sqrt{\alpha_0 P_T} x_n + \sqrt{\alpha_1 P_T} x_f$, where P_T is the total electrical launched power for two users and $\alpha_0 + \alpha_1 = 1$. The power allocation ratio, $\Re$, of SPC NOMA is defined as $\Re = \alpha_1 / \alpha_0$, where $\alpha_1 > \alpha_0$. As shown in Fig. 5.11 (a), since the 4-QAM modulation is mapped with Gray-coding, the composite constellation map cannot maintain Gray-code based mapping. At FU, single user detection is utilised and the receiver treats the NU signal as white noise. To implement successive interference cancellation (SIC) at NU, the FU signal has to be demodulated first. Secondly, the estimated FU signal is re-modulated and multiplied by the estimated channel response. The resulted signal will be subtracted from the received signal to achieve interference cancellation and to recover the signal of NU. In practice, receiver complexity is increased due to the implementation of SIC. Performance of NU is greatly degraded due to error propagation from the FU, especially at low power allocation ratios.

In order to solve the aforementioned practical issues, we propose an multi-level code (MLC) enabled NOMA scheme at the transmitter as shown in Fig. 5.11 (b). Instead of superposing QAM symbols of different users, the MLC scheme is conducted by bit interleaving and non-uniform QAM symbol mapping. As depicted in the composite constellation, the FU bit stream is interleaved at the first and third bits of the composite symbol to select the quadrant, while the NU bit stream is used to select the location of the symbol in the quadrant. The minimum distance between two composite symbols in different quadrants is $2a$, and the minimum distance between two composite symbols in the same quadrant is $2b$. Hence, the power allocation ratio in MLC scheme is defined as $\Re = (1+a/b)^2$. The total transmit power (P_T) of two users is maintained the same as in SPC scheme. Power allocation in MLC scheme is achieved by controlling the distances of the composite symbols. It should be noted that the composite constellation of MLC maintains Gray-mapping. Both NU and FU use single user detection, in which the received signals are firstly demodulated using the non-uniform 16-QAM demodulation. Then each user will only extract the bits at the corresponding locations in the received composite symbols to obtain the estimated bit streams. In contrast to SIC, this method enables low-complexity receiver. In addition, error propagation from the FU to NU can be eliminated as the signals of both users are demodulated independently. More generally, when more than two users are located in the cell, NOMA pair clustering will be deployed first in the BBU to pair a NU with a FU according to their channel quality.

5.3.2 Experimental Setup and Results

The proof-of-concept experimental setup is depicted in Fig. 5.12. The two-user 60 GHz RoF fronthaul system consists of four parts: centralised BBU, RRH, user equipment (UE) and a fronthaul link connecting the BBU and RRH. The principle of operation of the experimental setup in Fig. 5.12 is similar to that in CoMP fronthaul system shown in Fig. 5.3, except that only one fronthaul link is exploited here to serve two users in a small cell. The detailed explanation of the 60-GHz photonic signal generation will not be repeated here for simplicity. The generated 60.25-GHz optical signal was sent to the RRH over 3-km SMF fronthaul. At the RRH, a 60-GHz photodetector converted the optical signals to 60.25-GHz radio signals, which were sent to two users using a circular horn antenna with 25-dBi gain. The NU and FU were located at different distances away from the RRH. Each UE received the 60.25-GHz wireless

signals using separate 25-dBi horn antennas. We adjusted the antenna beam direction to emulate the line-of-sight property of 60-GHz wireless signals. In the experiment, 4-Gbps 4-QAM signals for NU and FU were transmitted simultaneously, obtaining a total bit rate of 8 Gbps. Fig. 5.12 inset (1) and (2) present the received IF signal spectra at distances of 38 cm and 250 cm. The signal amplitude attenuation was caused by the path loss of 60-GHz radio signals. Offline signal processing was conducted in MATLAB, including time synchronisation, channel estimation, frequency down-conversion, non-uniform 16-QAM demodulation and bit-error rate (BER) calculation.

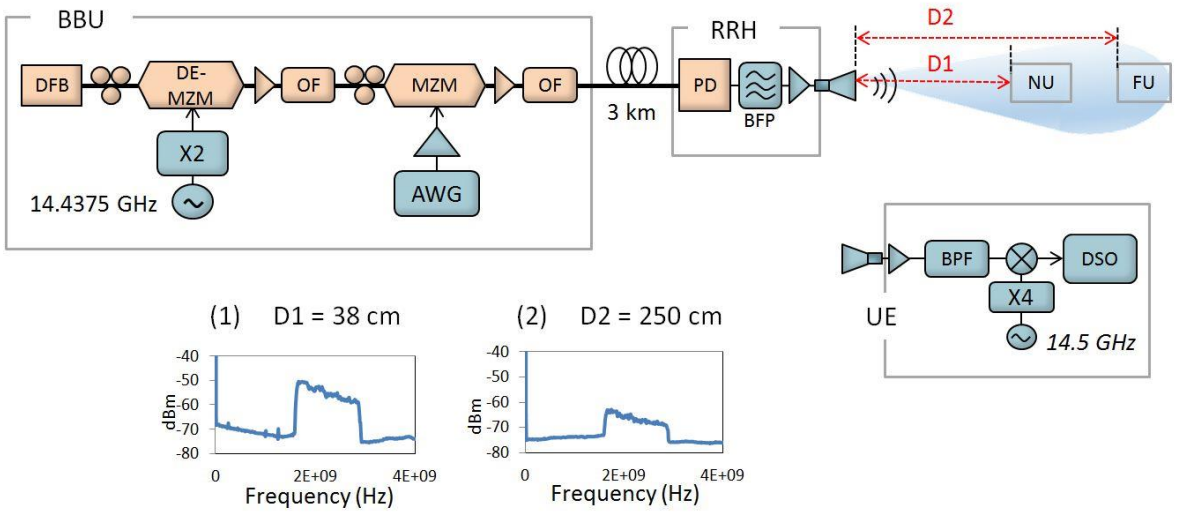

Fig. 5.12 Experimental setup of fronthaul link serving two users with NOMA scheme. Inset: RF spectrum of the down-converted signal at (1) near user with **D1 = 38cm** and (2) far user with **D2 = 250cm**. X2: frequency doubler, X4: frequency quadrupler, OF: optical filter

We first measured the BER versus received optical power at the RRH in Fig. 5.13 to quantify the performance of the overall link. The wireless distance was fixed at 38 cm and the power allocation ratio was $\Re = 4$ for NU and FU employing SPC and MLC schemes. MLC scheme performs better than SPC scheme with improved receiver sensitivity at the RRH. The improved optical receiver sensitivity enables lower power consumption at the RRH and has the potential of improving the cell coverage for 60 GHz small cells.

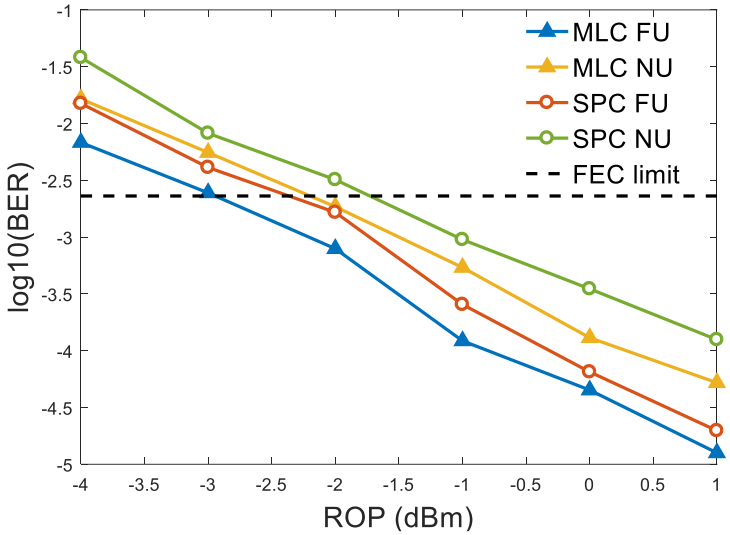

Fig. 5.13 BER versus received optical power (ROP) for SPC and MLC scheme at distance **D = 38cm** (FEC limit: $2.3\text{x}10^{-3}$ forward error correction limit with 7% overhead.)

We then evaluated the BER performances at various wireless link distances (NU and FU with distances of 38 cm, 90 cm, 147 cm, 198 cm and 250 cm) as depicted in Fig. 5.14 (a-e). The received optical power at the RRU was maintained at 1 dBm. The insets in Fig. 5.14 (a) present the received composite constellation maps at UE of MLC scheme at $\Re = 1, 4, 7$. Firstly, we compare the FU performance of the MLC without SIC scheme with the SPC-SIC scheme in Fig. 5.14 (a-e). When the FU moves from 38 cm to 250 cm, the performance of MLC scheme is better compared to the SPC-SIC scheme, especially at high power allocation ratios ($\Re \geq 4$). Similarly, the NU employing MLC outperforms SPC at all power allocation ratios. When power ratio is small ($\Re \leq 4$), a minimum BER exists for NU employing SPC-SIC scheme. In this scenario, the NU BER increases significantly with the decrease of power ratio even if the transmit power increases. This is mainly due to the error propagation from the FU at low power ratios. In contrast, error propagation can be completely avoided by using the MLC scheme. To implement the MLC NOMA scheme in a 60-GHz RoF fronthaul system, a higher power ratio will be chosen for a NOMA pair with distinct channel conditions (e.g. $\Re = 7$, NU D = 38cm, FU D = 250cm). While for a NOMA pair located close to each other, a low power ratio will be chosen (e.g. $\Re = 3$, NU D = 90cm, FU D = 147cm).

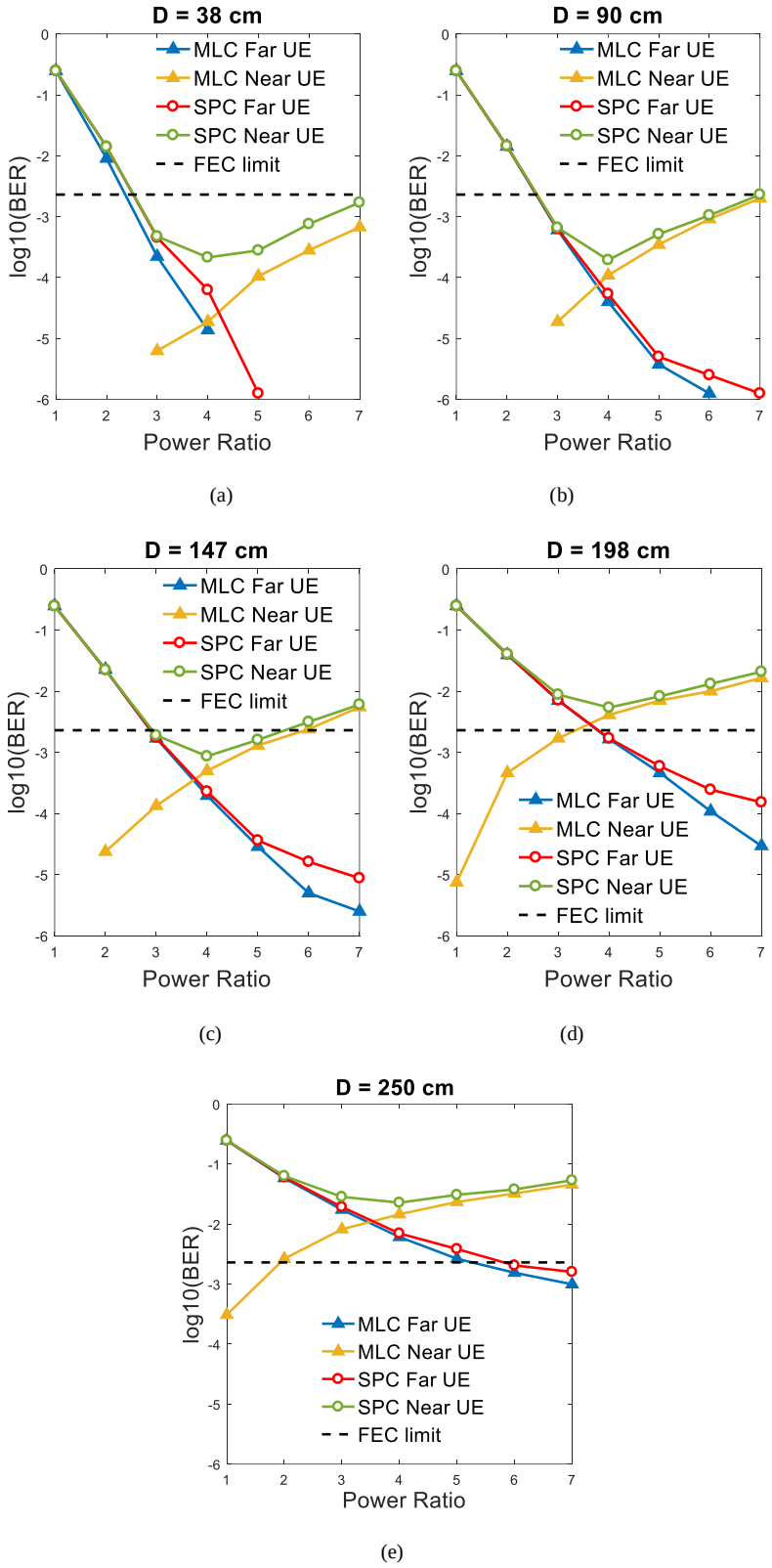

Fig. 5.14 BER versus power allocation ratio at varied wireless distances: (a) 38 cm, (b) 90 cm, (c) 147 cm, (d) 198 cm, (e) 250 cm

5.4 NOMA with Coordinated Base Stations

In the previous section, a single cell NOMA scheme aimed at improving the spectrum efficiency in the fronthaul system is proposed and demonstrated. When a user with lower channel gain (i.e. the far user in a NOMA user pair) is located at cell boundaries, inter-cell interference will also degrade the received signal quality apart from the intra-cell interference induced from power domain multiplexing. To mitigate the impact of inter-cell interference on the far users located at cell boundaries of two small cells, NOMA with coordinated base stations is adopted in the fronthaul system. In this section, we focus on a multi-user scenario shown in Fig. 5.15, where two small cells coordinated with each other using the CoMP transmission technique to serve the far user located at the cell boundaries. At the same time, NOMA technique is utilised between a pair of users located in the same cell.

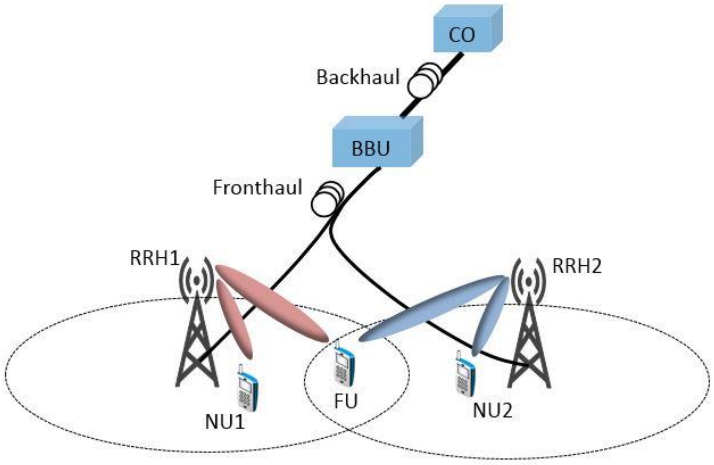

Fig. 5.15 Illustration of the downlink fronthaul RoF system using NOMA with coordinated base stations.

5.4.1 Principle of Operation for NOMA with Coordinated BSs

We will first discuss the principle of operation for the downlink fronthaul system using NOMA technique with coordinated BSs and demonstrate the applicability. Here we assume a downlink 2-user NOMA pair in each small cell, and the far user is in the cell boundary region for CoMP transmission as shown in Fig. 5.15.

- *SPC-based NOMA with Coordinated BSs*

Fig. 5.16 depicts the principle of operation for the SPC-based NOMA with coordinated BSs in downlink fronthaul systems serving one far user (FU) in the cell boundary and two near users (NU) in the cell centre. In the BBU, the data streams for NU1, NU2, and FU are first modulated using 4 QAM modulation format. The QAM symbols of FU is then coded with Alamouti code and two data streams are generated to be transmitted in two channels. In each channel, data symbols of NU will be multiplexed with the coded FU data symbols in power domain, resulting in composite 16 QAM signals. The power allocation ratio ($\Re = \alpha_1/\alpha_0$) between FU and NU in each cell is the same as defined in Section 5.3. Then the composite 16 QAM signals are passed through a raised cosine filter and up-converted to 2.5-GHz intermediate frequency (IF) in MATLAB. Finally, the generated IF signals will be modulated onto the 60-GHz optical carriers in the BBU and transmitted along two separate fronthaul links. At the FU receiver, the demodulation approach is similar to that in CoMP fronthaul system, except that noise induced by NU data will degrade the FU signal quality. While at the NU, SIC method will be used to demodulate the signal.

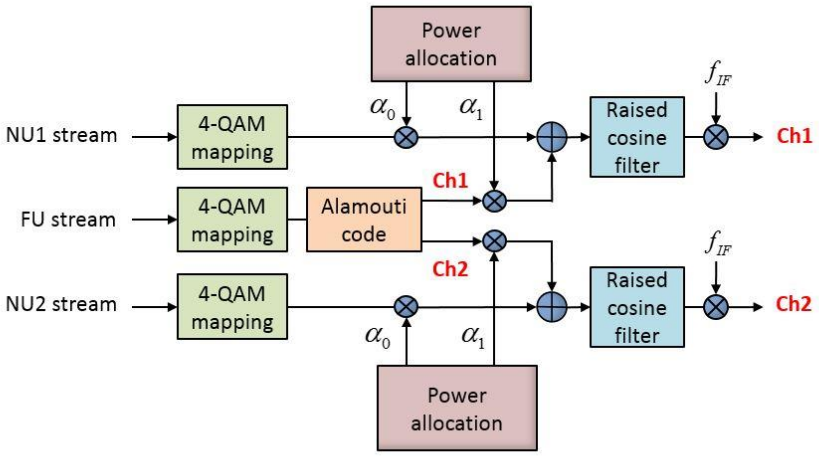

Fig. 5.16 Principle of operation of SPC-based NOMA with coordinated BSs

- *MLC-based NOMA scheme*

The operation principle of MLC-based NOMA scheme with coordinated BSs is illustrated in Fig. 5.17. Since the MLC scheme is achieved in bit level, the FU data stream will first be coded with Alamouti code after 4 QAM modulation and then demodulated to get the bit sequence for MLC coding. The following MLC-based NOMA scheme in two separate channels is the same as the single channel MLC NOMA scheme in Section 5.3.1 and will not be repeated here. The power allocation ratio is controlled by adjusting the distance between the composite symbols.

At the receiver, the FU demodulates the received signal using maximum likelihood detection and treat the NU data as noise. While the NUs demodulate the signals using MLC decode scheme which is independent of the FU signal.

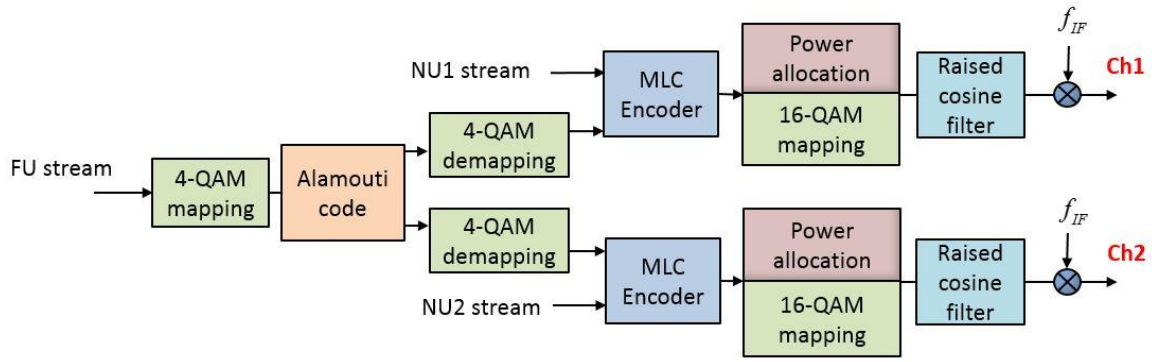

Fig. 5.17 Operation principle of MLC-based NOMA with coordinated BSs

5.4.2 Experimental Setup and Results

The SPC-based and MLC-based NOMA with coordinated BSs are experimentally demonstrated in the downlink fronthaul system to confirm the feasibility of the proposed schemes. The performance improvement of MLC-NOMA with CoMP is verified by comparing its performance with SPC-NOMA with CoMP.

The experimental setup for the fronthaul system using NOMA with coordinated BSs is shown in Fig. 5.18 (a). The experimental setup is similar to that in CoMP fronthaul system shown in Fig. 5.3, except that three users at different locations are served using the coordinated RRHs. As a proof-of-concept demonstration, the locations and orientations of the transmit and receive antennas are fixed and depicted in Fig. 5.18 (b). Distance between the two transmitters is kept

as the optimum distance of 40 cm according to the experimental charactersisation results in Section 5.2.4.4. The distance between transmitter and FU (resp. NU) is 124 cm (resp. 60 cm).

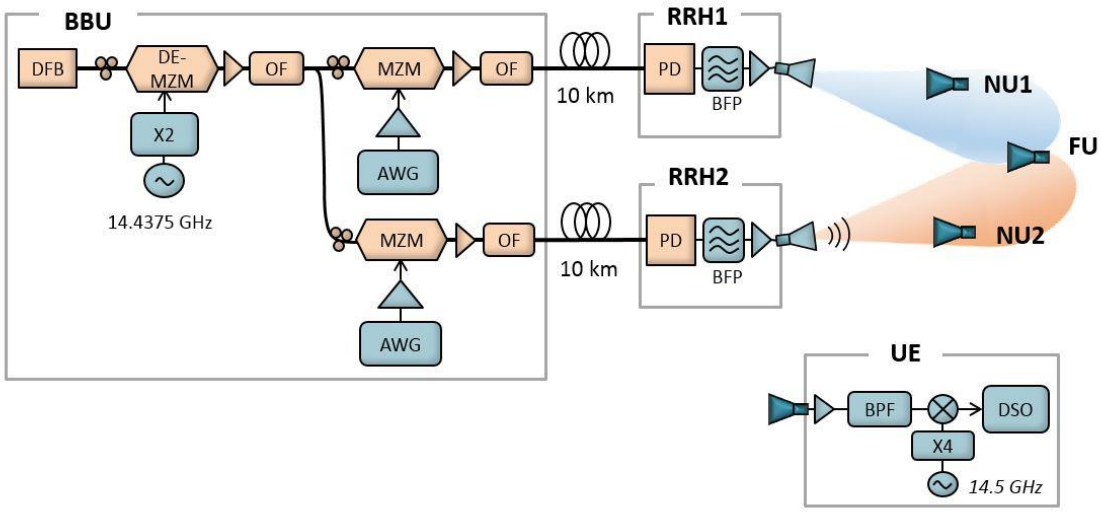

(a)

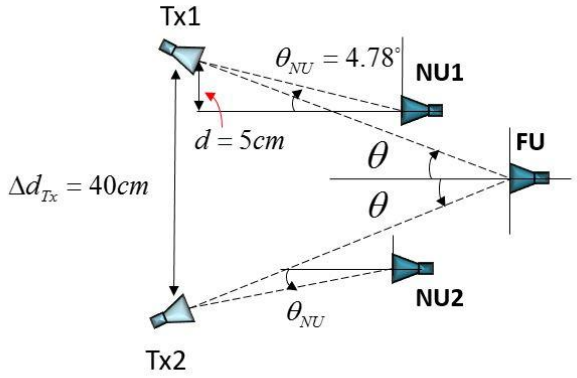

(b)

Fig. 5.18 (a) Experimental setup of downlink fronthaul system using NOMA with coordinated BSs serving two near users and one far user located at the cell boundaries. (b) Orientation of transmit antennas and receive antennas.

The data rate is set to 2 Gbps for each user. Thus, a sum rate of 6 Gbps was achieved in the system. Fig. 5.19 shows the calculated BER versus power allocation ratio for the fronthaul system serving two NUs and one FU. The launched optical power at the RRHs are maintained as -3 dBm for both links for fair comparison. The system performance of three users, using the two NOMA schemes with coordinated BSs, is compared for 10-km fronthaul transmission. In Fig. 5.19, the solid line represents the measured BER for users employing MLC-NOMA with

CoMP function. While the dashed line represents measured BER for users employing SPC-NOMA with CoMP function. It is noted that the BER performance of the three users exploiting MLC-NOMA with CoMP scheme is improved compared with SPC-NOMA with CoMP function especially at higher power allocation ratio values ($\Re \geq 4$). In addition, error propagation from the FU to NU is completely avoided at low power allocation values ($\Re \leq 4$). This performance improvement is due to the employment of MLC scheme in NOMA technique as we have demonstrated in Section 5.3. The valid power allocation ratio in the fronthaul system is defined as the range of which BER value is below the FEC limit. For the MLC-based NOMA with CoMP scheme, the valid power allocation range is $3 \leq \Re \leq 5$. However, the range of SPC-based NOMA with CoMP scheme is $3.5 \leq \Re \leq 4.2$. Therefore, the better performance of MLC-based scheme makes it more flexible and robust for NOMA user pair clustering, as well as higher data rate and longer distance transmission. The employment of CoMP function in the fronthaul system offers diversity gain for the FU located at cell boundaries of two small cell which has been verified in Section 5.2.4.2.

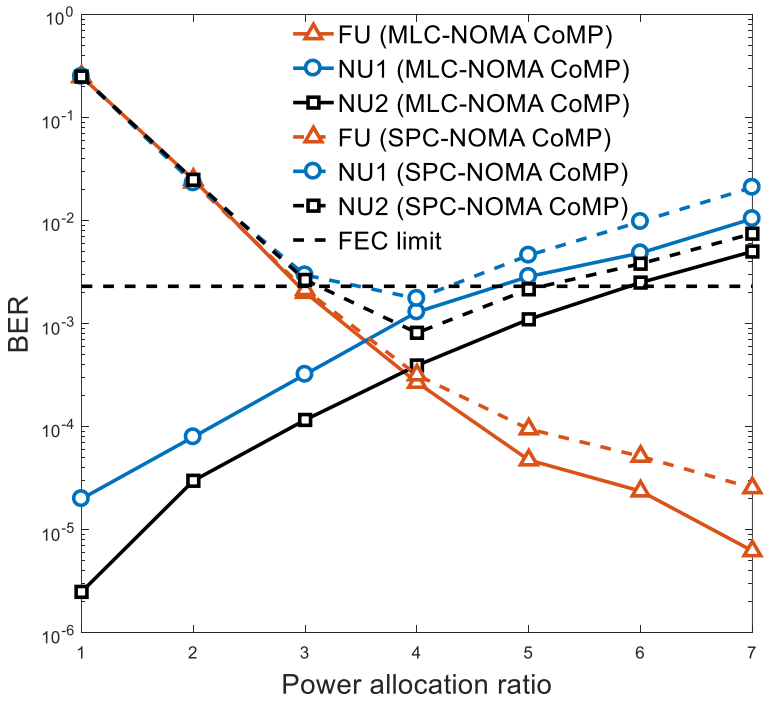

Fig. 5.19 BER versus power allocation ratio for the fronthaul system using MLC-based NOMA with coordinated BSs and SPC-based NOMA with coordinated BSs

5.5 Summary

In this chapter, we have proposed and experimentally demonstrated a 60-GHz RoF fronthaul network with two advanced techniques, namely CoMP and NOMA, overcoming the data rate and coverage bottlenecks imposed by existing 60-GHz mm-wave RoF systems.

Firstly, the fronthaul link employing CoMP transmission was demonstrated, serving one user located at the cell boundaries of two small cells. The proposed architecture has the merits of simplified CFOs estimation at receiver, reduced signalling overhead in the backhaul of high-speed next generation mobile networks. Besides, in this configuration, much smaller delay can be achieved and is able to meet the latency requirement of the next generation wireless communication system. The demonstrated CoMP fronthaul network achieved an improvement of 1.3 dB in receiver sensitivity for 4-Gbps 4-QAM signal transmitting along a 10-km fibre fronthaul compared to the scenario of two fronthaul links simultaneously transmission without STBC. This diversity gain is exploited to increase the achievable data rate of cell-edge user and to extend the mm-wave small cell coverage. Impact of imperfect synchronisation between two coordinated channels has also been evaluated. CoMP-based 60-GHz fronthaul links were confirmed to be more robust against inter-symbol interference (ISI) caused by timing misalignment than two channels transmission without STBC. The system performance was also characterised with regard to impact of signal angle of arrival, distance between two transmitters, the range of reception area, and sensitivity to antennas angle misalignment. These system characterisations provide a practical and thorough reference for future 60-GHz CoMP fronthaul link design.

Secondly, a two-user 60-GHz RoF fronthaul using MLC-based NOMA scheme was demonstrated experimentally, where no SIC was needed at the receiver. A total rate of 8 Gbps was achieved using 4 QAM signals transmitting over 3-km fibre fronthaul and 2.5-m wireless link. The proposed MLC-based NOMA scheme can overcome the practical issues faced by conventional SPC-based NOMA scheme which uses Gray-mapping for the composite constellation, has no error propagation from the far user, potentially lower the complexity of the receiver and increasing the cell coverage.

Finally, a multi-cell NOMA scheme was experimentally demonstrated together with CoMP function for the first time. The benefits include mitigated impact of inter-cell interference on the far users located at cell boundaries of two small cells, as well as improved spectrum efficiency of the system. In addition, the increased range of power allocation ratio in the MLC-NOMA transmission with CoMP function enables more flexible user clustering design at the transmitter.

Chapter 6 Analytical Modeling of Fronthaul Networks based on CoMP and NOMA

6.1 Introduction

Current cellular networks are undergoing an evolutionary change to a network that can provide higher traffic volume, larger numbers of connected users and smaller latency. Coordinated multipoint (CoMP) transmission [85, 95, 163], that can eliminate inter-cell interference and improve cell edge user performance, has been regarded as a potential enabler for next generation cellular networks. In the downlink RoF fronthaul networks, the employment of CoMP transmission requires that the same channel (time and frequency resources) is allocated to the user located at the cell edge of two small cells. Hence, the spectral efficiency is greatly degraded due to the use of CoMP transmission, especially when the number of cell edge users increases. Considering the large number of connected users and finite time/frequency resources in the next generation cellular networks, spectral efficiency is envisioned to be high to cater for the seamless coverage of user. Among numerous potential technologies to realise 5G and beyond, non-orthogonal multiple access (NOMA) has been introduced to increase the spectral efficiency by multiplexing multiple users' information in power [102] or code domain [107]. Hence, the deployment of CoMP and NOMA techniques in the fronthaul networks supplement each other to provide both improved signal quality of the cell edge user and acceptable spectral efficiency of the system.

There are previous studies and investigations in the literature on the combination of NOMA and CoMP techniques [126, 164-167]. However, to the best of our knowledge, there is a lack of investigation of NOMA applications in a coordinated context in the 60-GHz RoF fronthaul networks. In Chapter 5, we have experimentally demonstrated a 60-GHz RoF fronthaul system serving three users using NOMA techniques with coordinated BSs. In this chapter, we derive an analytical model of the fronthaul system based on NOMA and CoMP transmission. The mathematical expressions of effective signal-to-inteference-plus-noise ratio (SINR) of edge

user and near user are derived, as well as the spectral efficiency of a small cell using NOMA with coordinated BSs.

NOMA has been introduced in analog fronthaul transmission system to satisfy the large number of connected users with improved capacity in the next generation communication networks [115, 128, 157, 168-170]. However, there is a lack of comprehensive investigation to analyse the NOMA-based fronthaul system performance in the context of stochastic demography distribution in the millimetre-wave (mm-wave) small cells. In addition, a study on the impact of 60-GHz wireless channels and the noise induced from photonic links have not been considered. Hence, in this chapter we extend the model of fronthaul systems employing NOMA technique to a general case considering random number of users in a small cell, different user equipment (UE) distributions and various NOMA clustering schemes.

This chapter is organised as follows: in Section 6.2 we develop a tractable model for RoF fronthaul based on NOMA with coordinated BSs, where two small cells serving one edge user using CoMP transmission and two near users within the cell using NOMA technique. Three user distributions schemes and two NOMA clustering schemes are presented in Section 6.3. In Section 6.4 theoretical investigations of downlink NOMA fronthaul system are demonstrated, including the closed-form expressions of cell throughput containing random number of users and different NOMA clustering schemes. The optimum power allocation ratio to achieve maximum cell throughput in the cell is derived in Section 6.5. Finally, the simulation results and discussions are presented in Section 6.6, including a comparison of cell average spectral efficiency of NOMA and orthogonal multiple access (OMA) fronthaul systems.

6.2 Analytical Model of NOMA with Coordinated BSs in Fronthaul Networks

The experimental setup and results of NOMA with coordinated BSs in the fronthaul networks have been demonstrated and discussed in Chapter 5. In this section, a generalised analytical model of the proposed system using NOMA with coordinated BSs will be derived to analyse the underlying principle using average capacity of the near and far users in the cell. The

employment of NOMA with coordinated BSs in the fronthaul links has the merits of improved cell edge throughput and coverage, and improved spectral efficiency.

For the user located at the cell boundaries of two small cells, two BSs will transmit signals coordinately using Alamouti code to achieve transmit diversity gain and to eliminate the inter-cell interference. While within each cell, a near user will be served using the same frequency and time resources as the far user using NOMA technique. The system model is shown in Fig. 6.1. The transmitted baseband symbols for the cell edge user (UE1) are: $\{x_1, x_2, ..., x_N\}$. Let x_{ij} denotes the baseband symbols transmitted from the j_{th} RRH to the i_{th} UE, where $i \in \{1,2,3\}$ and $j \in \{1,2\}$. After using Alamouti coding scheme, the symbols transmitted to UE1 from RRH1 and RRH2 are: $x_{11}:\{x_1, -x_2^*, ..., x_{n-1}, -x_n^*\}$ and $x_{12}:\{x_2, x_1^*, ..., x_n, x_{n-1}^*\}$. At the same time, the symbols transmitted from RRH1 to UE2 (resp. RRH2 to UE3) are x_{21} (resp. x_{32}). Here we consider a symmetrical case where the distances from the RRH to the near user are the same in two small cells. Hence, the power allocation ratios are the same and denoted as $\Re = \alpha_1/\alpha_0$, where $\alpha_0 + \alpha_1 = 1$ and $\alpha_1 > \alpha_0$. Therefore, the transmitted signal from RRH1 and RRH2 are given by

$$\begin{cases} x_{RRH1} = \sqrt{\alpha_1 P_T}\, x_{11} + \sqrt{\alpha_0 P_T}\, x_{21} \\ x_{RRH2} = \sqrt{\alpha_1 P_T}\, x_{12} + \sqrt{\alpha_0 P_T}\, x_{32} \end{cases} \quad (1)$$

where P_T is the power budget for two users in the same cell.

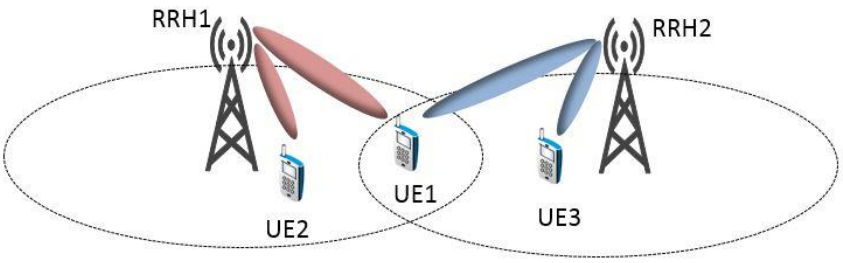

Fig. 6.1 Illustration of two cells using NOMA technique with coordinated RRHs

Let h_{ij} denotes the channel coefficients from j_{th} RRH to the i_{th} UE, w_{ij} denotes the precoding matrix coefficients, and PL_{ij} denotes the path loss from j_{th} RRH to the i_{th} UE. The received signals at cell edge user can be represented as

$$y_1 = h_{11}w_{11}\sqrt{\frac{\alpha_1 G_t G_r P_T}{PL_{11}}}x_{11} + h_{12}w_{12}\sqrt{\frac{\alpha_1 G_t G_r P_T}{PL_{12}}}x_{12} + h_{11}w_{21}\sqrt{\frac{\alpha_0 G_t G_r P_T}{PL_{11}}}x_{21} + h_{12}w_{32}\sqrt{\frac{\alpha_0 G_t G_r P_T}{PL_{12}}}x_{32} + n_1 \quad (2)$$

The first two terms in (2) represent the desired signal while the other terms are interference from the near users and the system noise. After mathematical manipulation, the received signal of the edge user at the first and second time slot can be expressed as

$$\begin{bmatrix} y_1(1) \\ y_1(2) \end{bmatrix} = H\begin{bmatrix} x_1 \\ x_2 \end{bmatrix} + \begin{bmatrix} N_1(1) \\ N_1^*(2) \end{bmatrix} \quad (3)$$

where $H = \begin{bmatrix} \frac{h_{11}\omega_{11}\sqrt{\alpha_1 G_t G_r P_T}}{\sqrt{PL_{11}}} & \frac{h_{12}\omega_{12}\sqrt{\alpha_1 G_t G_r P_T}}{\sqrt{PL_{12}}} \\ \frac{h_{12}^*\omega_{12}^*\sqrt{\alpha_1 G_t G_r P_T}}{\sqrt{PL_{12}}} & -\frac{h_{11}^*\omega_{11}^*\sqrt{\alpha_1 G_t G_r P_T}}{\sqrt{PL_{11}}} \end{bmatrix}$ denotes the channel matrix and N_1 is composed of interference and noise. The estimated signal of edge user in two time slots is therefore given by

$$\begin{bmatrix} \hat{x}_1 \\ \hat{x}_2 \end{bmatrix} = (H^H H)^{-1} H^H \begin{bmatrix} y_1(1) \\ y_1^*(2) \end{bmatrix} \quad (4)$$

Since the two near users are symmetrically located in the two cells, only UE2 are considered. The received signal at UE2 is expressed as

$$y_2 = h_{21}w_{21}\sqrt{\frac{\alpha_0 G_t G_r P_T}{PL_{21}}}x_{21} + h_{21}w_{11}\sqrt{\frac{\alpha_1 G_t G_r P_T}{PL_{21}}}x_{11} + h_{22}w_{12}\sqrt{\frac{\alpha_1 G_t G_r P_T}{PL_{22}}}x_{12} + h_{22}w_{32}\sqrt{\frac{\alpha_0 G_t G_r P_T}{PL_{22}}}x_{32} + n_2 \quad (5)$$

At the near users, if successive interference cancelation (SIC) is applied and we have the estimated received signal represented as

$$\begin{aligned}\hat{y}_2 &= y_2 - h_{21}w_{11}\sqrt{\frac{\alpha_1 P_T}{PL_{21}}}\hat{x}_{11} - h_{22}w_{12}\sqrt{\frac{\alpha_1 P_T}{PL_{22}}}\hat{x}_{12} \\ &\approx h_{21}w_{21}\sqrt{\frac{\alpha_0 P_T}{PL_{21}}}x_{21} + h_{22}w_{32}\sqrt{\frac{\alpha_0 P_T}{PL_{22}}}x_{32} + n_2\end{aligned} \tag{6}$$

In (6), the estimation of the edge user information is assumed to be correct without errors, which will not be true when the power allocation ratio is small.

However, our proposed MLC-based NOMA scheme (as mentioned in Chapter 5) can avoid the error propagation from the edge user to the near user as the signals of the two users are demodulated independently. Therefore, from (2) and (5), the SINR of the edge user (UE1) and near user (UE2) can be expressed as

$$\begin{cases} SINR_1 = \dfrac{\left|h_{11}w_{11}\sqrt{\alpha_1 P_T / PL_{11}}\right|^2 + \left|h_{12}w_{12}\sqrt{\alpha_1 P_T / PL_{12}}\right|^2}{\left|h_{11}w_{21}\sqrt{\alpha_0 P_T / PL_{11}}\right|^2 + \left|h_{12}w_{32}\sqrt{\alpha_0 P_T / PL_{12}}\right|^2 + \sigma^2} \\ SINR_2 \approx \dfrac{\left|h_{21}w_{21}\sqrt{\alpha_0 P_T / PL_{21}}\right|^2}{\left|h_{22}w_{32}\sqrt{\alpha_0 P_T / PL_{22}}\right|^2 + \sigma^2} \end{cases} \tag{7}$$

where σ^2 is the noise variance of the received signals. According to current 3GPP/ITU model [30], the line-of-sight (LOS) probability for signals with frequency above 6 GHz is

$$p = \min\left(\frac{20}{d}, 1\right)\left(1 - e^{-\frac{d}{39}}\right) + e^{-\frac{d}{39}} \tag{8}$$

where d is the distance from the RRH antenna to the UE. Thus, considering the LOS probability of 60-GHz channels, the achievable spectral efficiencies of UE1, UE2 and per-cell spectral efficiency are given by

$$\begin{cases} SE_1 = p_{11}^2 \log_2(1 + SINR_1) + 2p_{11}(1 - p_{11})\log_2(1 + SINR_{11}) \\ SE_2 = p_{21}\log_2(1 + SINR_2) \\ SE_{cell} = SE_2 + SE_1/2 \end{cases} \tag{9}$$

where p_{ij} is the LOS probability of the wireless channel from the j_{th} RRH to the i_{th} UE, and $SINR_{11} = \frac{\left|h_{11}w_{11}\sqrt{\alpha_1 P_T / PL_{11}}\right|^2}{\left|h_{11}w_{21}\sqrt{\alpha_0 P_T / PL_{11}}\right|^2 + \sigma^2}$ denotes the SINR of UE1 where only one of the coordinated links is a LOS channel.

6.3 NOMA User Pair Clustering

The key feature of NOMA is the non-orthogonal multiplexing of multiple users' information in the power domain. The performance benefits of users in the NOMA clustering pair largely depend on the power allocated to each user, which is determined by the user channel gain or user distributions. Hence, the NOMA user clustering approaches should be investigated considering various user distributions in the small cells. In this section, NOMA clustering schemes will be discussed and analysed under three cases of user distribution in the cells, including users clustering to the cell centre, clustering to the edge and uniform user distribution in the cell.

6.3.1 User Distributions

Generally, uniform user distribution is adopted in evaluating the cellular system performance for simplicity [171]. However, non-uniform user distribution is beneficial to provide a more accurate emulation of user locations in different topography of the land, thus more realistic illustration of system performance. In a small cell, users tend to cluster to the centre or the cell boundaries according to the physical topography of the land. For example, at street corner where the RRHs are deployed on top of buildings and pedestrians are clustering to the cell edge along the street. While in hotpots, higher density of users exists in the cell centre. Therefore, three user distributions in the NOMA fronthaul system will be considered and demonstrated, including two non-uniform user distributions and a uniform user distribution.

In uniform user distribution, users have an equal probability of locating in all possible locations in the cell. In contrast, for non-uniform distribution, the probability is different at different locations. Hence, we focus on the approach to generate different probabilities of user locations within a small cell in order to generate non-uniform user distributions. Here a spatial binning

method [172] is considered as shown in Fig. 6.2. In Fig. 6.2, the RRH is located at the centre of a small cell that is divided into N bins. The cell diameter is denoted as D. The probability of a user located in the i_{th} bin is defined as P_i ($i = 1, \ldots, N$), which is determined by the distance from the RRH to the centre of the bin r_i.

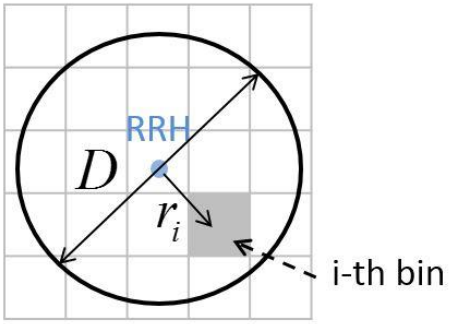

Fig. 6.2 Quantised representation of a small cell using a spatial binning method

In [172, 173] the probability density function (PDF) of non-uniform user distributions are expressed as a discrete function of the distance r_i, where the users located at the bins on the cell boundaries require special consideration. Here we further extend the models to a more general expression as a continuous function. The PDFs of user clustering to the centre and clustering to the edge are given by

$$P_C(r) = \frac{(D-2r)^2\beta + D^2}{\iint[(D-2r)^2\beta + D^2]dA} = \frac{24[\beta(D-2r)^2 + D^2]}{\pi D^4(\beta+6)}$$
$$P_E(r) = \frac{4r^2\beta + D^2}{\iint(4r^2\beta + D^2)dA} = \frac{8(D^2 + 4\beta r^2)}{\pi D^4(\beta+2)} \quad (10)$$

where r is the distance from the RRH to the user location, β ($\beta \geq 0$) is the scaling factor to control the strength of user clustering. The larger value of β, the more users will cluster to the cell centre or cell edge. Noted that when $\beta = 0$, all the locations have the same probability for user occurrence. Therefore, the PDF of uniform user distribution in the cell is expressed as

$$P_U(r) = \frac{4}{\pi D^2} \tag{11}$$

To generate the set of user locations with various distributions, the cumulative density function (CDF) is needed. The CDF of users clustering to the centre, clustering to the edge and uniform distribution are given by

$$\begin{aligned} CDF_C(r) &= \int_0^{2\pi} d\theta \int_0^{D/2} rP_C(r)dr = \frac{24(\beta+1)D^2r^2 - 64\beta Dr^3 + 48\beta r^4}{D^4(\beta+6)} \\ CDF_E(r) &= \int_0^{2\pi} d\theta \int_0^{D/2} rP_E(r)dr = \frac{8r^2(D^2+2\beta r^2)}{D^4(\beta+2)} \\ CDF_U(r) &= \int_0^{2\pi} d\theta \int_0^{D/2} rP_U(r)dr = \frac{4r^2}{D^2} \end{aligned} \tag{12}$$

In Fig. 6.3 the PDF and CDF as a function of the distance from RRH to the UE are illustrated to show the difference between the three distributions. The small cell diameter and scaling factor are chosen to be $D = 220\text{m}$ and $\beta = 10$ as an example.

A set of M user locations in the cell can be generated by sampling the CDF with M uniformly distributed numbers between 0 and 1. Then map the M numbers to the distance (x axis) in Fig. 6.3 to get the M user locations. Once the locations of users are determined in the small cell, NOMA user pair clustering will be investigated to group users with different channel gain (i.e. locations) into pairs for non-orthogonal multiplexing.

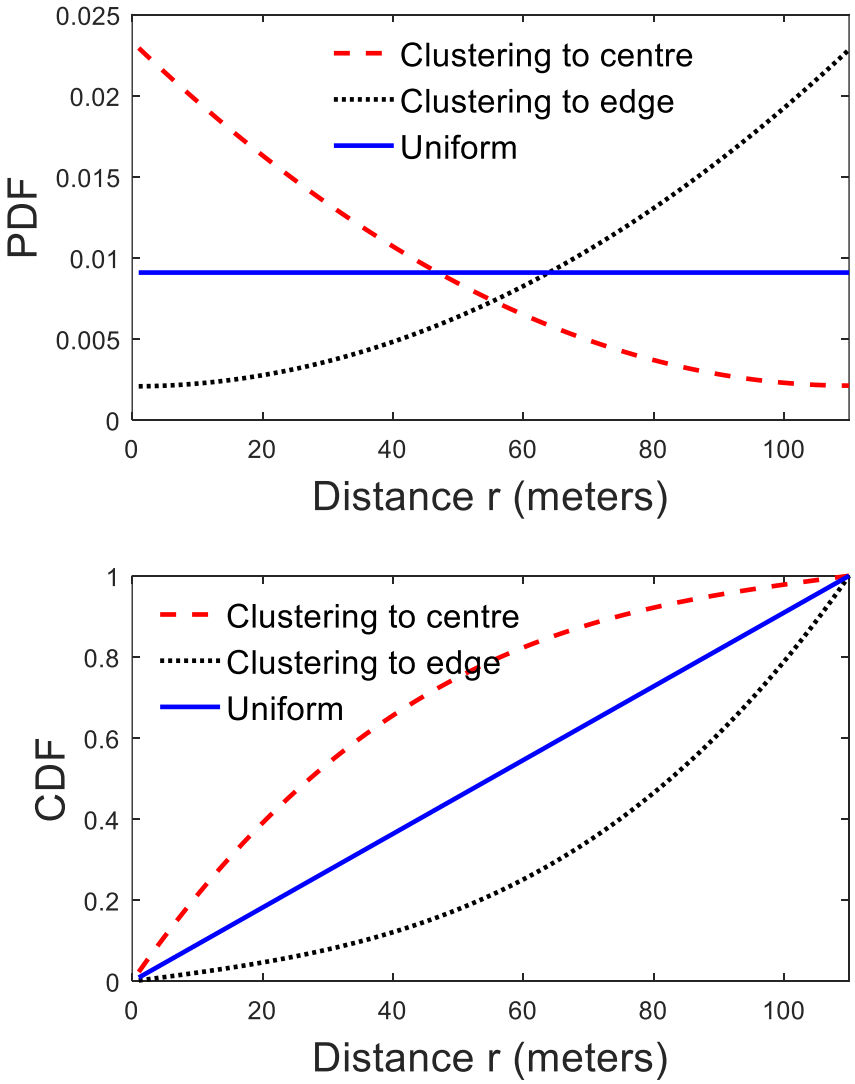

Fig. 6.3 PDF and CDF as a function of distance in three distributions

6.3.2 NOMA Clustering Scheme

Optimal NOMA user clustering for throughput maximisation can be achieved by exhaustive search among all the users in the same cell. In this case, all the possible combinations of NOMA user pair need to be considered for every user. The computational complexity is greatly increased especially for cells with large numbers of users. Some research has been done to

decrease the complexity by using sub-optimal user clustering schemes that exploit the differences of user channel gain [119, 171, 174].

Before grouping users into NOMA clusters, the number of users in a cluster should be decided. The more users in the same cluster, the more complex receiver will be for the users with higher channel gain. In addition, the latency for users with higher channel gain will increase due to the computational complexity. Considering the low-latency and low-cost requirements of next generation wireless communication systems, the number of users in a NOMA cluster is limited. Thus, we only consider a 2-user NOMA cluster using sub-optimal user clustering schemes in the following analysis.

Taking the transmit and receive antenna gain and path loss of 60-GHz wireless signals into account, the channel gain of k_{th} user is defined as

$$G_k = \frac{G_t G_r}{PL_k} \tag{13}$$

where G_t and G_r are the gains of the transmit and receive antennas to overcome the large path loss and PL_k is the path loss of k-th user. As mentioned earlier, 60-GHz wireless signals have the characteristics of line-of-sight (LOS) transmission. Thus, a Friss' free space path loss (FSPL) model [33, 175] can be used to describe the path loss effect as a function of transmission distance. The path loss model in dB for a user located at a distance r is given by

$$PL(f,r)[dB] = 20\log_{10}(\frac{4\pi f}{c}) + 10n\log_{10}(r) + \chi_\delta \tag{14}$$

where the first term on the right denotes the free space path loss in dB at 1 m, f is the carrier frequency in Hertz in the 60 GHz frequency band, n is the path loss exponent which describes how lossy the environment is. χ_δ is the shadowing variable with zero mean and standard deviation of σ. The path loss of the k_{th} user in the cell in linear scale is expressed as

$$PL_k(f,r_k) = (\frac{4\pi f}{c})^2 \cdot r_k^{\,n} \cdot 10^{\chi_\delta/10} \tag{15}$$

Assume there are M users located within the cell, we first sort the users according to their channel gain G_k, where $1 \leq k \leq M$. All the users are sorted in descending order so that the first user has the highest channel gain G_1, while the M-th user has the lowest channel gain: $G_1 \geq G_2 \geq \cdots \geq G_k \geq \cdots \geq G_M$. Since the users are supposed to be grouped into 2-user clusters, all the users are classified into two or three classes depending on whether M is an even or odd number as shown in Fig. 6.4. If M is an even number, the users will be divided into two groups, near users in class A and far users in class B, according to their channel gain. While for an odd number M, the user with channel gain of $G_{(M+1)/2}$ will be excluded as a non-NOMA user.

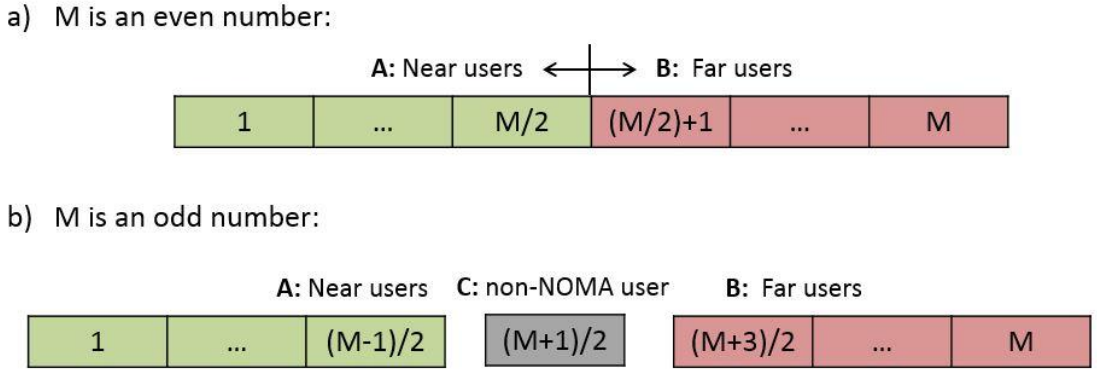

Fig. 6.4 Classify M users into near and far user groups

If the power allocation ratio $\Re$ (stated as the ratio for simplicity in the following analysis) is kept the same for all the NOMA clusters within the same cell, any user in class A can be clustered with a user in class B, without any influence on the throughput performance. However, if the ratio is dynamically determined in each cluster aimed at maximising the throughput of each cluster thus the throughput of the cell, higher cell capacity is expected compared with the fixed ratio scheme. Besides, it should be noted that dynamic ratio in each cluster has higher computational complexity. Two clustering schemes [171] are considered in the dynamic ratio scheme. In Fig. 6.5, the two clustering schemes are illustrated where the number of users are chosen to be 6 as an example. Each user in the near user class A will be paired with a user in the far user class B. In clustering scheme 1, the near user with highest channel gain in class A will be paired with the far user with highest channel gain in class B. While in clustering scheme

2, the near user with highest channel gain in class A will be paired with the far user with lowest channel gain in class B.

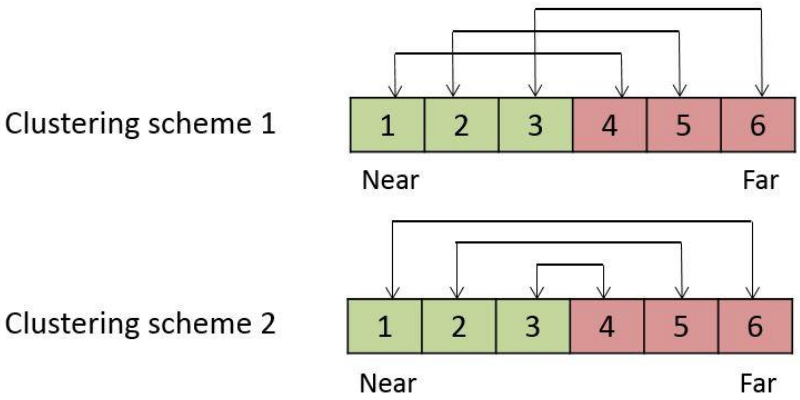

Fig. 6.5 Illustration of two clustering scheme for 2-user NOMA cluster

6.4 Downlink NOMA Fronthaul System Model

User distributions and NOMA clustering schemes for 60-GHz fronthaul networks have been discussed in section 6.3. In this section, a 2-user NOMA fronthaul system model will be derived and the closed-form expression of cell throughput in a 60-GHz small cell will be given, where both fixed ratio over the entire cell and dynamic ratio will be considered. Particularly, the noise from the photonic link is considered in the derived analytical model, resulting in a more precise model for the proposed fronthaul system.

6.4.1 System Model

For a downlink fronthaul network employing NOMA technique, single transmit antenna and single receive antenna for both RRH and UE are considered. The number of users in the cell is M. NOMA technique is achieved by grouping a near user and a far user into a cluster. The transmit power budget for a 2-user NOMA cluster is $P_T = P_n + P_f$, where P_n is the transmit power allocated to the near user and P_f is the power allocated to the far user. Hence, the power

allocation ratio is denoted as $\Re = P_f/P_n$. For the non-NOMA user in the case when M is an odd number, the transmit power budget is $P_T/2$. The 60-GHz signal to be transmitted at the RRH antenna contains noise originated from the optical fronthaul transmission and should be considered in the model for more accurate analysis. The noise power is represented as N_{Tx}. Thus, the signal-to-noise ratio (SNR) at the RRH is given by

$$SNR_{Tx} = \frac{P_T}{N_{Tx}} = \frac{P_n + P_f}{N_{Tx}} \tag{16}$$

The signal-to-interference-plus-noise ratio (SINR) for the near user and far user at the transmitter is represented as

$$\begin{cases} SINR_{Tx\_n} = \dfrac{P_n}{N_{Tx}} \\ SINR_{Tx\_f} = \dfrac{P_f}{P_n + N_{Tx}} \end{cases} \tag{17}$$

After simplification, (17) can be expressed using the SNR at the transmitter as

$$\begin{cases} SINR_{Tx\_n} = \dfrac{SNR_{Tx}}{\Re + 1} \\ SINR_{Tx\_f} = \dfrac{\Re \cdot SNR_{Tx}}{\Re + SNR_{Tx} + 1} \end{cases} \tag{18}$$

At the receiver, the received power of k_{th} user contains the power of a near and a far user in the cluster and is expressed as

$$P_{rk} = P_{nk} + P_{fk} = P_T G_k = G_k P_n + G_k P_f \tag{19}$$

where P_{rk} is the total received power, P_{nk} is the power of the near user, P_{fk} is the power of the far user, and G_k is the channel gain of the k_{th} user as denoted in (13) which is a function of the distance between the RRH and the user. Therefore, the received power is determined by the channel gain and thus the location of the user. Let N_k be the power of Gaussian noise at the receiver, the SNR at k_{th} receiver is then given by

$$SNR_k = \frac{P_{rk}}{N_k + G_k N_{Tx}} = \frac{P_T G_k}{N_k + G_k N_{Tx}} = \frac{P_T G_k SNR_{Tx}}{N_k SNR_{Tx} + G_k P_T} \tag{20}$$

To analyse the performance of the near and far users, SINR at the receiver needs to be defined. If the k_{th} user is sorted into the far user class, the power of near user contributes to the inter-cell interference to the far user. Hence, the SINR of a far user is

$$SINR_{fk} = \frac{P_{fk}}{P_{nk} + N_k + G_k N_{Tx}} \tag{21}$$

If the k_{th} user is sorted into the near user class, the inter-cell interference from the far user can be eliminated using our proposed MLC-based NOMA scheme as mentioned in Chapter 5. Therefore, the SINR of a near user is expressed as

$$SINR_{nk} = \frac{P_{nk}}{N_k + G_k N_{Tx}} \tag{22}$$

Combined with the definition in (20), (21) and (22) can be represented using the ratio and SNR_k as

$$\begin{cases} SINR_{fk} = \dfrac{\Re \cdot SNR_k}{\Re + SNR_k + 1} \\ SINR_{nk} = \dfrac{SNR_k}{\Re + 1} \end{cases} \tag{23}$$

For the non-NOMA user, the received power is given by $P_{rk} = P_T G_k/2$, ($k = (M+1)/2$). Therefore, the SNR of the non-NOMA user is represented by

$$SNR_0 = \frac{P_{r0}}{N_0 + G_0 N_{Tx}} = \frac{P_T G_0}{2(N_0 + G_0 N_{Tx})} \quad , \quad k = \frac{(M+1)}{2} \tag{24}$$

The achievable throughput per bandwidth, i.e. spectral efficiency, for the k_{th} user in the 2-user NOMA fronthaul system is given by

$$R_k = \begin{cases} \log_2\left(1+\dfrac{SNR_k}{\Re+1}\right) & , \quad 1 \le k \le \dfrac{2M-1+(-1)^M}{4} \\ \dfrac{1}{2}\cdot\log_2\left(1+SNR_0\right) & , \quad k = \dfrac{M+1}{2} \\ \log_2\left(1+\dfrac{\Re\cdot SNR_k}{\Re+SNR_k+1}\right) & , \quad \dfrac{2M+5-(-1)^M}{4} \le k \le M \end{cases} \tag{25}$$

Note that (25) hold true for $\forall M \in \mathbb{N}, \forall k \in \mathbb{N}$. The scaling factor $\frac{1}{2}$ in (25) when $k = (M+1)/2$ is due to the employment of orthogonal multiplexing for the non-NOMA user, where only half of the bandwidth is allocated compared with NOMA users.

6.4.2 Cell Throughput

Here we present the analytical results of the cell total throughput where 2-user NOMA clusters are employed in the fronthaul networks. Both fixed ratio and dynamic ratio for various clusters in the cell are considered, and the closed-form expression of the optimal ratio in a cell will be demonstrated.

- *Same ratio for various clusters in the cell*

The achievable cell throughput, C_{cell}, is the summation of the throughput of each user located within the small cell. In the case where fixed ratio is deployed for every NOMA cluster in the cell, the cell throughput can be represented as

$$\begin{cases} C_{cell} = \dfrac{1-(-1)^M}{4} B\log_2(1+SNR_0) + \displaystyle\sum_{k=1}^{\frac{2M-1+(-1)^M}{4}} B\log_2\left(1+\dfrac{SNR_k}{\Re+1}\right) \\ \qquad + \displaystyle\sum_{k=\frac{2M+5-(-1)^M}{4}}^{M} B\log_2\left(1+\dfrac{\Re\cdot SNR_k}{\Re+SNR_k+1}\right) \\ SNR_k = \dfrac{P_{rk}}{N_k+G_kN_{Tx}} = \dfrac{P_TG_rG_t}{N_k\cdot\left(\dfrac{4\pi f}{c}\right)^2\cdot r_k^{\,n}\cdot 10^{\chi_\delta/10}+N_{Tx}G_rG_t} \quad , \quad k \in \{1,2,...,M\} \end{cases} \tag{26}$$

where B is the signal bandwidth, $\Re$ is the power allocation ratio that is the same for all clusters in the cell. The first term on the right in (26) represents the capacity of the non-NOMA user,

the second and third terms denote the capacity of near users and far users in the clusters, respectively. Since the user locations are already known once the user distribution scheme is chosen, the set of user distances r_k is deterministic. Hence, the cell capacity in (26) is a function of the ratio $\Re$. The optimum ratio that maximises the cell throughput will be derived in the next section.

- *Dynamic ratio for various clusters in the cell*

In the case where dynamic ratio is applied in various NOMA clusters, the cell throughput is given by

$$\begin{cases} C_{cell} = \dfrac{1-(-1)^M}{4} B\log_2(1+SNR_0) + \sum\limits_{k=1}^{\frac{2M-1+(-1)^M}{4}} B\log_2\left(1+\dfrac{SNR_k}{\Re_k+1}\right) \\ \qquad + \sum\limits_{k=\frac{2M+5-(-1)^M}{4}}^{M} B\log_2\left(1+\dfrac{\Re_k \cdot SNR_k}{\Re_k+SNR_k+1}\right) \\ SNR_k = \dfrac{P_{rk}}{N_k+G_kN_{Tx}} = \dfrac{P_T G_r G_t}{N_k \cdot \left(\dfrac{4\pi f}{c}\right)^2 \cdot r_k^{\,n} \cdot 10^{\chi_\delta/10} + N_{Tx} G_r G_t} \quad , \quad k \in \{1,2,...,M\} \end{cases} \tag{27}$$

Similarly, the cell throughput is a function of the power allocation ratio, $\Re_k$, which is dynamically determined according to the channel gains of the near and far users in the cluster.

6.5 Optimum Power Allocation Ratio

For downlink 2-user NOMA fronthaul networks, the optimal power allocation ratio in the cell can be determined such that the cell total throughput is maximum. The derivative of a NOMA cluster throughput is always negative as shown below

$$\begin{aligned} &C_{pair\_k}{}' = (C_{n\_k} + C_{f\_k})' \\ &= -\frac{B}{\ln 2}\left[\frac{(\Re+1)SNR_{n\_k}}{(\Re+SNR_{n\_k}+1)\cdot(\Re+1)^2} + \frac{(\Re+SNR_{f\_k}+1)\cdot\Re\cdot SNR_{f\_k}}{(\Re\cdot SNR_{f\_k}+\Re+SNR_{f\_k}+1)\cdot(\Re+SNR_{f\_k}+1)^2}\right] < 0 \end{aligned} \tag{28}$$

Hence, the NOMA cluster throughput is a monotonic decreasing function of the ratio. We have the conclusion that small power allocation ratio is preferred to achieve higher NOMA cluster throughput thus the cell total throughput. In the following, we will formulate the NOMA power allocation optimisation problem of both fixed ratio and dynamic ratio for various clusters in the cell.

The goal of the downlink NOMA fronthaul power allocation approach is to maximise the cell throughput with the constraints: keeping the SINR of each user below a SINR threshold T such that all the users can properly demodulate the received signals. Hence, the optimal power allocation problem can be formulated as

$$\max_{T,\Re} C_{cell} \text{ , subject to: } \mathrm{SINR_{Tx}} \geq T \text{ and } \mathrm{SINR_k} \geq T, \forall k \in \{1,2,\dots,M\}$$

Since the cell throughput is a monotonic decreasing function of the ratio, the optimisation problem is equivalent to

$$\min_{T} \Re \text{ , subject to: } \mathrm{SINR_{Tx}} \geq T \text{ and } \mathrm{SINR_k} \geq T, \forall k \in \{1,2,\dots,M\}.$$

- *Fixed ratio for various clusters in the cell*

In the case of fixed ratio for various clusters in the cell, the constraints of the optimisation problem can be simplified and represented as

$$\begin{cases} \dfrac{T(SNR_{Tx}+1)}{SNR_{Tx}-T} \leq \Re \leq \dfrac{SNR_{Tx}}{T}-1 \\ \dfrac{T(SNR_{M}+1)}{SNR_{M}-T} \leq \Re \leq \dfrac{SNR_{(2M-1+(-1)^{M})/4}}{T}-1 \\ SNR_{Tx} \geq T^2+2T \\ SNR_{M} > T \end{cases} \tag{29}$$

In (29), the third and fourth inequalities originated from the constraints that the upper limit should be larger than the lower limit in the first and second inequalities. Note that the optimum, i.e. minimum ratio in the cell can be found among the lower limits of the first two inequalities, whichever is smaller.

Hence, the closed-form optimal power allocation solution in this case is given by:

$$\Re_{opt} = \min\left\{ \frac{T(SNR_{Tx}+1)}{SNR_{Tx}-T} \quad , \quad \frac{T(SNR_{M}+1)}{SNR_{M}-T} \right\} \tag{30}$$

where $\mathrm{SNR_{Tx}} \geq T^2 + 2T$ *and* $SNR_M > T$ should be satisfied. Note that the optimum ratio in the cell is determined by the user with lowest channel gain in the cell. The optimal cell throughput can be calculated by substituting (30) into (26).

- *Dynamic ratio for various clusters in the cell*

In the case of dynamic ratio for various clusters in the cell, the per cluster capacity optimisation should be considered instead of the cell total throughput optimisation to simplify the problem. Similarly, the problem of maximising the throughput of a NOMA cluster subject to the constraints of user SINR threshold is equivalent to the problem of minimising the ratio of every cluster subject to the constraint of user SINR threshold:

$$\min_{T} \Re_k \text{ , subject to: } \mathrm{SINR_{Tx}} \geq T, \mathrm{SINR_{nk}} \geq T, \text{ and } \mathrm{SINR_{fk}} \geq T$$

Therefore, the optimal ratio in this case is a set of optimised ratios that maximise the throughput of each cluster thus the cell throughput. The constraints of this optimisation problem can be simplified and represented as

$$\begin{cases} \dfrac{T(SNR_{Tx}+1)}{SNR_{Tx}-T} \leq \Re_k \leq \dfrac{SNR_{Tx}}{T} - 1 \\ \dfrac{T(SNR_{fk}+1)}{SNR_{fk}-T} \leq \Re_k \leq \dfrac{SNR_{nk}}{T} - 1 \end{cases} \tag{31}$$

As can be seen in (31), the optimal ratio for a NOMA cluster is decided by the threshold T and SNR of the far user in the cluster, i.e. the distance from the far user to the RRH. The closed-form optimum power allocation ratio set in the cell is represented as

$$\Re_{opt} = \left\{ \Re_{k\_opt} \middle| \Re_{k\_opt} = \min\left\{ \frac{T(SNR_{Tx}+1)}{SNR_{Tx}-T} \quad , \quad \frac{T(SNR_{fk}+1)}{SNR_{fk}-T} \right\}, k = 1,2,...,M \right\} \tag{32}$$

The optimal cell throughput can be calculated by substituting (32) into (27).

6.6 Simulation Results and Discussions of Downlink NOMA Fronthaul System

In this section, the throughput performance and spectral efficiency (bits/s/Hz) of the downlink NOMA fronthaul networks will be demonstrated using the proposed user distribution and clustering schemes. The performance of the NOMA system will also be compared with conventional orthogonal multiple access (OMA) system (e.g., orthogonal frequency-division multiple access (OFDM)) to illustrate the superior performance of employing NOMA in the fronthaul scenario.

Table 6.1 Simulation Parameters

Parameters	**Value**
Cell Radius (D)	110 m
Number of users in the cell (M)	101
Antenna gain at RRH/UE	25 dBi
Power budget for a cluster (P_T)	0 dBm
Path loss exponent	2.1
Shadow factor (χ_σ)	$\sigma = 3.76$ dB
UE distribution scaling factor (β)	10
Signal carrier frequency	60 GHz
SINR threshold	4 dB

The system parameters used in the numerical simulation is shown in Table 6.1. The cell radius is chosen to be 110 meters to represent a small cell. The number of users in the cell is 101 such that 50 clusters will be generated as well as a non-NOMA user. Since higher emission limit is allowed for 60-GHz devices that operate outdoors with very high gain antennas to encourage broader deployment of point-to-point broadband systems [176], the antenna gain is set to be 25

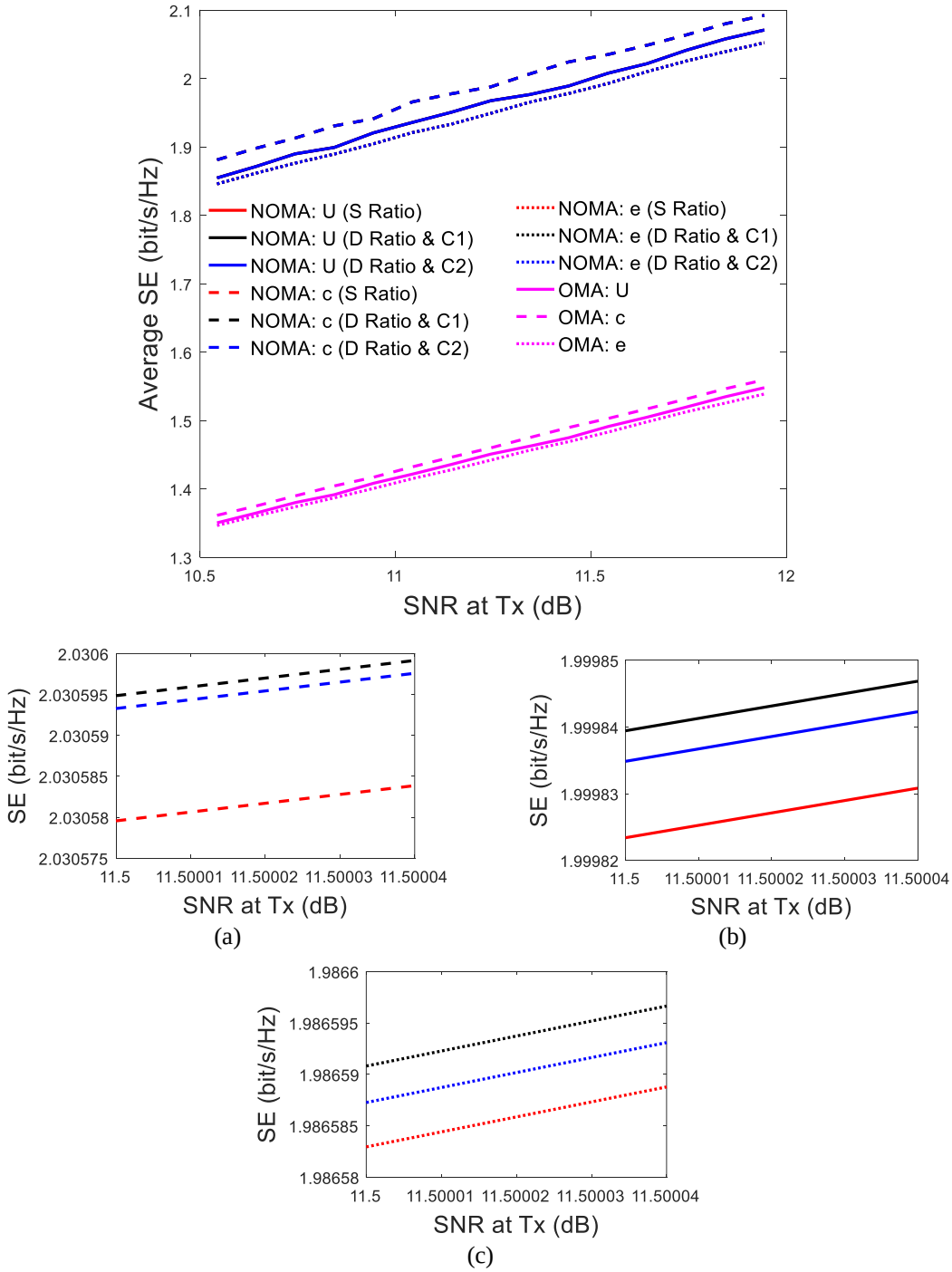

Fig. 6.6 Average spectral efficiency for NOMA-based and OMA-based RoF fronthaul systems. Insets show the zoom in illustration of NOMA system with (a) clustering to the centre distribution of fixed ratio among various clusters (red dash line), dynamic ratio with clustering scheme 1 (black dash line), and dynamic ratio with clustering scheme 2 (blue dash line); (b) uniform distribution; (c) clustering to the edge. (U: uniform distribution; c: clustering to centre; e: clustering to edge; S Ratio: fixed ratio among various clusters; D Ratio: dynamic ratio; C1: clustering scheme 1; C2: clustering scheme 2)

dBi for both transmit and receive antennas. Furthermore, higher antenna gain is desired in 60 GHz fibre-wireless communication for better coverage, as well as to maintain a lower RF exposure levels in the near field. The path loss exponent of the 60 GHz radio channel is chosen to be 2.1 [177] and the shadowing effect is represented by a zero mean Gaussian random variable, χ_σ, with a standard deviation $\sigma = 3.76$ dB [178]. As an example, the SINR threshold of the receiver is assumed to be 4 dB [179].

In the NOMA-based 60-GHz RoF fronthaul links, the optimal power allocation ratio we have derived in section 6.5 is utilised in the simulation to achieve the maximised throughput of the cell. Fig. 6.6 shows the average spectral efficiency of the small cell covering 101 users served by NOMA-based 60-GHz RoF fronthaul links as well as conventional OMA-based fronthaul links. Fig. 6.6 is obtained by considering three user distributions (uniform distribution, clustering to the centre and clustering to the edge) for both NOMA and OMA systems. The key observations from Fig. 6.6 are as follows:

- The optimised NOMA-based fronthaul systems achieve tremendous spectral efficiency gain (about 35%) compared with OMA-based fronthaul systems for all user distributions. This result is expected since NOMA is envisioned to improve the spectral efficiency in the downlink fronthaul networks.
- User distribution of clustering to the centre has the best throughput performance, while user clustering to the edge obtains the least spectral efficiency in both NOMA and OMA systems. This is due to the higher throughputs of the higher channel gain users achieved when more users are distributed near the cell centre.
- In the NOMA-based fronthaul networks, different power allocation ratio schemes and clustering schemes have limited impact on the performance of spectral efficiency as shown in the insets (a)-(c) in Fig. 6.6. As can be observed from the insets, NOMA networks using dynamic ratio (shown as black and blue in the insets) have better spectral efficiency compared with that using same ratio among various clusters. NOMA clustering scheme 1 (as mentioned in Fig. 6.5) has better spectral efficiency compared with clustering scheme 2. Note that Fig. 6.6 shows the average spectral efficiency performance all over the cell among 101 users, the performance differences between near and far users are averaged and not shown in the figures.

In conclusion, the application of NOMA in the 60-GHz RoF fronthaul networks is a promising approach for improving the spectral efficiency performance. Despite the utilisation of dynamic ratio with clustering scheme 1 provides the best average spectral efficiency performance in the cell, it sacrifices the computational complexity in computing the optimum ratio for each cluster. On the other hand, the NOMA approach using a fixed ratio among all the clusters achieves similar performance with simplified power allocation ratio design at the base station. Hence, dynamic ratio with clustering scheme 1 offers the maximised cell throughput, while fixed ratio scheme is suitable for delay-limited fronthaul networks where the users are sensitive to the fronthaul delay and requires simplified ratio allocation approaches.

6.7 Summary

The main contributions of this chapter are listed as follows:

Firstly, we demonstrated a tractable model of the RoF fronthaul networks based on NOMA with coordinated BSs. This model is focused on a fronthaul link containing two small cells. The user located at the cell edge of two cells is served using CoMP transmission to mitigate the impact of inter-cell interference as well as improve the received signal quality and cell coverage. While the data stream of near users within each cell are multiplexed in power domain with that of the edge user using NOMA technique to improve the system spectral efficiency. Theoretical studies have been carried out to demonstrate the feasibility of the proposed scheme.

Secondly, we further extended the model of downlink NOMA RoF fronthaul systems. The impact of user distributions, NOMA clustering schemes and noise originated from the photonic side were considered in the model to provide a more realistic representation of real applications. Mathematical expressions of the user and cell throughput were derived. Simulation results showed that NOMA fronthaul system could achieve about 35% average spectral efficiency gain compared to traditional OMA fronthaul system. Besides, different user distributions provided different cell throughput, where users clustered to the cell centre had the highest cell throughput. Dynamic power ratio allocation scheme had a better spectral efficiency compared with the fixed ratio scheme for various clusters at the cost of higher computational complexity trading off with system cost and latency. The choice of power allocation scheme and NOMA

clustering scheme depend on the system requirements such as deployment scenario, system cost budget and latency requirement. Hence, the derived model can offer insights to future fronthaul system design with regard to various scenarios requirements.

Chapter 7 Conclusion

7.1 Thesis Overview

The next generation communication system has posed challenges in the data rate, end-to-end latency, system throughput, spectral efficiency, energy efficiency and cost-effectiveness on the network. Fronthaul network is the bottleneck which constraints the performance of high-speed, high capacity networks. This thesis is aimed at exploring cost-effective opto-electronic technologies, fronthaul system architectures and advanced spectral efficient techniques to address the ever-increasing need for network capacity and transmission data rate. Several promising techniques for next generation communications are proposed, investigated and developed in fronthaul systems, including license-free mm-wave spectrum band, RoF technique and advanced technologies such as CoMP and NOMA, to facilitate next-generation networks with high mobility and broadband radio access.

In Chapter 2, a comprehensive literature review on key enablers for next generation communication systems has been presented and summarised. Various fronthaul options have been surveyed and analysed, including wireless fronthaul solutions and wired/optical fronthaul solutions. The bandwidth and data rate limitations of conventional digital fronthaul links based on CPRI and OBSAI are discussed, leading to the re-investigation of potential analog-fronthaul solutions. Besides, state-of-the-art research investigations of analog RoF fronthaul systems have been summarised and discussed. As a promising candidate for future communication networks, mm-wave signal generation methods in optical domain are thoroughly reviewed. The advantages and constraints of various mm-wave signal generation approaches are summarised. Different signal transmission impairments (RF power fading, noise and distortion) originated from fibre chromatic dispersion and nonlinearity of electrical and optical devices have been presented. Possible solutions to mitigate or avoid these impairments are also demonstrated and reviewed. Since inter-cell interference will be a severe issue in future massive small cells deployment, fronthaul networks based on CoMP transmission are studied to mitigate the interference, improve spectral efficiency, improve cell throughput and to extend cell coverage.

Finally, current research investigations on spectral efficiency improvements such as SEFDM and NOMA have been reviewed. Theoretical and experimental studies on NOMA based multiple access networks for significant spectral efficiency gain have been presented.

In Chapter 3, two proposed analog RoF fronthaul systems based on a variation of OSSB and DSB-SC modulation techniques are presented. The proposed schemes are achieved using two cascaded external modulators that will relax the stringent requirements for high-speed electrical component for optical mm-wave signal generation. The operation principle, system architectures and experimental setup have been described. A systematic comparison of the system performance of two fronthaul alternatives are presented as well as the impact of chromatic dispersion along different length of fronthaul links. Experimental demonstrations have been carried out by transmitting 4-QAM and 16-QAM 60.25-GHz signals over 3-km and 10-km analog fronthaul fibre links. Up to 8 Gbps error-free data transmission has been experimentally demonstrated and it has been verified that the modified OSSB fronthaul link has a better receiver sensitivity compared to the modified DSB-SC scheme. In addition, RF power fading can be eliminated using the modified OSSB fronthaul solution. Furthermore, a cost-effective fronthaul system design is achieved using integrated microwave photonic filters in the BBU to serve as a small-size and low-cost optical filtering function. In the experiments, a wavelength tunable notch filter is cascaded with a bandpass filter to obtain a filter profile of two passbands with a frequency separation of around 60 GHz. It is validated that the fronthaul link performance can be further improved with smaller insertion loss and steeper roll-off integrated filters.

In Chapter 4, thorough analytical models of the proposed 60-GHz RoF fronthaul systems are presented. Received RF signal power as a function of system OCSR is derived for two fronthaul schemes to compare their performance. Simulation results illustrate that smaller OCSR exists in the modified OSSB fronthaul system, thus providing better receiver sensitivity compared with the modified DSB-SC fronthaul scheme. Mathematical expressions of the total noise power in the two fronthaul systems are calculated to evaluate system performance. In addition, power consumption and system parameters comparison of the two schemes are demonstrated to provide typical design parameters for 60-GHz mm-wave RoF fronthaul link design. Furthermore, fibre chromatic dispersion effect is considered in the derived fronthaul models. The RF power fading performance of the modified DSB-SC fronthaul link is compared with

the traditional single stage DSB modulation based fronthaul link. Simulation results indicate that the modified DSB-SC fronthaul link is less sensitive to the dispersion effect and is feasible in real applications for short-reach fronthaul transmission.

In Chapter 5, a 60-GHz RoF fronthaul system using two advanced spectral-efficient techniques is experimentally demonstrated. The fronthaul network based on CoMP and NOMA can overcome the data rate and coverage bottleneck imposed by current mm-wave RoF fronthaul systems. We first demonstrate a downlink fronthaul system using CoMP transmission technique, serving a user located at the cell edge using two RRHs in two small cells. The cooperation of RRHs is achieved at the centralised BBU, where signals for the edge user are jointly processed using STBC to provide transmission diversity. Experimental results show that CoMP fronthaul system could obtain 1.3-dB receiver sensitivity improvement when transmitting 4-QAM signal along 10-km fibre fronthaul link compared with two fronthaul links transmission without STBC. Besides, CoMP based fronthaul systems are verified to be more robust against ISI caused by timing mismatch between two fronthaul links. We then characterise the system performance in terms of various signal angle of arrival, distance between two transmitters, the range of reception area and sensitivity to antenna misalignment. Furthermore, a 2-user NOMA based 60-GHz RoF fronthaul system is demonstrated experimentally. We have proposed a novel MLC-based NOMA scheme where SIC is not needed at the receiver such that the receiver complexity can be significantly reduced compared with conventional NOMA based on SPC and SIC. Data rate up to 8 Gbps is demonstrated transmitting 4 QAM signals over 3-km fibre fronthaul and 2.5-m wireless link. The proposed MLC-based NOMA fronthaul exhibits better BER performance than SPC-based NOMA fronthaul. No error propagation was observed and low-complexity receiver design was feasible using the proposed fronthaul scheme. We finally demonstrated a fronthaul system with jointly NOMA and CoMP technique in downlink transmission, providing mitigated impact of inter-cell interference and improved spectral efficiency.

In chapter 6, theoretical studies of advanced techniques in RoF fronthaul system are presented. We first derive a tractable model of the RoF fronthaul system based on NOMA with coordinated BSs, focusing on fronthaul system containing two cooperated small cells. Theoretical investigations have been carried out to demonstrate the feasibility of proposed fronthaul systems. The downlink fronthaul system based on NOMA is further investigated to

provide a more realistic representation of real applications where large numbers of users exist in the cell. Different user distribution schemes (clustering to centre, clustering to edge and uniform distribution), and different NOMA pair clustering schemes are considered in the analytical model. The noise induced from the photonic side has also been taken into account. Mathematical expressions of the effective SINR of each user within the cell, the closed-form expression of system capacity and the optimal power allocation ratio are derived. NOMA fronthaul system is verified to achieve about 35% average spectral efficiency gain compared with the traditional OMA fronthaul system through simulation. In addition, the impact of user distributions is presented, indicating that users clustering to centre has the highest cell throughput. Dynamic power ratio allocation scheme could obtain better spectral efficiency compared with the fixed ratio among various clusters at the cost of higher computational complexity trading off with system cost and latency.

7.2 Future Work

This work presented systematic investigation and comparison on mm-wave RoF fronthaul systems using a variation of two popular external modulation techniques: the modified DSB-SC scheme and the modified OSSB scheme. Both experimental and theoretical demonstrations are presented in terms of their BER performance, ability to overcome the chromatic dispersion effect and cost reduction design of proposed fronthaul systems. Advanced techniques (CoMP and NOMA) to mitigate the inter-cell interference, improve cell edge throughput, extend cell coverage and improve system spectral efficiency have also been proposed and developed in the RoF fronthaul systems. However, several related research topics came up during the investigations which could not be pursued in this thesis and could be of paramount importance for further investigation.

- In the 60-GHz RoF fronthaul transmission scheme that we proposed in Chapter 3, an IQ mixer is used to up-convert the baseband signals to an IF frequency. The amplifier to drive the IQ mixer introduced nonlinearity to the system which degrades the BER performance and limit the realisation of higher-order QAM modulation format.

Linearisation techniques such as electrical analog linearisation or optical linearisation can be employed in the system to mitigate the distortion caused by nonlinearity.

- In our experimental setup, the BPF employed after the photodiode only has a bandwidth of around 2 GHz, limiting the transmission of higher bandwidth signals. Thus, the highest achievable data rate in our experiments is only 8 Gbps for 16 QAM transmission. With a wider bandwidth BPF in the 60-GHz range and nonlinearity techniques, much higher data rate can be achieved. Another option is to use an optical IQ modulator and avoid the use of electrical IQ mixer for mm-wave signal generation. In this way, the nonlinearity of fronthaul links can be greatly reduced and higher-order modulation format can be achieved.

- New wireless transmission technologies, such as beamforming and massive MIMO, that can exploit the intrinsic benefits of 60-GHz mm-wave spectrum have been recognised by researchers for the provision of broadband radio access with massive connections. In Chapter 5, we use a pair of horn antennas to emulate the directional characteristics of beamforming. However, to facilitate beamforming or massive MIMO in fronthaul systems, large antenna arrays working in the 60-GHz frequency-band are needed. Advanced processing capability in the BBU is also required. Longer transmission distance, extended cell coverage and improved mobility of small cells are envisioned with the deployment of beamforming and massive MIMO.

- The NOMA and CoMP schemes employed in proposed fronthaul system in Chapter 5 require perfect knowledge of the channel state information at the receiver, resulting in increased latency along fronthaul links and increased receiver complexity. More efficient channel estimation algorithms are deserved to be further investigated to provide accurate channel estimation and fast convergence.

- Only downlink transmission of 60-GHz RoF fronthaul systems is demonstrated as detailed in Chapter 3 and 5. Transmission of 60-GHz mm-wave signals using analog RoF technique provides various merits, including reduced RRH structure that will

decrease system cost in massive small cell deployment, large available licence-free spectrum in 60-GHz frequency range and centralised BBU function that facilitate future C-RAN architecture. However, uplink 60-GHz RoF fronthaul systems pose a challenge: the optical mm-wave signal generation at the RRH requires additional devices such as laser diodes and high-speed modulators that will increase the cost of system tremendously. An effective way of frequency re-use in the RRH or utilisation of dual mode laser diodes with a frequency separation of around 60-GHz needed to be investigated in the future to obtain cost-effective uplink fronthaul transmission.

- As we have discussed, both wireless and wired/optical fronthaul have constraints in different scenarios. Wireless fronthaul systems based on FSO or mm-wave frequency bands offer a wider bandwidth, higher mobility and higher flexibility compared with optical fronthaul systems. In addition, in some situations, optical fibre may not be available for fronthaul deployment. However, wireless fronthaul systems are severely influenced by weather conditions and the cost of equipment and maintenance is higher compared with optical RoF fronthaul systems. The hybrid wireless and optical fronthaul system will be necessary in some scenarios where they can complement with each other. The coexistence of different types of fronthaul structure requires coordination in the centralised BBU pool and should be further investigated.

Bibliography

[1] R. Waterhouse and D. Novack, "Realizing 5G: microwave photonics for 5G mobile wireless systems," *IEEE Microwave Magazine,* vol. 16, pp. 84-92, 2015.

[2] S. Chen and J. Zhao, "The requirements, challenges, and technologies for 5G of terrestrial mobile telecommunication," *IEEE Communications Magazine,* vol. 52, pp. 36-43, 2014.

[3] Q. C. Li, H. Niu, A. T. Papathanassiou, and G. Wu, "5G network capacity: key elements and technologies," *Vehicular Technology Magazine, IEEE,* vol. 9, pp. 71-78, 2014.

[4] M. Marcus and B. Pattan, "Millimeter wave propagation; spectrum management implications," *Microwave Magazine, IEEE,* vol. 6, pp. 54-62, 2005.

[5] F. Kronestedt and S. Andersson, "Migration of adaptive antennas into existing networks," in *Vehicular Technology Conference, 1998. VTC 98. 48th IEEE*, 1998, pp. 1670-1674.

[6] J. Hoadley and P. Maveddat, "Enabling small cell deployment with HetNet," *IEEE Wireless Communications,* vol. 19, pp. 4-5, 2012.

[7] S. Akoum and J. Acharya, "Full-dimensional MIMO for future cellular networks," in *Radio and Wireless Symposium (RWS), 2014 IEEE*, 2014, pp. 1-3.

[8] E. G. Larsson, O. Edfors, F. Tufvesson, and T. L. Marzetta, "Massive MIMO for next generation wireless systems," *IEEE Communications Magazine,* vol. 52, pp. 186-195, 2014.

[9] A. Sendonaris, E. Erkip, and B. Aazhang, "User cooperation diversity. Part I. System description," *IEEE Transactions on Communications,* vol. 51, pp. 1927-1938, 2003.

[10] R. Irmer, H. Droste, P. Marsch, M. Grieger, G. Fettweis, S. Brueck, *et al.*, "Coordinated multipoint: Concepts, performance, and field trial results," *IEEE Communications Magazine,* vol. 49, pp. 102-111, 2011.

[11] Z. Ding, Z. Yang, P. Fan, and H. V. Poor, "On the performance of non-orthogonal multiple access in 5G systems with randomly deployed users," *IEEE Signal Processing Letters*, vol. 21, pp. 1501-1505, 2014.

[12] C. Mobile, "C-RAN: the road towards green RAN," *White Paper, version*, vol. 2, 2011.

[13] M. Peng, C. Wang, V. Lau, and H. V. Poor, "Fronthaul-constrained cloud radio access networks: Insights and challenges," *IEEE Wireless Communications*, vol. 22, pp. 152-160, 2015.

[14] M. Peng, Y. Li, Z. Zhao, and C. Wang, "System architecture and key technologies for 5G heterogeneous cloud radio access networks," *IEEE network*, vol. 29, pp. 6-14, 2015.

[15] I. Chih-Lin, Y. Yuan, J. Huang, S. Ma, C. Cui, and R. Duan, "Rethink fronthaul for soft RAN," *IEEE Communications Magazine*, vol. 53, pp. 82-88, 2015.

[16] A. Ericsson, "Common Public Radio Interface (CPRI) Specification V6. 0," ed, 2013.

[17] N. Alliance, "5G white paper," *Next generation mobile networks, white paper*, 2015.

[18] F. Boccardi, R. W. Heath, A. Lozano, T. L. Marzetta, and P. Popovski, "Five disruptive technology directions for 5G," *IEEE Communications Magazine*, vol. 52, pp. 74-80, 2014.

[19] V. Jungnickel, K. Manolakis, W. Zirwas, B. Panzner, V. Braun, M. Lossow, *et al.*, "The role of small cells, coordinated multipoint, and massive MIMO in 5G," *IEEE Communications Magazine*, vol. 52, pp. 44-51, 2014.

[20] G. Wunder, P. Jung, M. Kasparick, T. Wild, F. Schaich, Y. Chen, *et al.*, "5GNOW: non-orthogonal, asynchronous waveforms for future mobile applications," *IEEE Communications Magazine*, vol. 52, pp. 97-105, 2014.

[21] G.-K. Chang and L. Cheng, "Fiber-wireless fronthaul: The last frontier," in *OptoElectronics and Communications Conference (OECC) held jointly with 2016 International Conference on Photonics in Switching (PS), 2016 21st*, 2016, pp. 1-3.

[22] C. Lim, A. Nirmalathas, K.-L. Lee, C. Ranaweera, E. Wong, and Y. Tian, "Radio-over-Fiber technology: past and present," in *Asia Communications and Photonics Conference*, 2017, p. S3E. 1.

[23] T. X. Vu, T. Van Nguyen, and T. Q. Quek, "Power optimization with BLER constraint for wireless fronthauls in C-RAN," *IEEE Communications Letters,* vol. 20, pp. 602-605, 2016.

[24] S.-H. Park, K.-J. Lee, C. Song, and I. Lee, "Joint design of fronthaul and access links for C-RAN with wireless fronthauling," *IEEE signal processing letters,* vol. 23, pp. 1657-1661, 2016.

[25] J. C. Juarez, A. Dwivedi, A. R. Hammons, S. D. Jones, V. Weerackody, and R. A. Nichols, "Free-space optical communications for next-generation military networks," *IEEE Communications Magazine*, vol. 44, 2006.

[26] T. P. McKenna, J. C. Juarez, J. A. Nanzer, and T. R. Clark, "Hybrid millimeter-wave/free-space optical system for high data rate communications," in *Photonics Conference (IPC), 2013 IEEE*, 2013, pp. 203-204.

[27] M. Alzenad, M. Z. Shakir, H. Yanikomeroglu, and M.-S. Alouini, "FSO-based vertical backhaul/fronthaul framework for 5G+ wireless networks," *IEEE Communications Magazine,* vol. 56, pp. 218-224, 2018.

[28] I. Bor-Yaliniz and H. Yanikomeroglu, "The new frontier in RAN heterogeneity: Multi-tier drone-cells," *IEEE Communications Magazine*, vol. 54, pp. 48-55, 2016.

[29] G. R. MacCartney and T. S. Rappaport, "Study on 3GPP rural macrocell path loss models for millimeter wave wireless communications," in *Communications (ICC), 2017 IEEE International Conference on*, 2017, pp. 1-7.

[30] K. Haneda, J. Zhang, L. Tan, G. Liu, Y. Zheng, H. Asplund, *et al.*, "5G 3GPP-like channel models for outdoor urban microcellular and macrocellular environments," in *2016 IEEE 83rd Vehicular Technology Conference (VTC Spring)*, 2016, pp. 1-7.

[31] M. K. Samimi, G. R. MacCartney, S. Sun, and T. S. Rappaport, "28 GHz millimeter-wave ultrawideband small-scale fading models in wireless channels," in *Vehicular Technology Conference (VTC Spring), 2016 IEEE 83rd*, 2016, pp. 1-6.

[32] M. K. Samimi and T. S. Rappaport, "3-D millimeter-wave statistical channel model for 5G wireless system design," *IEEE Transactions on Microwave Theory and Techniques*, vol. 64, pp. 2207-2225, 2016.

[33] A. I. Sulyman, A. Alwarafy, G. R. MacCartney, T. S. Rappaport, and A. Alsanie, "Directional radio propagation path loss models for millimeter-wave wireless networks in the 28-, 60-, and 73-GHz bands," *IEEE Transactions on Wireless Communications*, vol. 15, pp. 6939-6947, 2016.

[34] P.-H. Kuo and A. Mourad, "Millimeter wave for 5G mobile fronthaul and backhaul," in *Networks and Communications (EuCNC), 2017 European Conference on*, 2017, pp. 1-5.

[35] J. Lun, D. Grace, A. Burr, Y. Han, K. Leppanen, and T. Cai, "Millimetre wave backhaul/fronthaul deployments for ultra-dense outdoor small cells," in *2016 IEEE Wireless Communications and Networking Conference*, 2016, pp. 1-6.

[36] K. Min, M. Jung, S. Shin, S. Kim, and S. Choi, "System level simulation of mmWave based mobile Xhaul networks," in *2017 IEEE 85th Vehicular Technology Conference (VTC Spring)*, 2017, pp. 1-5.

[37] J. Mack and P. Cabrol, "EdgeLink™ mmW mesh transport experiments in the Berlin 5G-crosshaul testbed," in *2017 IEEE Long Island Systems, Applications and Technology Conference (LISAT)*, 2017, pp. 1-6.

[38] Z. Tayq, P. Chanclou, T. Diallo, K. Grzybowski, F. Saliou, S. Gosselin, *et al.*, "Performance demonstration of fiber and wireless fronthaul combination with remote powering," in *Optical Fiber Communications Conference and Exhibition (OFC), 2016*, 2016, pp. 1-3.

[39] Open Base Station Architecture Initiative (OBSAI) <http://www.obsai.com>

[40] European Telecommunications Standards Institute, Group Specification, Open Radio equipment Interface (ETSI GS ORI) 001, Requirements for ORI (Release 4), October, 2014.

[41] T. Pfeiffer, "Next generation mobile fronthaul and midhaul architectures," *Journal of Optical Communications and Networking*, vol. 7, pp. B38-B45, 2015.

[42] B. Guo, W. Cao, A. Tao, and D. Samardzija, "LTE/LTE‐A signal compression on the CPRI Interface," *Bell Labs Technical Journal*, vol. 18, pp. 117-133, 2013.

[43] K. Miyamoto, S. Kuwano, J. Terada, and A. Otaka, "Split-PHY processing architecture to realize base station coordination and transmission bandwidth reduction in mobile fronthaul," in *Optical Fiber Communication Conference*, 2015, p. M2J. 4.

[44] U. Dötsch, M. Doll, H. P. Mayer, F. Schaich, J. Segel, and P. Sehier, "Quantitative analysis of split base station processing and determination of advantageous architectures for LTE," *Bell Labs Technical Journal*, vol. 18, pp. 105-128, 2013.

[45] N. Shibata, T. Murakami, K. Ishihara, T. Kobayashi, J.-i. Kani, J. Terada, *et al.*, "256-QAM 8 wireless signal transmission with DSP-assisted analog RoF for mobile front-haul in LTE-B," in *19th Optoelectronics and Communications Conference (OECC) and the 39th Australian Conference on Optical Fibre Technology (ACOFT)*, 2014, p. 129.

[46] S.-H. Cho, H. Park, H. S. Chung, K.-H. Doo, S. S. Lee, and J. H. Lee, "Cost-effective next generation mobile fronthaul architecture with multi-IF carrier transmission scheme," in *Optical Fiber Communication Conference*, 2014, p. Tu2B. 6.

[47] Y. Chenhui, X. Hu, X. Huang, Q. Chang, X. Sun, Z. Gao, *et al.*, "A first demonstration of a PON-based analog fronthaul solution supporting 120 20MHz LTE-A signals for future Het-Net radio access," in *Asia Communications and Photonics Conference*, 2015, p. ASu3E. 2.

[48] X. Liu, H. Zeng, N. Chand, and F. Effenberger, "Efficient mobile fronthaul via DSP-based channel aggregation," *Journal of Lightwave Technology*, vol. 34, pp. 1556-1564, 2016.

[49] K.-I. Kitayama, "Architectural considerations of fiber-radio millimeter-wave wireless access systems," *Fiber & Integrated Optics*, vol. 19, pp. 167-186, 2000.

[50] J. A. Zhang, I. B. Collings, C. S. Chen, L. Roullet, L. Luo, S.-W. Ho, *et al.*, "Evolving small-cell communications towards mobile-over-FTTx networks," *IEEE Communications Magazine,* vol. 51, pp. 92-101, 2013.

[51] Z. Jia, J. Yu, G. Ellinas, and G.-K. Chang, "Key enabling technologies for optical–wireless networks: optical millimeter-wave generation, wavelength reuse, and architecture," *Journal of Lightwave Technology,* vol. 25, pp. 3452-3471, 2007.

[52] S. Alavi, M. Soltanian, I. Amiri, M. Khalily, A. Supa'at, and H. Ahmad, "Towards 5G: A photonic based millimeter wave signal generation for applying in 5G access fronthaul," *Scientific reports,* vol. 6, 2016.

[53] C.-T. Tsai, C.-H. Lin, C.-T. Lin, Y.-C. Chi, and G.-R. Lin, "60-GHz millimeter-wave over fiber with directly modulated dual-mode laser diode," *Scientific reports,* vol. 6, 2016.

[54] J. Li, H. Lee, and K. J. Vahala, "Microwave synthesizer using an on-chip Brillouin oscillator," *Nature communications,* vol. 4, 2013.

[55] P.-T. Shih, J. Chen, C.-T. Lin, W.-J. Jiang, H.-S. Huang, P.-C. Peng, *et al.*, "Optical millimeter-wave signal generation via frequency 12-tupling," *Journal of Lightwave Technology,* vol. 28, pp. 71-78, 2010.

[56] J. Li, T. Ning, L. Pei, C. Qi, Q. Zhou, X. Hu, *et al.*, "60 GHz millimeter-wave generator based on a frequency-quadrupling feed-forward modulation technique," *Optics letters,* vol. 35, pp. 3619-3621, 2010.

[57] C. R. Lima, D. Wake, and P. A. Davies, "Compact optical millimetre-wave source using a dual-mode semiconductor laser," *Electronics Letters,* vol. 31, pp. 364-366, 1995.

[58] C. Lim, M. Attygalle, A. Nirmalathas, D. Novak, and R. Waterhouse, "Analysis of optical carrier-to-sideband ratio for improving transmission performance in fiber-radio links," *Microwave Theory and Techniques, IEEE Transactions on,* vol. 54, pp. 2181-2187, 2006.

[59] G. H. Smith, D. Novak, and Z. Ahmed, "Overcoming chromatic-dispersion effects in fiber-wireless systems incorporating external modulators," *IEEE transactions on microwave theory and techniques,* vol. 45, pp. 1410-1415, 1997.

[60] B. Leesti, A. J. Zilkie, J. S. Aitchison, M. Mojahedi, R. H. Wang, T. J. Rotter, *et al.*, "Broad-band wavelength up-conversion of picosecond pulses via four-wave mixing in a quantum-dash waveguide," *IEEE photonics technology letters,* vol. 17, pp. 1046-1048, 2005.

[61] L. Johansson and A. Seeds, "Millimetre-wave radio-over-fibre transmission using an optical injection phase-lock loop source," in *Microwave Photonics, 2000. MWP 2000. International Topical Meeting on*, 2000, pp. 129-132.

[62] U. Gliese, S. Nørskov, and T. Nielsen, "Chromatic dispersion in fiber-optic microwave and millimeter-wave links," *Microwave Theory and Techniques, IEEE Transactions on,* vol. 44, pp. 1716-1724, 1996.

[63] C. Lim, A. Nirmalathas, M. Bakaul, K.-L. Lee, D. Novak, and R. Waterhouse, "Mitigation strategy for transmission impairments in millimeter-wave radio-over-fiber networks [Invited]," *Journal of Optical Networking,* vol. 8, pp. 201-214, 2009.

[64] H. Schmuck, "Comparison of optical millimetre-wave system concepts with regard to chromatic dispersion," *Electronics Letters,* vol. 31, pp. 1848-1848, 1995.

[65] J. Ma, C. Yu, Z. Zhou, and J. Yu, "Optical mm-wave generation by using external modulator based on optical carrier suppression," *Optics communications,* vol. 268, pp. 51-57, 2006.

[66] G. Smith, D. Novak, and Z. Ahmed, "Technique for optical SSB generation to overcome dispersion penalties in fibre-radio systems," *Electronics Letters,* vol. 33, pp. 74-75, 1997.

[67] D.-H. Jeon, H.-D. Jung, and S.-K. Han, "Mitigation of dispersion-induced effects using SOA in analog optical transmission," *IEEE Photonics Technology Letters,* vol. 14, pp. 1166-1168, 2002.

[68] J. Capmany, D. Pastor, P. Munoz, S. Sales, B. Ortega, and A. Martinez, "WDM-SSB generation and dispersion mitigation in radio over fiber systems with improved performance using an AWG multiplexer with flat top resonances," in *Microwave Photonics, 2003. MWP 2003 Proceedings. International Topical Meeting on*, 2003, pp. 39-42.

[69] E. Vourch, D. Le Berre, and D. Herve, "Lightwave single sideband wavelength self-tunable filter using an InP: Fe crystal for fiber-wireless systems," *IEEE Photonics Technology Letters*, vol. 14, pp. 194-196, 2002.

[70] P. Won, W. Zhang, and J. Williams, "Self-phase modulation dependent dispersion mitigation in high power SSB and DSB+ dispersion compensated modulated radio-over-fiber links," in *Microwave Symposium Digest, 2006. IEEE MTT-S International*, 2006, pp. 1947-1950.

[71] J. Marti, J. Fuster, and R. Laming, "Experimental reduction of chromatic dispersion effects in lightwave microwave/millimetre-wave transmissions using tapered linearly chirped fibre gratings," *Electronics Letters*, vol. 33, pp. 1170-1171, 1997.

[72] X. Zhang, R. Zhu, D. Shen, and T. Liu, "Linearization technologies for broadband radio-over-fiber transmission systems," in *Photonics*, 2014, pp. 455-472.

[73] X. Zhang, S. Saha, R. Zhu, T. Liu, and D. Shen, "Analog pre-distortion circuit for radio over fiber transmission," *IEEE Photonics Technology Letters*, vol. 28, pp. 2541-2544, 2016.

[74] R. Zhu, Z. Xuan, Y. Zhang, X. Zhang, and D. Shen, "Novel broadband analog predistortion circuit for radio-over-fiber systems," in *Microwave Symposium (IMS), 2015 IEEE MTT-S International*, 2015, pp. 1-4.

[75] Z. Chen, L. Yan, W. Pan, B. Luo, X. Zou, Y. Guo, *et al.*, "SFDR enhancement in analog photonic links by simultaneous compensation for dispersion and nonlinearity," *Optics Express*, vol. 21, pp. 20999-21009, 2013.

[76] B. Hraimel and X. Zhang, "Performance improvement of radio-over fiber links using mixed-polarization electro-absorption modulators," *IEEE Transactions on Microwave Theory and Techniques*, vol. 59, pp. 3239-3248, 2011.

[77] R. Zhu and X. Zhang, "Linearization of radio-over-fiber systems by using two lasers with different wavelengths," in *Microwave Symposium (IMS), 2014 IEEE MTT-S International*, 2014, pp. 1-3.

[78] A. Agarwal, T. Banwell, P. Toliver, and T. Woodward, "Predistortion compensation of nonlinearities in optical channelization systems for microwave applications," in *Optical Communication (ECOC), 2010 36th European Conference and Exhibition on*, 2010, pp. 1-3.

[79] X. Xie, Y. Dai, K. Xu, J. Niu, R. Wang, L. Yan, *et al.*, "Digital joint compensation of IMD3 and XMD in broadband channelized RF photonic link," *Optics express*, vol. 20, pp. 25636-25643, 2012.

[80] G. Americas, "4G Mobile Broadband Evolution 3GPP Release 10 and Beyond," ed: Jan, 2012.

[81] M. Sawahashi, Y. Kishiyama, A. Morimoto, D. Nishikawa, and M. Tanno, "Coordinated multipoint transmission/reception techniques for LTE-advanced [Coordinated and Distributed MIMO]," *IEEE Wireless Communications*, vol. 17, pp. 26-34, 2010.

[82] D. Lee, H. Seo, B. Clerckx, E. Hardouin, D. Mazzarese, S. Nagata, *et al.*, "Coordinated multipoint transmission and reception in LTE-advanced: deployment scenarios and operational challenges," *IEEE Communications Magazine*, vol. 50, pp. 148-155, 2012.

[83] V. Kotzsch and G. Fettweis, "Interference analysis in time and frequency asynchronous network MIMO OFDM systems," in *Wireless Communications and Networking Conference (WCNC), 2010 IEEE*, 2010, pp. 1-6.

[84] Y.-R. Tsai, H.-Y. Huang, Y.-C. Chen, and K.-J. Yang, "Simultaneous multiple carrier frequency offsets estimation for coordinated multi-point transmission in OFDM systems," *IEEE Transactions on Wireless Communications*, vol. 12, pp. 4558-4568, 2013.

[85] M. Li, X. Yun, S. Nagata, and L. Chen, "Power allocation of dynamic point blanking for downlink CoMP in LTE-advanced," in *Wireless Communications & Signal Processing (WCSP), 2013 International Conference on*, 2013, pp. 1-5.

[86] F. Zheng, M. Wu, and H. Lu, "Coordinated multi-point transmission and reception for LTE-advanced," in *Wireless Communications, Networking and Mobile Computing, 2009. WiCom'09. 5th International Conference on*, 2009, pp. 1-4.

[87] J. Li, M. Peng, A. Cheng, Y. Yu, and C. Wang, "Resource allocation optimization for delay-sensitive traffic in fronthaul constrained cloud radio access networks," 2014.

[88] B. Cheng, X. Mi, X. Xu, Z. Xu, X. Xu, and M. Zhao, "A real-time implementation of comp transmission based on cloud-ran infrastructure," in *2014 International Wireless Communications and Mobile Computing Conference (IWCMC)*, 2014, pp. 1033-1038.

[89] C. Fan, Y. J. Zhang, and X. Yuan, "Dynamic nested clustering for parallel PHY-layer processing in cloud-RANs," *IEEE Transactions on Wireless Communications,* vol. 15, pp. 1881-1894, 2016.

[90] S.-H. Park, O. Simeone, O. Sahin, and S. Shamai, "Robust layered transmission and compression for distributed uplink reception in cloud radio access networks," *IEEE Transactions on Vehicular Technology,* vol. 63, pp. 204-216, 2014.

[91] A. Liu and V. K. Lau, "Joint power and antenna selection optimization in large cloud radio access networks," *IEEE Transactions on Signal Processing,* vol. 62, pp. 1319-1328, 2014.

[92] S. Luo, R. Zhang, and T. J. Lim, "Downlink and uplink energy minimization through user association and beamforming in C-RAN," *IEEE Transactions on Wireless Communications,* vol. 14, pp. 494-508, 2015.

[93] L. Cheng, M. Zhu, M. M. U. Gul, X. Ma, and G.-K. Chang, "Adaptive photonics-aided coordinated multipoint transmissions for next-generation mobile fronthaul," *Journal of Lightwave Technology,* vol. 32, pp. 1907-1914, 2014.

[94] L. Cheng, M. M. U. Gul, F. Lu, M. Zhu, J. Wang, M. Xu, *et al.*, "Coordinated multipoint transmissions in millimeter-wave radio-over-fiber systems," *Journal of Lightwave Technology,* vol. 34, pp. 653-660, 2016.

[95] L. Cheng, M. Gul, A. Ng'oma, F. Lu, X. Ma, and G.-K. Chang, "High-diversity millimeter-wave CoMP transmission based on centralized SFBC in radio-over-fiber systems," in *Optical Fiber Communications Conference and Exhibition (OFC), 2015*, 2015, pp. 1-3.

[96] R. Q. Hu and Y. Qian, "An energy efficient and spectrum efficient wireless heterogeneous network framework for 5G systems," *IEEE Communications Magazine*, vol. 52, pp. 94-101, 2014.

[97] M. Rodrigues and I. Darwazeh, "A spectrally efficient frequency division multiplexing based communications system," in *Proc. 8th Int. OFDM Workshop*, 2003, pp. 48-49.

[98] I. Kanaras, A. Chorti, M. R. Rodrigues, and I. Darwazeh, "Spectrally efficient FDM signals: Bandwidth gain at the expense of receiver complexity," in *Communications, 2009. ICC'09. IEEE International Conference on*, 2009, pp. 1-6.

[99] I. Darwazeh, T. Xu, T. Gui, Y. Bao, and Z. Li, "Optical SEFDM system; bandwidth saving using non-orthogonal sub-carriers," *IEEE Photonics Technology Letters*, vol. 26, pp. 352-355, 2014.

[100] S. Mikroulis, T. Xu, J. E. Mitchell, and I. Darwazeh, "First demonstration of a spectrally efficient FDM radio over fiber system topology for beyond 4G cellular networking," in *Networks and Optical Communications-(NOC), 2015 20th European Conference on*, 2015, pp. 1-5.

[101] T. Xu, S. Mikroulis, J. E. Mitchell, and I. Darwazeh, "Bandwidth compressed waveform for 60-GHz millimeter-wave radio over fiber experiment," *Journal of Lightwave Technology*, vol. 34, pp. 3458-3465, 2016.

[102] Y. Saito, Y. Kishiyama, A. Benjebbour, T. Nakamura, A. Li, and K. Higuchi, "Non-orthogonal multiple access (NOMA) for cellular future radio access," in *Vehicular Technology Conference (VTC Spring), 2013 IEEE 77th*, 2013, pp. 1-5.

[103] A. Benjebbour, Y. Saito, Y. Kishiyama, A. Li, A. Harada, and T. Nakamura, "Concept and practical considerations of non-orthogonal multiple access (NOMA) for future radio access," in *Intelligent Signal Processing and Communications Systems (ISPACS), 2013 International Symposium on*, 2013, pp. 770-774.

[104] A. Benjebbour, A. Li, Y. Saito, Y. Kishiyama, A. Harada, and T. Nakamura, "System-level performance of downlink NOMA for future LTE enhancements," in *Globecom Workshops (GC Wkshps), 2013 IEEE*, 2013, pp. 66-70.

[105] S. N. Datta and S. Kalyanasundaram, "Optimal power allocation and user selection in non-orthogonal multiple access systems," in *Wireless Communications and Networking Conference (WCNC), 2016 IEEE*, 2016, pp. 1-6.

[106] S. Han, I. Chih-Lin, Z. Xu, and Q. Sun, "Energy efficiency and spectrum efficiency co-design: From NOMA to network NOMA," *IEEE COMSOC MMTC E-Letter*, vol. 9, 2014.

[107] R. Hoshyar, F. P. Wathan, and R. Tafazolli, "Novel low-density signature for synchronous CDMA systems over AWGN channel," *IEEE Transactions on Signal Processing*, vol. 56, pp. 1616-1626, 2008.

[108] M. Al-Imari, P. Xiao, M. A. Imran, and R. Tafazolli, "Uplink non-orthogonal multiple access for 5G wireless networks," in *Wireless Communications Systems (ISWCS), 2014 11th International Symposium on*, 2014, pp. 781-785.

[109] H. Nikopour and H. Baligh, "Sparse code multiple access," in *Personal Indoor and Mobile Radio Communications (PIMRC), 2013 IEEE 24th International Symposium on*, 2013, pp. 332-336.

[110] S. Chen, B. Ren, Q. Gao, S. Kang, S. Sun, and K. Niu, "Pattern division multiple access -- a novel nonorthogonal multiple access for fifth-generation radio networks," *IEEE Transactions on Vehicular Technology*, vol. 66, pp. 3185-3196, 2017.

[111] J. Huang, K. Peng, C. Pan, F. Yang, and H. Jin, "Scalable video broadcasting using bit division multiplexing," *IEEE Transactions on Broadcasting*, vol. 60, pp. 701-706, 2014.

[112] T. Wo and P. A. Hoeher, "Superposition mapping with application in bit-interleaved coded modulation," in *2010 International ITG Conference on Source and Channel Coding (SCC)*, 2010, pp. 1-6.

[113] L. Ping, L. Liu, K. Wu, and W. K. Leung, "Interleave division multiple-access," *IEEE Transactions on Wireless Communications*, vol. 5, pp. 938-947, 2006.

[114] V. V. Veeravalli and A. Mantravadi, "The coding-spreading tradeoff in CDMA systems," *IEEE Journal on Selected Areas in Communications*, vol. 20, pp. 396-408, 2002.

[115] L. Dai, B. Wang, Y. Yuan, S. Han, I. Chih-Lin, and Z. Wang, "Non-orthogonal multiple access for 5G: solutions, challenges, opportunities, and future research trends," *IEEE Communications Magazine*, vol. 53, pp. 74-81, 2015.

[116] Z. Feng, M. Tang, X. Guan, C. C.-K. Chan, Q. Wu, R. Wang, *et al.*, "Digital domain power division multiplexing DDO-OFDM transmission with successive interference cancellation," in *Lasers and Electro-Optics (CLEO), 2016 Conference on*, 2016, pp. 1-2.

[117] L. Yin, W. O. Popoola, X. Wu, and H. Haas, "Performance evaluation of non-orthogonal multiple access in visible light communication," *IEEE Transactions on Communications*, vol. 64, pp. 5162-5175, 2016.

[118] X. Guan, Y. Hong, Q. Yang, and C.-K. Chan, "Phase pre-distortion for non-orthogonal multiple access in visible light communications," in *Optical Fiber Communication Conference*, 2016, p. Th1H. 4.

[119] Y. Liu, M. Elkashlan, Z. Ding, and G. K. Karagiannidis, "Fairness of user clustering in MIMO non-orthogonal multiple access systems," *IEEE Communications Letters*, vol. 20, pp. 1465-1468, 2016.

[120] S. Timotheou and I. Krikidis, "Fairness for non-orthogonal multiple access in 5G systems," *IEEE Signal Processing Letters*, vol. 22, pp. 1647-1651, 2015.

[121] Z. Yang, Z. Ding, P. Fan, and N. Al-Dhahir, "A general power allocation scheme to guarantee quality of service in downlink and uplink NOMA systems," *IEEE Transactions on Wireless Communications*, vol. 15, pp. 7244-7257, 2016.

[122] Y. Sun, D. W. K. Ng, Z. Ding, and R. Schober, "Optimal joint power and subcarrier allocation for MC-NOMA systems," in *Global Communications Conference (GLOBECOM), 2016 IEEE*, 2016, pp. 1-6.

[123] L. Lei, D. Yuan, C. K. Ho, and S. Sun, "Joint optimization of power and channel allocation with non-orthogonal multiple access for 5G cellular systems," in *Global Communications Conference (GLOBECOM), 2015 IEEE*, 2015, pp. 1-6.

[124] Z. Ding, Y. Liu, J. Choi, Q. Sun, M. Elkashlan, I. Chih-Lin, *et al.*, "Application of non-orthogonal multiple access in LTE and 5G networks," *IEEE Communications Magazine*, vol. 55, pp. 185-191, 2017.

[125] A. S. Marcano and H. L. Christiansen, "Performance of non-orthogonal multiple access (NOMA) in mmWave wireless communications for 5G networks," in *Computing, Networking and Communications (ICNC), 2017 International Conference on*, 2017, pp. 969-974.

[126] J. Choi, "Non-orthogonal multiple access in downlink coordinated two-point systems," *IEEE Communications Letters*, vol. 18, pp. 313-316, 2014.

[127] Z. Ding, M. Peng, and H. V. Poor, "Cooperative non-orthogonal multiple access in 5G systems," *IEEE Communications Letters*, vol. 19, pp. 1462-1465, 2015.

[128] Z. Zhang, Z. Ma, Y. Xiao, M. Xiao, G. K. Karagiannidis, and P. Fan, "Non-orthogonal multiple access for cooperative multicast millimeter wave wireless networks," *IEEE Journal on Selected Areas in Communications*, vol. 35, pp. 1794-1808, 2017.

[129] S.-L. Shieh and Y.-C. Huang, "A simple scheme for realizing the promised gains of downlink nonorthogonal multiple access," *IEEE Transactions on Communications*, vol. 64, pp. 1624-1635, 2016.

[130] S.-L. Shieh, C.-H. Lin, Y.-C. Huang, and C.-L. Wang, "On gray labeling for downlink non-orthogonal multiple access without SIC," *IEEE Communications Letters*, vol. 20, pp. 1721-1724, 2016.

[131] Y. Tian, K.-L. Lee, C. Lim, and A. Nirmalathas, "Experimental comparison of DSB-SC & OSSB based 60 GHz radio-over-fiber fronthaul links," in *Microwave Photonics (MWP), 2016 IEEE International Topical Meeting on*, 2016, pp. 141-144.

[132] A. Ng'oma, "Radio-over-fiber techniques for millimeter wave wireless applications," in *Microwave Photonics (MWP), 2015 International Topical Meeting on*, 2015, pp. 1-4.

[133] C. Lim, C. Pulikkaseril, and K.-L. Lee, "A study on LCoS-based remote nodes for 60 GHz fiber-wireless links," *Lightwave Technology, Journal of*, vol. 30, pp. 3110-3117, 2012.

[134] Y. Yang, M. J. Crisp, R. V. Penty, and I. H. White, "Low-cost MIMO radio over fiber system for multiservice DAS using double sideband frequency translation," *Journal of Lightwave Technology*, vol. 34, pp. 3818-3824, 2016.

[135] P. K. Agyapong, M. Iwamura, D. Staehle, W. Kiess, and A. Benjebbour, "Design considerations for a 5G network architecture," *IEEE Communications Magazine*, vol. 52, pp. 65-75, 2014.

[136] J. Yu, G.-K. Chang, Z. Jia, A. Chowdhury, M.-F. Huang, H.-C. Chien, *et al.*, "Cost-effective optical millimeter technologies and field demonstrations for very high throughput wireless-over-fiber access systems," *Journal of Lightwave Technology*, vol. 28, pp. 2376-2397, 2010.

[137] S. X. Chew, X. Yi, S. Song, L. Li, P. Bian, L. Nguyen, *et al.*, "Silicon-on-insulator dual-ring notch filter for optical sideband suppression and spectral characterization," *Journal of Lightwave Technology*, vol. 34, pp. 4705-4714, 2016.

[138] H.-C. Liu and A. Yariv, "Synthesis of high-order bandpass filters based on coupled-resonator optical waveguides (CROWs)," *Optics express*, vol. 19, pp. 17653-17668, 2011.

[139] S. Song, X. Yi, S. X. Chew, L. Li, L. Nguyen, and R. Zheng, "Optical single-sideband modulation based on silicon-on-insulator coupled-resonator optical waveguides," *Optical Engineering*, vol. 55, pp. 031114-031114, 2016.

[140] J. Li, T. Ning, L. Pei, S. Gao, H. You, H. Chen, *et al.*, "Performance analysis of an optical single sideband modulation approach with tunable optical carrier-to-sideband ratio," *Optics & Laser Technology*, vol. 48, pp. 210-215, 2013.

[141] J. Zhang, H. Chen, M. Chen, T. Wang, and S. Xie, "A photonic microwave frequency quadrupler using two cascaded intensity modulators with repetitious optical carrier suppression," *IEEE Photonics Technology Letters*, vol. 19, pp. 1057-1059, 2007.

[142] A. A. F. Júnior, O. L. Coutinho, C. de Sousa Martins, J. A. J. Ribeiro, V. R. de Almeida, and J. E. B. Oliveira, "Analytical model of optical fiber chromatic dispersion effect in upconverted millimeter-wave long-haul fiber optic link," in *International Workshop on Telecommunications (IWT)*, 2013, pp. 1-8.

[143] C. Lim, K.-L. Lee, A. Nirmalathas, D. Novak, and R. Waterhouse, "Impact of chromatic dispersion on 60 GHz radio-over-fiber transmission," in *LEOS 2008-21st Annual Meeting of the IEEE Lasers and Electro-Optics Society*, 2008.

[144] G. Meslener, "Chromatic dispersion induced distortion of modulated monochromatic light employing direct detection," *IEEE Journal of Quantum Electronics,* vol. 20, pp. 1208-1216, 1984.

[145] K. Yonenaga and N. Takachio, "A fiber chromatic dispersion compensation technique with an optical SSB transmission in optical homodyne detection systems," *IEEE Photonics Technology Letters,* vol. 5, pp. 949-951, 1993.

[146] J. Ma, J. Yu, C. Yu, X. Xin, J. Zeng, and L. Chen, "Fiber dispersion influence on transmission of the optical millimeter-waves generated using LN-MZM intensity modulation," *Journal of Lightwave Technology,* vol. 25, pp. 3244-3256, 2007.

[147] W.-J. Jiang, C.-T. Lin, A. Ng'oma, P.-T. Shih, J. Chen, M. Sauer, *et al.*, "Simple 14-Gb/s short-range radio-over-fiber system employing a single-electrode MZM for 60-GHz wireless applications," *Journal of Lightwave Technology,* vol. 28, pp. 2238-2246, 2010.

[148] C.-T. Lin, J. J. Chen, S.-P. Dai, P.-C. Peng, and S. Chi, "Impact of nonlinear transfer function and imperfect splitting ratio of MZM on optical up-conversion employing double sideband with carrier suppression modulation," *Journal of Lightwave Technology,* vol. 26, pp. 2449-2459, 2008.

[149] B. Hraimel, X. Zhang, Y. Pei, K. Wu, T. Liu, T. Xu, *et al.*, "Optical single-sideband modulation with tunable optical carrier to sideband ratio in radio over fiber systems," *Journal of Lightwave Technology,* vol. 29, pp. 775-781, 2011.

[150] M. Cvijetic and I. Djordjevic, *Advanced optical communication systems and networks*: Artech House, 2013.

[151] R. Dahlgren, "Noise in fiber optic communication links," *signal,* vol. 2, p. 2, 2000.

[152] D. M. Baney, P. Gallion, and R. S. Tucker, "Theory and measurement techniques for the noise figure of optical amplifiers," *Optical fiber technology,* vol. 6, pp. 122-154, 2000.

[153] X. Shen, K. Xu, J. Wu, and J. Lin, "Power consumption modelling of radio-over-fiber distributed antenna system based wireless sensor network," 2011.

[154] A. S. Gowda, H. Yang, S. T. Abraha, A. Ng'oma, A. R. Dhaini, L. G. Kazovsky, *et al.*, "Energy consumption of indoor radio-over-fiber distribution links: Experimental findings," in *2014 IEEE Global Communications Conference*, 2014, pp. 2612-2617.

[155] R. S. Tucker, "Green optical communications—Part I: Energy limitations in transport," *IEEE Journal of selected topics in quantum electronics,* vol. 17, pp. 245-260, 2011.

[156] G. P. Fettweis, "A 5G wireless communications vision," *Microwave Journal,* vol. 55, pp. 24-36, 2012.

[157] L. Li, M. Bi, W. Jia, and W. Hu, "Experiment demonstration of optical fronthaul transmission system based on power division multiplexing for future 5G scenarios," in *Asia Communications and Photonics Conference*, 2016, p. AF1C. 4.

[158] S. M. Alamouti, "A simple transmit diversity technique for wireless communications," *IEEE Journal on selected areas in communications,* vol. 16, pp. 1451-1458, 1998.

[159] J. R. Hampton, *Introduction to MIMO communications*: Cambridge university press, 2013.

[160] F.-C. Zheng, A. G. Burr, and S. Olafsson, "Near-optimum detection for distributed space-time block coding under imperfect synchronization," *IEEE transactions on communications,* vol. 56, 2008.

[161] Y. Zhu, Z. Zhang, Z. Marzi, C. Nelson, U. Madhow, B. Y. Zhao, *et al.*, "Demystifying 60GHz outdoor picocells," in *Proceedings of the 20th annual international conference on Mobile computing and networking*, 2014, pp. 5-16.

[162] L. Hanzo, T. Liew, B. Yeap, R. Tee, and S. X. Ng, *Turbo coding, turbo equalisation and space-time coding: EXIT-chart-aided near-capacity designs for wireless channels* vol. 22: John Wiley & Sons, 2011.

[163] H. Zhang and H. Dai, "Cochannel interference mitigation and cooperative processing in downlink multicell multiuser MIMO networks," *EURASIP Journal on Wireless Communications and Networking*, vol. 2004, pp. 222-235, 2004.

[164] M. S. Ali, E. Hossain, and D. I. Kim, "Coordinated multi-point (CoMP) transmission in downlink multi-cell NOMA systems: models and spectral efficiency performance," *arXiv preprint arXiv:1703.09255*, 2017.

[165] A. Beylerian and T. Ohtsuki, "Coordinated non-orthogonal multiple access (CO-NOMA)," in *Global Communications Conference (GLOBECOM), 2016 IEEE*, 2016, pp. 1-5.

[166] W. Shin, M. Vaezi, B. Lee, D. J. Love, J. Lee, and H. V. Poor, "Non-orthogonal multiple access in multi-cell networks: Theory, performance, and practical challenges," *IEEE Communications Magazine*, vol. 55, pp. 176-183, 2017.

[167] Y. Tian, A. R. Nix, and M. Beach, "On the performance of opportunistic NOMA in downlink CoMP networks," *IEEE Communications Letters*, vol. 20, pp. 998-1001, 2016.

[168] D. Boviz, C. S. Chen, and S. Yang, "Effective design of multi-user reception and fronthaul rate allocation in 5G cloud RAN," *IEEE Journal on Selected Areas in Communications*, 2017.

[169] D. Boviz, C. S. Chen, and S. Yang, "Cost-aware fronthaul rate allocation to maximize benefit of multi-user reception in C-RAN," in *IEEE Wireless Communications and Networking Conference (WCNC)*, 2017.

[170] P. T. Dat, A. Kanno, N. Yamamoto, and T. Kawanishi, "Simultaneous transmission of multi-RATs and mobile fronthaul in the MMW bands over an IFoF system," in *Optical Fiber Communication Conference*, 2017, p. W1C. 4.

[171] M. S. Ali, H. Tabassum, and E. Hossain, "Dynamic user clustering and power allocation for uplink and downlink non-orthogonal multiple access (NOMA) systems," *IEEE Access*, vol. 4, pp. 6325-6343, 2016.

[172] M. Newton and J. Thompson, "Classification and generation of non-uniform user distributions for cellular multi-hop networks," in *Communications, 2006. ICC'06. IEEE International Conference on*, 2006, pp. 4549-4553.

[173] E. Kassem, R. Marsalek, and J. Blumenstein, "On the capacity of fractional frequency reuse with three power levels for non-uniform user distribution," in *Systems, Signals and Image Processing (IWSSIP), 2016 International Conference on*, 2016, pp. 1-5.

[174] S. Ali, E. Hossain, and D. I. Kim, "Non-orthogonal multiple access (NOMA) for downlink multiuser MIMO systems: User clustering, beamforming, and power allocation," *IEEE Access*, vol. 5, pp. 565-577, 2017.

[175] T. S. Rappaport, *Wireless communications: principles and practice* vol. 2: prentice hall PTR New Jersey, 1996.

[176] F. C. Commission, "Revision of part 15 of the commission's rules regarding operation in the 57-64 GHz band," *Federal Communications Commission, Tech. Rep*, 2013.

[177] W. Keusgen, R. J. Weiler, M. Peter, M. Wisotzki, and B. Göktepe, "Propagation measurements and simulations for millimeter-wave mobile access in a busy urban environment," in *Infrared, Millimeter, and Terahertz waves (IRMMW-THz), 2014 39th International Conference on*, 2014, pp. 1-3.

[178] T. S. Rappaport, G. R. MacCartney, M. K. Samimi, and S. Sun, "Wideband millimeter-wave propagation measurements and channel models for future wireless communication system design," *IEEE Transactions on Communications*, vol. 63, pp. 3029-3056, 2015.

[179] J. Fan, Q. Yin, G. Y. Li, B. Peng, and X. Zhu, "MCS selection for throughput improvement in downlink LTE systems," in *Computer Communications and Networks (ICCCN), 2011 Proceedings of 20th International Conference on*, 2011, pp. 1-5.

Appendix A: Acronyms

ADC	Analogue-to-Digital Converter
AOA	Angle of Arrival
APD	Avalanche Photodiodes
ASE	Amplified Spontaneous Emission
AWG	Arbitrary Waveform Generator
BBU	Baseband Unit
BDMA	Bit Division Multiple Access
BER	Bit Error Ratio
BLER	System Block Error Rate
BPF	Bandpass Filter
BS	Beam Station
BW	Bandwidth
CD	Chromatic Dispersion
CDF	Cumulative Density Function
CDMA	Code Division Multiple Access
CFO	Carrier Frequency Offset
CO	Central Office
CoMP	Coordinated Multipoint
CPRI	common public radio interface
C-RAN	Cloud Radio Access Network
CSI	Channel State Information
CW	Continuous Wave

CWDM	Coarse Wavelength-Division Multiplexing
DAC	Digital to Analogue Converter
DC	Direct Current
DE-MZM	Dual-electrode MZM
DFB LD	Distributed-Feedback Laser Diode
DFE	Decision Feedback Equalizer
DSO	Digital Storage Oscilloscope
DSB	Double Sideband
DSB-SC	Double Sideband Suppress Carrier
DSP	Digital Signal Processing
EAM	Electro-Absorption Modulator
EDFA	Erbium-Doped Fibre Amplifier
EIM	Electromagnetic Interference
EVM	Error Vector Magnitude
FEC	Forward Error Correction
FDM	Frequency-Division Multiplexing
FSO	Free-Space Optics
FSPL	Free Space Path Loss
FU	Far User
GPP	General Purpose Processor
HetNet	Heterogeneous Network
ICI	Inter-Carrier Interference
ICIC	Intercell Interference Coordination
IF	Intermediate Frequency
IoT	Internet of Things
ISI	Inter-symbol Interference
JT	Joint Transmission
LCoS	Liquid Crystal on Silicon
LO	Local Oscillator

LOS	Line-of-Sight
LTE	Long-term Evolution
LTE-A	Long Term Evolution Advanced
MIMO	Multiple Input Multiple Output
MLC	Multi-level Code
mm-wave	Millimeter Wave
MZM	Mach-Zehnder Modulator
NOMA	Non-orthogonal Multiple Access
NU	Near User
OBSAI	Open Base Station Architecture Initiative
OCS	Optical Carrier Suppression
OCSR	Optical Carrier-to-sideband Ratio
OFDM	Orthogonal Frequency Division Multiplexing
OMA	Orthogonal Multiple Access
ORI	Open Radio equipment Interface
OSSB	Optical Single Sideband
PC	Polarization Controller
PD	Photodetector
PDF	Probability Density Function
PDMA	Pattern Division Multiple Access
PON	Passive Optical Network
QAM	Quadrature Amplitude Modulation
QoS	Quality of Service
RAN	Radio Access Network
RF	Radio Frequency
RIN	Relative Intensity Noise
RoF	Radio-over-Fiber
RRH	Remote Radio Head
SE	Spectral Efficiency

SEFDM	Spectrally Efficient Frequency Division Multiplexing
SEM	Scanning Electron Microscope
SFBC	Space-Frequency Block Coding
SFDR	Spurious-Free Dynamic Range
SIC	Successive Interference Cancellation
SINR	Single-to-Interference plus Noise Ratio
SMF	Single-Mode Fibre
SNR	Signal to Noise Ratio
SOI	Silicon-on-Insulator
SPC	Superposition code
STBC	Space Time Block Coding
STO	Signal Timing Offset
TDM	Time-Division Multiplexing
TE	Transverse Electric mode
TM	Transverse Magnetic mode
UE	User Equipment
VLC	Visible Light Communication
WDM	Wavelength-Division Multiplexing
WS	Waveshaper